The Observation and Interpretation of some Properties of $SmCo_5$ Permanent Magnet Alloys

by

C.K.Mylvaganam

A thesis submitted to the Faculty of Graduate Studies of the University of Manitoba in partial fulfilment of the requirements for the degree of Doctor of Philosophy.

Department of Physics
University of Manitoba
June, 1980

THE OBSERVATION AND INTERPRETATION OF SOME PROPERTIES OF $SmCo_5$ PERMANENT MAGNET ALLOYS

BY

CHANDRARAJ KANTHA MYLVAGANAM

A thesis submitted to the Faculty of Graduate Studies of the University of Manitoba in partial fulfillment of the requirements of the degree of

DOCTOR OF PHILOSOPHY

Acknowledgements

I am indebted to my supervisor, Professor Paul Gaunt, who actively participated in this research project, making a substantial contribution to its successful completion.

I am grateful to Mr. Gilles Roy, who willingly made available his vast store of expertise on experimental matters whenever it was requested.

Thanks are also due to Ms. Yuen Cheng, who assisted me with some aspects of the computer programming and to Mr. Greg Kenning, who analysed some of the X-ray data.

Finally, I would like to express my deep appreciation of the understanding and encouragement afforded me throughout the duration of this project by my wife, Ruvani, who also did such an excellent job of typing this thesis.

Abstract

The high coercive force of liquid-phase sintered $SmCo_5$ alloys is associated with grain boundary inhomogeneities. In the demagnetized initial state, on cooling from the Curie temperature, a uniaxial material such as $SmCo_5$ will contain several 180^o domain walls. Upon application of a forward field, neighbouring 180^o walls will approach each other and, depending on their relative sense of spin rotation, will either be annihilated or form a tightly wound 360^o wall. In the presence of an inhomogeneous region with a lower wall energy than the matrix, the 360^o wall may be pinned, forming a nucleation centre which requires a large reverse field to unpin it and regenerate the two original 180^o walls.

The interaction between a 360^o wall and a localized planar inhomogeneity is treated micromagnetically to develop a model which minimizes the activation energy.

Measurements of magnetization and Barkhausen effect confirm that in sintered $SmCo_5$, domain walls are pinned at highly localized sites which coincide with grain boundaries. The model is therefore applied to this material, assuming a planar Sm_2Co_{17} inhomogeneity. Calculations are performed for inhomogeneity thicknesses up to 125Å at temperatures varying from 4.2K to 500K. Coercive fields that agree closely with experimental determinations are obtained. A critical inhomogeneity thickness (17Å at 77K) below which the coercivity disappears is determined at each temperature. Above this thickness, coercivity rises

steeply until it reaches a plateau. It is observed that more than one pair of walls can exist within the grain.

The interaction between an inhomogeneity and a domain wall may be described by a parabolic force, which gives a two-thirds power relationship between activation energy and field. A similar power relationship is exhibited by the activation energy calculated from the micromagnetic model.

The possibility that the continuously pinned wall's escape may be facilitated by thermal activation is considered. It is suggested that the wall bows out, forming a thermally activated 'blister', before breaking away at a smaller field than might otherwise be expected. The activation energy/field parameter, $(\frac{\partial E}{\partial H})_T$, is determined by combining the micromagnetic and parabolic force theories.

Measurements of magnetic after-effect made at temperatures from 4.2K to room temperature, over a range of effective fields to 20kOe, reveal the presence of a range of activation energies within the material. $(\frac{\partial E}{\partial H})_T$ is obtained at each field and is seen to extrapolate towards the theoretical value at the predicted coercive field. It is further observed that even though the viscosity coefficient is dependent on specimen history, $(\frac{\partial E}{\partial H})_T$ depends only on the effective field present.

The presence of non-stoichiometric phases which have different crystalline anisotropies is consistent with the observed relationship between H_{eff} and $(\frac{\partial E}{\partial H})_T$.

TABLE OF CONTENTS

CHAPTER 1

INTRODUCTION

1.1 Domains and Domain Walls

Ferromagnets are defined as those materials in which atomic dipole moments are aligned parallel to one another. Such materials can therefore exhibit a magnetic moment even in the absence of a field. Despite this property of spontaneous magnetization, a ferromagnet which has not been exposed to a magnetic field will not exhibit a magnetic moment. Upon the application of even a small field however, a large moment may be seen.

To explain these phenomena, Weiss (1907) postulated the existence of small spontaneously magnetized regions, which he called 'domains', within the material. These domains would have individual magnetic moments, but could be aligned in such a manner as to give a null resultant moment over the whole material. When a field was applied, they would realign themselves, giving a new resultant moment. Such a multi-domain configuration has, in general, a lower magnetostatic energy than a single region of uniform magnetization over the entire material. (When the material is sufficiently small however, the single domain configuration is the preferred one.)

The region between adjacent domains is one in which atomic moments are in the process of changing direction, as shown in figure 1.1-1. This boundary layer is known as a 'domain wall'. Realignment of domains is therefore characterized by movement of domain walls.

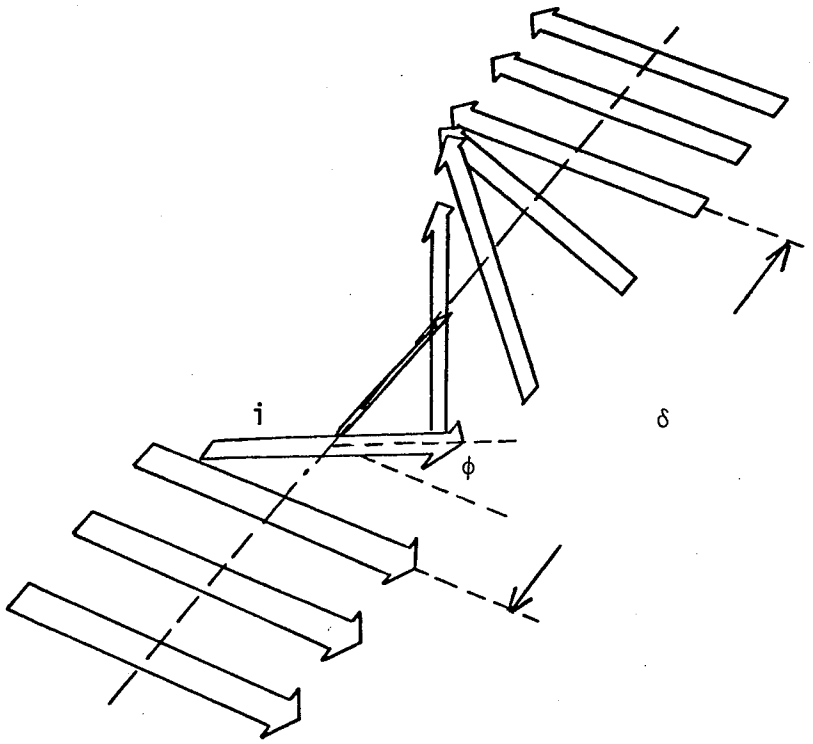

Figure 1.1-1 - A 180° domain wall of width δ. The spins are rotating out of the plane of magnetization. The i^{th} spin has rotated by an angle ϕ.

1.2 Magnetic Hardening

1.2.1 Introduction

When a material has been magnetized to saturation, it can be demagnetized by applying a field in the direction opposite to that of the moment. The required field is known as the 'coercive field'. A large coercive field is a characteristic of 'hard' magnetic materials. While the boundary between hard and soft materials is not precisely defined, a coercive field of 50 Oe is generally regarded as being indicative of magnetic hardness. Plainly, the harder the material, the more desirable it is as a permanent magnet.

If a material is magnetically hard, it is difficult to change its domain configuration or to move its domain walls from their static positions. Magnetic hardening must therefore be characterized by a mechanism which keeps the wall 'pinned' or 'trapped' until the coercive field is applied. Many theories of magnetic hardening have been suggested and the following is a brief description of some of them.

1.2.2 Reversal of Single Domain Particles

Stoner and Wohlfarth (1948) have studied the difficulty of reversing single domain particles if they have initially been magnetized in the easy direction of the material. Here the change in anisotropy energy has to be overcome by the energy contributed by the magnetic field and when this energy is attained at the coercive field the magnetization will flip around.

1.2.3 Non-Ferromagnetic Inclusions

The effect on coercivity of non-ferromagnetic inclusions within a ferromagnetic matrix was examined by Kersten (1943) in his study of copper and carbon inhomogeneities in iron. He looked at the effect on the energy of the domain wall when it intersected an inclusion. Since the inclusion was non-magnetic, this in effect shortened the wall, decreasing its energy and therefore placed it in an energy state which was preferable to the one where it did not intersect an inclusion. The wall would thus remain pinned by the inclusion until a sufficiently large field was applied.

Consider a matrix of saturation magnetization I per unit volume and containing n inclusions per unit volume which are spherical, with radius r, occupying the corners of a cubic lattice. A wall of unit area will therefore intersect $n^{2/3}$ inclusions.

Initially the wall is in a pinned state, lying across the middle of the plane of inclusions as shown in figure 1.2.3-1a. When a field H is applied, the wall is displaced a distance x as in figure 1.2.3-1b.

The change in wall area per inclusion is

$$\pi r^2 - \pi(r^2 - x^2).$$

If γ is the wall energy per unit area, the change in wall energy per unit area is $n^{2/3}\gamma\pi x^2$.

When the wall is displaced by x, this means that a volume of x per unit area has reversed magnetization. The corresponding change in

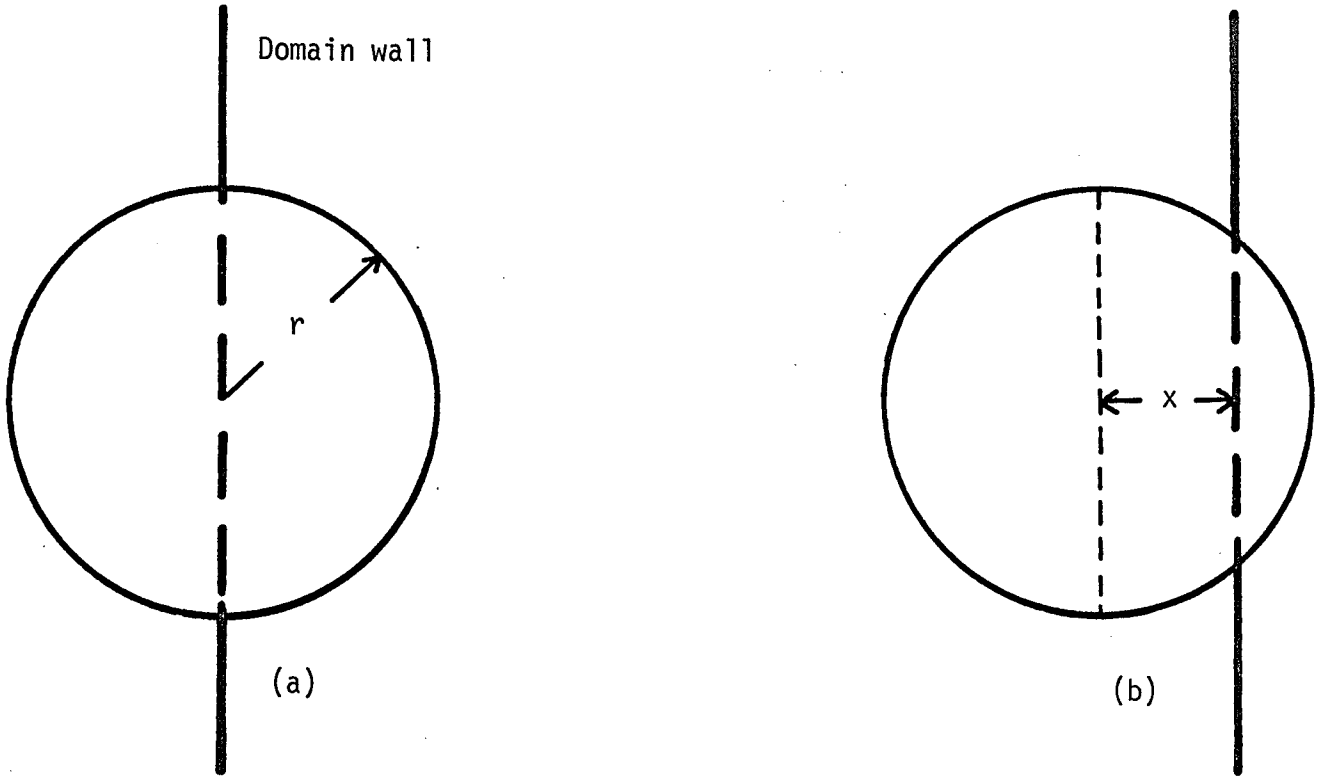

Figure 1.2.3-1 - (a) Domain wall pinned by an inclusion in the absence of a field.
(b) Wall has been displaced by the application of a field.

energy per unit area is $2HIx$.

The total energy per unit area,

$$\Delta E = n^{2/3}\pi\gamma x^2 - 2HIx \ .$$

Since this must be minimized,

$$\frac{\partial(\Delta E)}{\partial x} = 0$$

and this gives,

$$H = \frac{\pi n^{2/3} \gamma}{I} x \ .$$

Displacement is therefore proportional to the field as long as the wall is being intersected. The field required so that wall may reach the edge of the inclusions is

$$H_c = \frac{\pi n^{2/3} \gamma}{I} x \ ,$$

and this must be the coercive field because once the wall has passed through the inclusions, it is free to continue moving through the material until it reaches the next plane of obstacles. Since all inclusions are the same size, this field should be sufficient to enable the wall to move freely through the entire material.

This theory yielded satisfactory correlation with experimental observations in cases where the dimensions of the obstacle were much greater than the width of the domain wall.

1.2.4 Ferromagnetic Inclusions

Kersten's theory can, with the appropriate modifications, be extended to the case of ferromagnetic inclusions within a ferromagnetic

matrix. Pinning can take place in such a situation if the domain wall energy within the inclusion is lower than that within the matrix. The wall will then have a lower energy if it intersects inclusions and will prefer to remain in this state.

Conversely, an inclusion with a higher energy will act as an obstacle, blocking the path of the wall.

1.2.5 Free Poles

Néel (1946) criticized Kersten's theory on the grounds that even though inclusions would be expected to have free poles on their surfaces, producing disperse fields with large magnetostatic energies, their presence had been ignored. The presence of random strains in the material could cause changes in the easy direction of magnetization, producing further free poles and these should have been considered as well.

Neel showed that the logarithm of the coercive field varied linearly with the logarithm of the volume fraction of inclusions and compared his theoretical values with experimental results for many systems.

1.3 The Present Study

In the present study, the processes governing magnetic hardening in sintered $SmCo_5$ permanent magnet alloys were examined. Craik and Hill (1974) have suggested that magnetic hardening in rare earth-cobalt materials may be caused by the insertion within the material of planes

having different exchange and anisotropy energies. As detailed more fully by other authors (chapter 2), $SmCo_5$ alloys may be expected to contain other phases of Sm-Co compounds, such as Sm_2Co_{17} and Sm_2Co_7, which are also ferromagnetic. An order of magnitude calculation indicated negligible demagnetizing effects due to inhomogeneities within the matrix. A theory of coercivity in which domain walls were pinned by planar inclusions of a secondary phase was therefore developed. The remainder of this section seeks to outline the path taken to develop and to substantiate this model.

A model describing the interaction between a 180° domain wall and a planar inhomogeneity was synthesized (chapter 3). This gave expressions for the distribution of energy barriers and the effect of thermal activation.

In chapter 4 expressions for the energy of a domain wall in an $SmCo_5$ matrix as it interacted with planar Sm_2Co_{17} inhomogeneities were derived using a micromagnetic approach and values for the coercive field were obtained. These were compared with the experimental determinations of coercivity in chapter 6 as well as those contained in other studies.

The validity of the interaction model was tested by comparing the energy barrier distribution obtained from the purely theoretical calculation of chapter 3 with the values from the magnetic after-effect experiments of chapter 7. This, being a direct evaluation, gives a much better indication of barrier distribution than the measurements of coercive field, because the effect of thermal activation on coercivity itself is relatively small.

The model was based on the premise that pinning took place only at inhomogeneities and that there was free movement of domain walls within the grain. This was verified with further magnetization measurements to study the reversibility of domains (chapter 6), as well as by measurements of Barkhausen jumps (chapter 8) which were correlated with the grain size measurements of chapter 5.

X-ray diffraction and electron microscopy were used to positively identify the material used, as well as to yield information on the nature and distribution of any inhomogeneities that may have been present (chapter 5).

The above is a brief outline of the procedure that was followed in this investigation. It is, along with the findings, detailed fully in the following chapters. The results are discussed in chapter 9.

CHAPTER 2

SAMARIUM-COBALT MAGNET MATERIAL

2.1 Introduction

$SmCo_5$ has found widespread use as a commercial magnet because of its desirable permanent magnet characteristics which include large coercivities and $(BH)_{max}$ energy products. Interestingly, these properties are not exhibited by the bulk alloy, but by small particles of the material. They are further enhanced when the particles are aligned and compacted to a high density.

The $SmCo_5$ magnets used in this study were manufactured in this manner. This chapter therefore examines the structure of the material, the process of manufacture, the likelihood of the presence of secondary phases and the structure of such phases.

2.2 Structure of $SmCo_5$

Crystals of $SmCo_5$ have alternate layers as shown in figure 2.2-1. One type of layer has a hexagonal arrangement of Co atoms. The other has Sm and Co atoms in a 1:2 ratio. The structure, which is hexagonal, belongs to the P6/mmm space group with the following atomic co-ordinates for the unit cell:

$$\text{Sm} - (0\ 0\ 0)$$

$$\text{Co} - (\tfrac{1}{3}\ \tfrac{2}{3}\ 0), (\tfrac{2}{3}\ \tfrac{1}{3}\ 0)$$

$$(\tfrac{1}{2}\ 0\ \tfrac{1}{2}), (0\ \tfrac{1}{2}\ \tfrac{1}{2}), (\tfrac{1}{2}\ \tfrac{1}{2}\ \tfrac{1}{2})$$

as given by the International tables for X-ray crystallography, Volume I (1969).

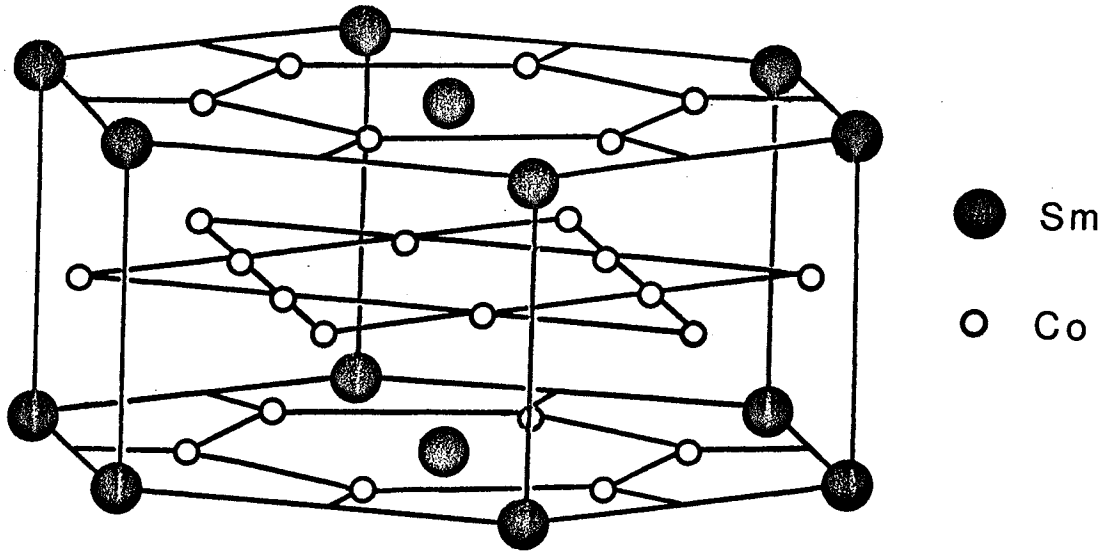

Figure 2.2-1 - Structure of $SmCo_5$.

Typical lattice parameters, according to Taylor (1971), are $a = 4.989\text{Å}$, $c = 3.981\text{Å}$.

2.3 Manufacture of the Magnets

Two techniques have been used for the densification of $SmCo_5$ powders. The first is the process of mechanical compaction, which was successfully carried out by Buschow, Luiten and Westendorp (1969). They aligned loosely packed $SmCo_5$ powder in a magnetic field and pressed it to a relative density of 70%. It must be noted that it is essential to have initial loose packing so that the particles may rotate easily. Further compression under a hydrostatic pressure of 20 kbars, combined with uniaxial deformation, increased relative density to over 95%. This process gives the desired permanent magnet properties, but because of the high pressures that are required, the size of the magnet is restricted.

The other is the technique of bonding the aligned particles by heating them, known as sintering. A problem here was that stoichiometric $SmCo_5$ underwent a loss of coercivity during the sintering process, as reported by Cech (1970). Benz and Martin (1970) overcame this by combining two melts at 1100°C. The first was stoichiometric with 66.7 wt.% Co, while the second, which was in its liquid phase at this temperature, has 40 wt.% Co. They were mixed to an average composition of 62.6 wt.% Co, which corresponds to 81 at.% Co. After aligning and pressing to 13 kbars, the powder was sintered at 1100°C for 30 minutes. Relative densities of 90 to 95% were obtained in this manner. Such a process is known as liquid phase sintering.

Das (1969) used a single melt with 63 wt.% Co instead of a combination of melts as described above.

The sintering temperature and time are critical in determining the permanent magnet properties of the alloy. Further heat treatment of the sintered magnet is carried out to enhance them.

2.4 Secondary Phases

2.4.1 Formation

The cobalt-rich portion of the Sm-Co phase diagram (Buschow and den Broeder 1973) is reproduced in figure 2.4.1-1. It is evident that small variations in the stoichiometry of the alloy will give rise to secondary cobalt-rich Sm_2Co_{17} or samarium-rich Sm_2Co_7 phases. Indeed, the presence of secondary phases is almost unavoidable, because if a single stoichiometric powder is used, heavy oxidation of the samarium will lead to the formation of a cobalt-rich phase (Jorgensen and Bartlett 1973), whereas the mixing of hypostoichiometric and stoichiometric powders in the liquid phase sintering process will give an initially samarium-rich phase which, depending on the degree of oxidation of samarium can even become cobalt-rich. The post-sintering annealing to which the material is subjected can cause some further decomposition of the primary $SmCo_5$ phase. This eutectoid decomposition has been studied by den Broeder and Buschow (1972) and Martin and Smeggil (1973). The effect of these secondary phases on magnetic properties has been examined by den Broeder and Zijlstra (1976) and will be discussed in the final chapter.

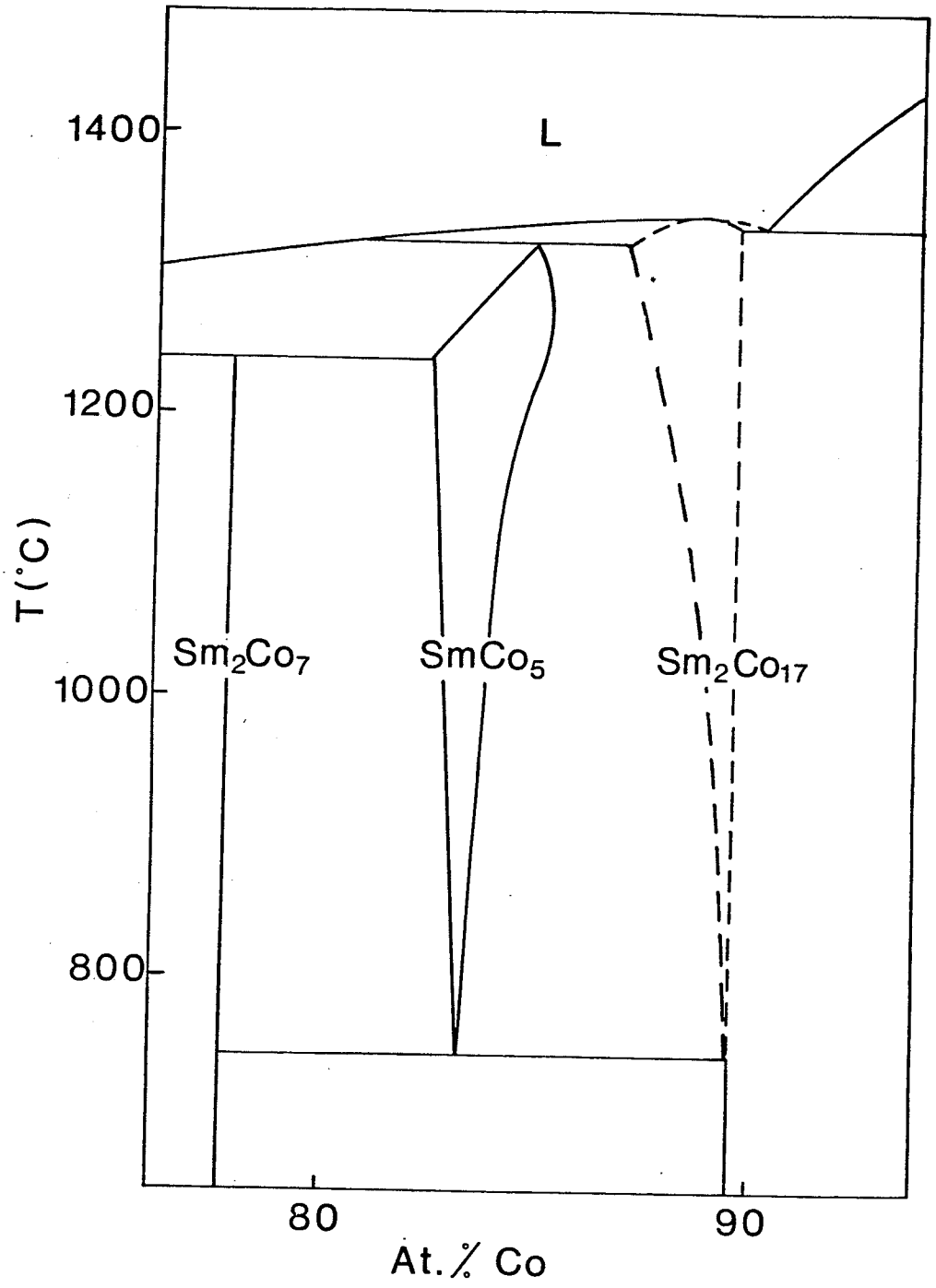

Figure 2.4.1-1 - Co-rich portion of the Sm-Co phase diagram (Buschow and den Broeder 1973).

2.4.2 Structure of Sm_2Co_{17}

Sm_2Co_{17} can have either a hexagonal or a rhombohedral structure. The hexagonal lattice is formed from the $SmCo_5$ lattice by having an ordered sublattice of a pair of Co atoms for every third Sm atom, followed by a [0 1 0] alternate sense stacking shift on every second (0 0 1) layer. This is illustrated in figure 2.4.2-1 (Ostertag, Strnat and Hoffer 1967). The rhombohedral structure, which is formed if the stacking displacement is not reversed, is illustrated in figure 2.4.2-2 (Ostertag et al 1967). The basal 'a' axes of the Sm_2Co_{17} unit cell are rotated by 30° with respect to those of the original $SmCo_5$ cell. 'a' is increased by a factor of $\sqrt{3}$. 'c' is doubled. Taylor (1971) gives lattice parameters for Sm_2Co_{17} as a = 8.402Å and c = 8.114Å (hexagonal) or 12.172Å (rhombohedral).

In the ITXC (v.I) notation, Ostertag et al (1967) have shown that the hexagonal Sm_2Co_{17} unit cell belongs to the $P6_3/mmc$ space group and has the following positions occupied:

Sm(1) - $\pm(0\ 0\ \frac{1}{4})$

Sm(2) - $\pm(\frac{1}{3}\ \frac{2}{3}\ \frac{3}{4})$

Co(1) - $\pm(\frac{1}{3}\ \frac{2}{3}\ z)$, $\pm(\frac{2}{3}\ \frac{1}{3}\ \frac{1}{2}+z)$

Co(2) - $(\frac{1}{2}\ 0\ 0)$, $(0\ \frac{1}{2}\ 0)$, $(\frac{1}{2}\ \frac{1}{2}\ \frac{1}{2})$,$(\frac{1}{2}\ \frac{1}{2}\ 0)$,$(\frac{1}{2}\ 0\ \frac{1}{2})$,$(0\ \frac{1}{2}\ \frac{1}{2})$

Co(3) - $\pm(x\ y\ \frac{1}{4})$, $\pm(\bar{y}\ x-y\ \frac{1}{4})$, $\pm(y-x\ \bar{x}\ \frac{1}{4})$, $\pm(\bar{y}\ \bar{x}\ \frac{1}{4})$, $\pm(x\ x-y\ \frac{1}{4})$, $\pm(y-x\ y\ \frac{1}{4})$

Co(4) - $\pm(x\ 2x\ z)$, $\pm(2\bar{x}\ \bar{x}\ z)$, $\pm(x\ \bar{x}\ z)$, $\pm(\bar{x}\ 2\bar{x}\ \frac{1}{2}+z)$, $\pm(2x\ x\ \frac{1}{2}+z)$, $\pm(\bar{x}\ x\ \frac{1}{2}+z)$

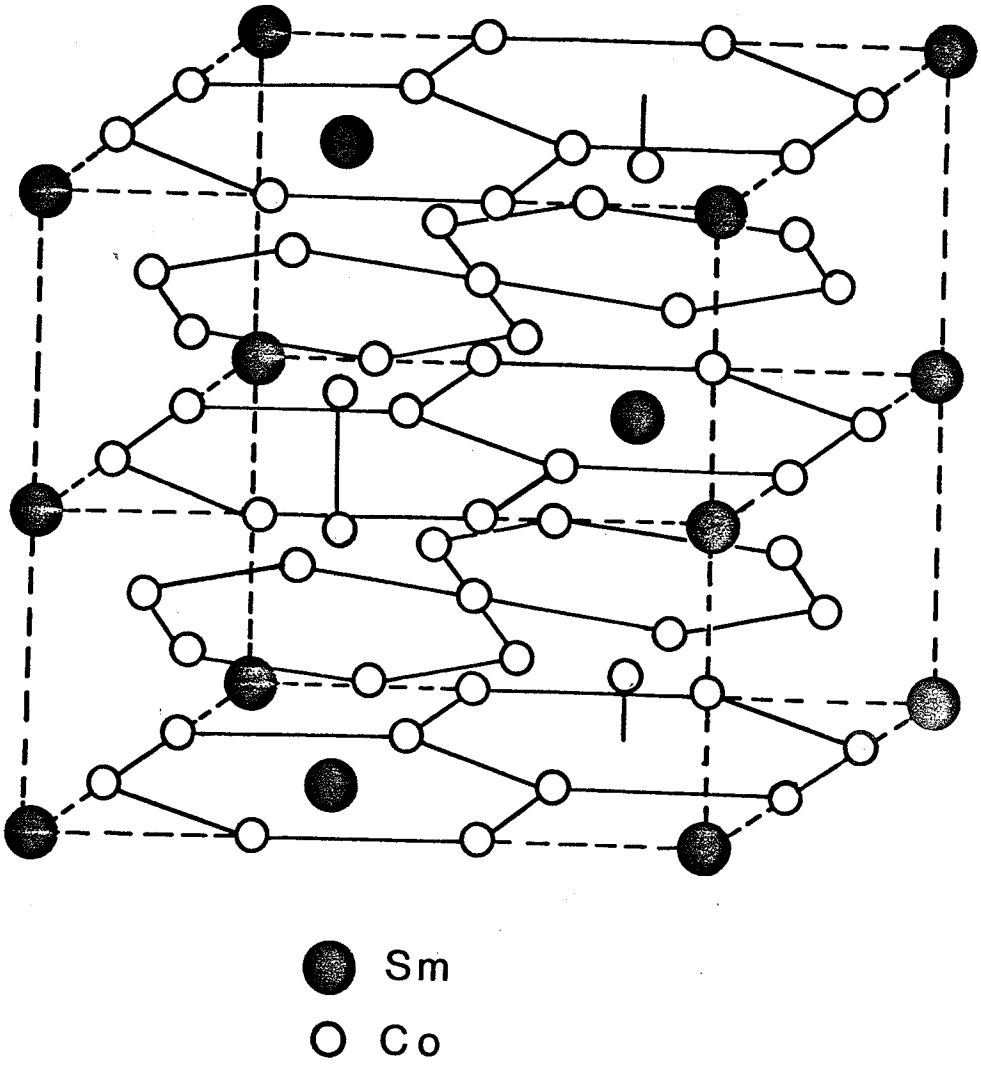

Figure 2.4.2-1 - Hexagonal Sm_2Co_{17}.

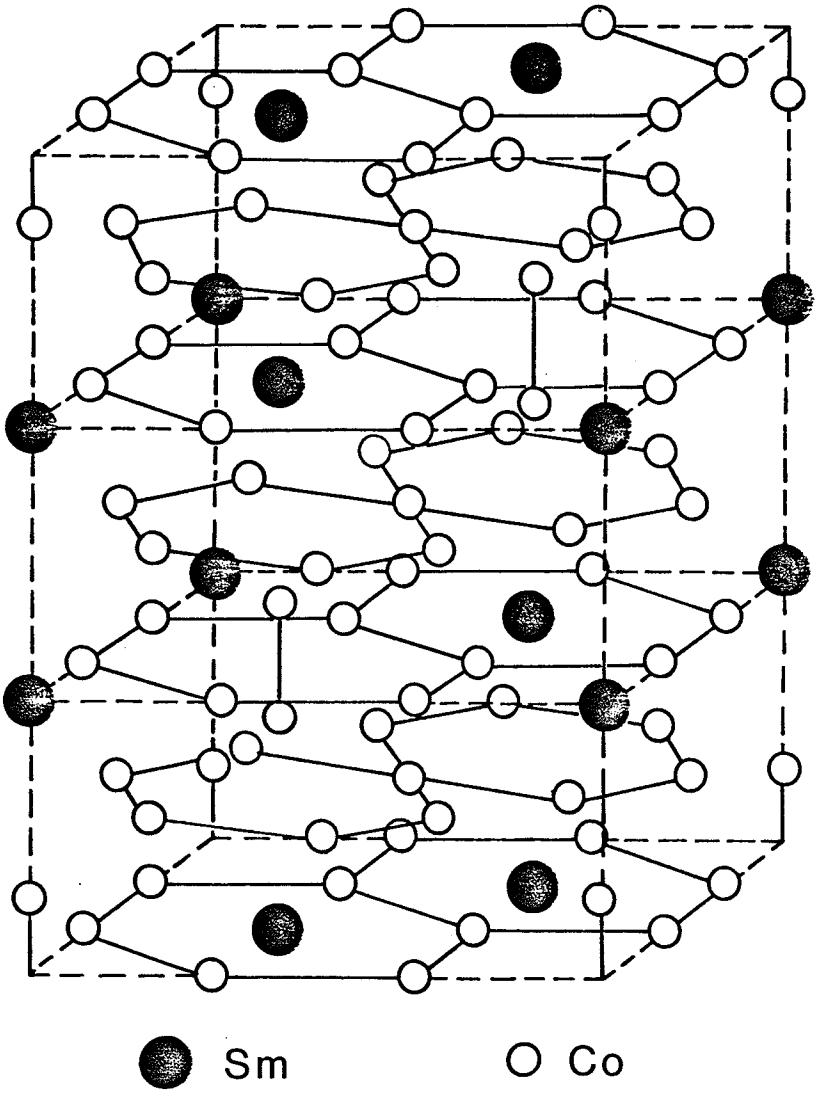

Figure 2.4.2-2 - Rhombohedral Sm_2Co_{17}.

The Co(1) atoms replace Sm atoms in the 1-5 configuration and have z = 0.89. For Co(3), x = $\frac{1}{3}$ and y = 0, while for Co(4), x = $\frac{1}{6}$ and z = 0.

These positions are somewhat idealized, representing a direct transformation from the $SmCo_5$ to the Sm_2Co_{17} lattice. The small displacements for stacking purposes, for example, which are caused by the size difference between the Sm and Co atoms have not been taken into account. However, Ostertag et al (1967), using the atomic co-ordinates given above, have obtained satisfactory agreement between predicted and observed intensities of X-ray diffraction, suggesting that deviations from these positions are of little consequence for the present purpose.

Rhombohedral Sm_2Co_{17} belongs to the $R\bar{3}m$ space group.

2.4.3 Structure of Sm_2Co_7

Sm_2Co_7 is formed from $SmCo_5$ by substitution of Sm for Co at the $\left[\frac{2}{3}\ \frac{1}{3}\ 0\right]$ position of every third (0 0 1) layer, followed by a $\left[\frac{1}{3}\ -\frac{1}{3}\ 0\right]$ stacking shift on the same layer. Once again, the structure can be either hexagonal or rhombohedral, depending on the sense of the stacking shift. Here 'c' is 6 times as great as for $SmCo_5$. Typically, a = 5.041Å and c = 24.33Å (hexagonal) and 36.31Å (rhombohedral) (Taylor 1971).

The unit cell of the hexagonal structure, which belongs to the $P6_3/mmc$ space group has the following atomic co-ordinates:

Sm - $\pm(0\ 0\ \frac{1}{12})$

$\pm(0\ 0\ \frac{1}{4})$, $\pm(\frac{1}{3}\ -\frac{1}{3}\ \frac{1}{4})$

$\pm(\frac{1}{3}\ -\frac{1}{3}\ \frac{5}{12})$

Co - $(\frac{1}{2}\ 0\ 0)$, $(0\ \frac{1}{2}\ 0)$, $(\frac{1}{2}\ \frac{1}{2}\ 0)$

$\pm(\frac{1}{3}\ -\frac{1}{3}\ \frac{1}{12})$, $\pm(-\frac{1}{3}\ \frac{1}{3}\ \frac{1}{12})$

$\pm(\frac{1}{2}\ 0\ \frac{1}{6})$, $\pm(0\ \frac{1}{2}\ \frac{1}{6})$, $\pm(\frac{1}{2}\ \frac{1}{2}\ \frac{1}{6})$

$\pm(-\frac{1}{3}\ \frac{1}{3}\ \frac{1}{4})$

$(-\frac{1}{6}\ \frac{1}{6}\ \pm\frac{1}{3})$, $(\frac{1}{3}\ \frac{1}{6}\ \pm\frac{1}{3})$, $(-\frac{1}{6}\ -\frac{1}{3}\ \pm\frac{1}{3})$

$\pm(\frac{1}{3}\ -\frac{1}{3}\ \frac{5}{12})$, $\pm(0\ 0\ \frac{5}{12})$

$(\frac{5}{6}\ \frac{1}{6}\ \frac{1}{2})$, $(\frac{5}{6}\ -\frac{1}{3}\ \frac{1}{2})$, $(\frac{1}{3}\ \frac{1}{6}\ \frac{1}{2})$

Once again, there will be small displacements within the space group, caused by the relative size difference of the substituted atoms.

CHAPTER 3

INTERACTION MODEL

3.1 Interaction Potentials

Any interaction may be expressed as a potential written in terms of a variable. The nature of the potential is dependent on the type of interaction under consideration. For example, the interaction between a dislocation and a lattice defect, or a domain wall and an inhomogeneity are pinning or repulsive interactions. The corresponding potentials must therefore be constructed in such a manner as to make the pinned state the more desirable one. A suitably designed potential well with a displacement variable satisfies this criterion.

The problem, therefore, is one of choosing an appropriate form for the interaction potential. Potentials have been designed to fit various situations, but they all have a common characteristic in that they are combinations of barriers and wells which either impede progress or cause trapping. The differences arise in choice of origin for the variable and the shape of the potential. Cottrell and Bilby (1949), for example, found that an inverse quadratic function suitably described the potential when a dislocation was pinned by a lattice defect. Granato, Lücke, Schlipf and Teutonico (1964) linearized this potential to obtain a form that they found more tractable. The interaction potential, it can therefore be seen, need not be rigid but can, in fact, be rather malleable within the framework of the criteria governing the interaction.

What follows in this chapter is the synthesis of a potential that suitably describes the interaction between a magnetic domain wall and an inhomogeneity.

3.2 Interaction between Domain Wall and Pin

When a domain wall is pinned at the origin, in the absence of a field, the restoring forces should be the same in both directions. It is therefore reasonable to look upon the wall as sitting in a symmetrical potential well and this potential must be described as an even function which increases for a short distance away from the pin and then tails off, such as

$$W(z) = \alpha z^2 - \beta z^4 \qquad \text{per unit area,}$$

where terms of higher order have been neglected.

The pinning force,

$$F_p = -\frac{dW}{dz} = -2\alpha z + 4\beta z^3 \tag{3.2-1}$$

and

$$\frac{dF_p}{dz} = -\frac{d^2W}{dz^2} = -2\alpha + 12\beta z^2 \tag{3.2-2}$$

W(z) is illustrated in figure 3.2-1.

We see from eqs.(3.2-1) and (3.2-2) that the force is maximum when

$$z_0 = \left(\frac{\alpha}{6\beta}\right)^{\frac{1}{2}} \tag{3.2-3}$$

Expanding the potential about this position of maximum restoring force, if $z = z_0 + \varepsilon$, where ε is a small quantity,

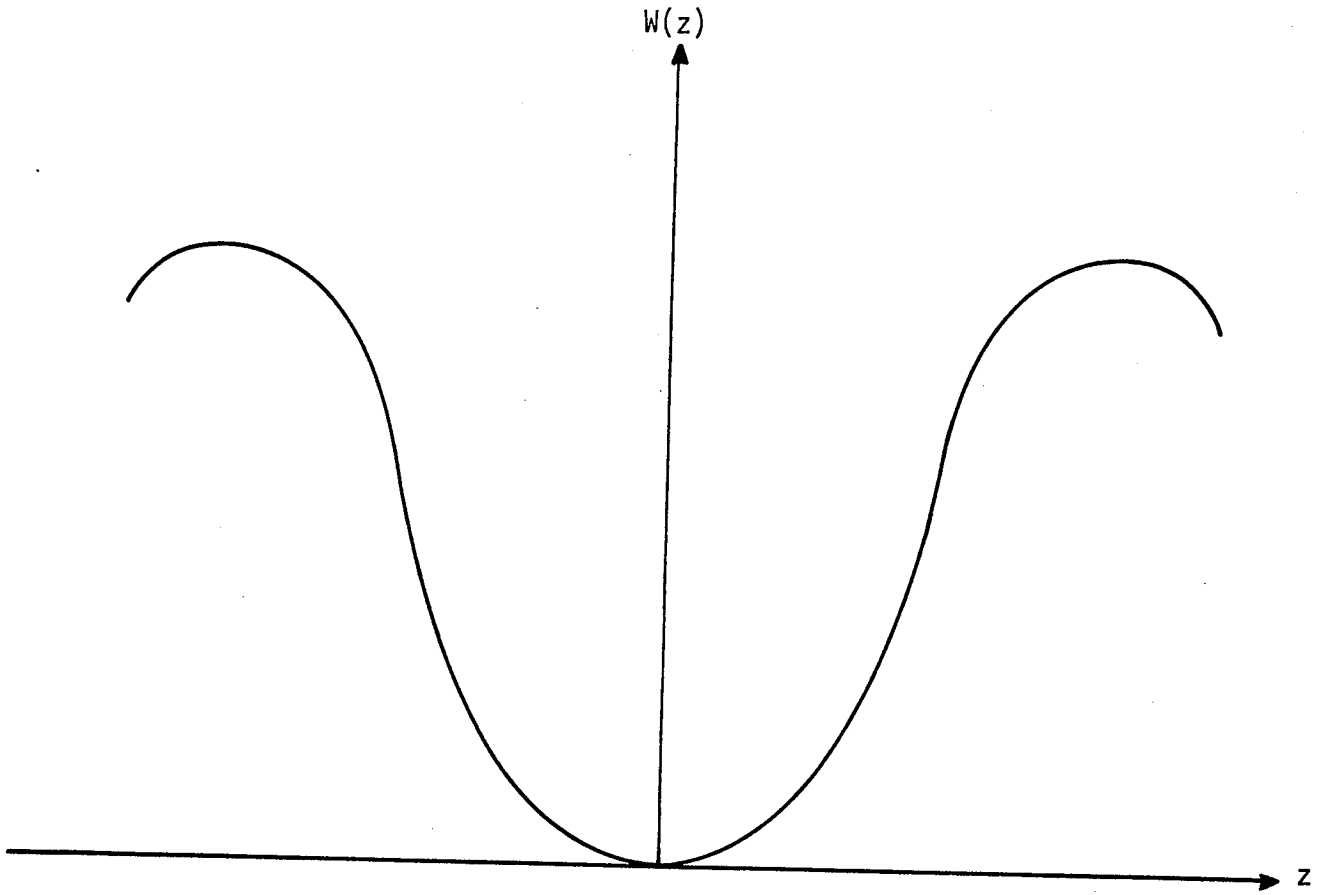

Figure 3.2-1 - The variation of W(z) with position.

$$W(z) = \alpha(z_0 + \varepsilon)^2 - \beta(z_0 + \varepsilon)^4$$

and

$$W(z) = \alpha(z_0^2 + 2z_0\varepsilon + \varepsilon^2) - \beta(z_0^4 + 4z_0^3\varepsilon + 6z_0^2\varepsilon^2 + 4z_0\varepsilon^3 + \varepsilon^4)$$

Expansion about z_0 yields a potential,

$$W_{z_0}(\varepsilon) = (2\alpha z_0 - 4\beta z_0^3)\varepsilon + (\alpha - 6\beta z_0^2)\varepsilon^2 - 4\beta z_0\varepsilon^3 - \beta\varepsilon^4$$

Substitution for z_0 from eq.(3.2-3) causes the coefficient of the second order term to vanish. Also, since ε is small, $\varepsilon^4 << 1$ and can be neglected.

The interaction potential may therefore be rewritten as an odd powered function with respect to an origin at the point of maximum force:

$$V(z) = F(z + b - \frac{z^3 + b^3}{3b^2}), \qquad (3.2\text{-}4)$$

the interaction energy per unit volume.

$$\frac{dV}{dz} = F(1 - \frac{z^2}{b^2}) \qquad (3.2\text{-}5)$$

$V(z)$ and $\frac{dV}{dz}$ have been sketched in figures 3.2-2 and 3.2-3 respectively.

The restoring force, $-\frac{dV}{dz}$ is therefore parabolic and as expected, greatest when $z = 0$.

V has a maximum at $z = +b$ and a minimum at $z = -b$.

Thus, a function V as described by eq.(3.2-4) is appropriate for the interaction energy of a domain wall pinned at $z = -b$.

b is called the interaction parameter and F the force constant.

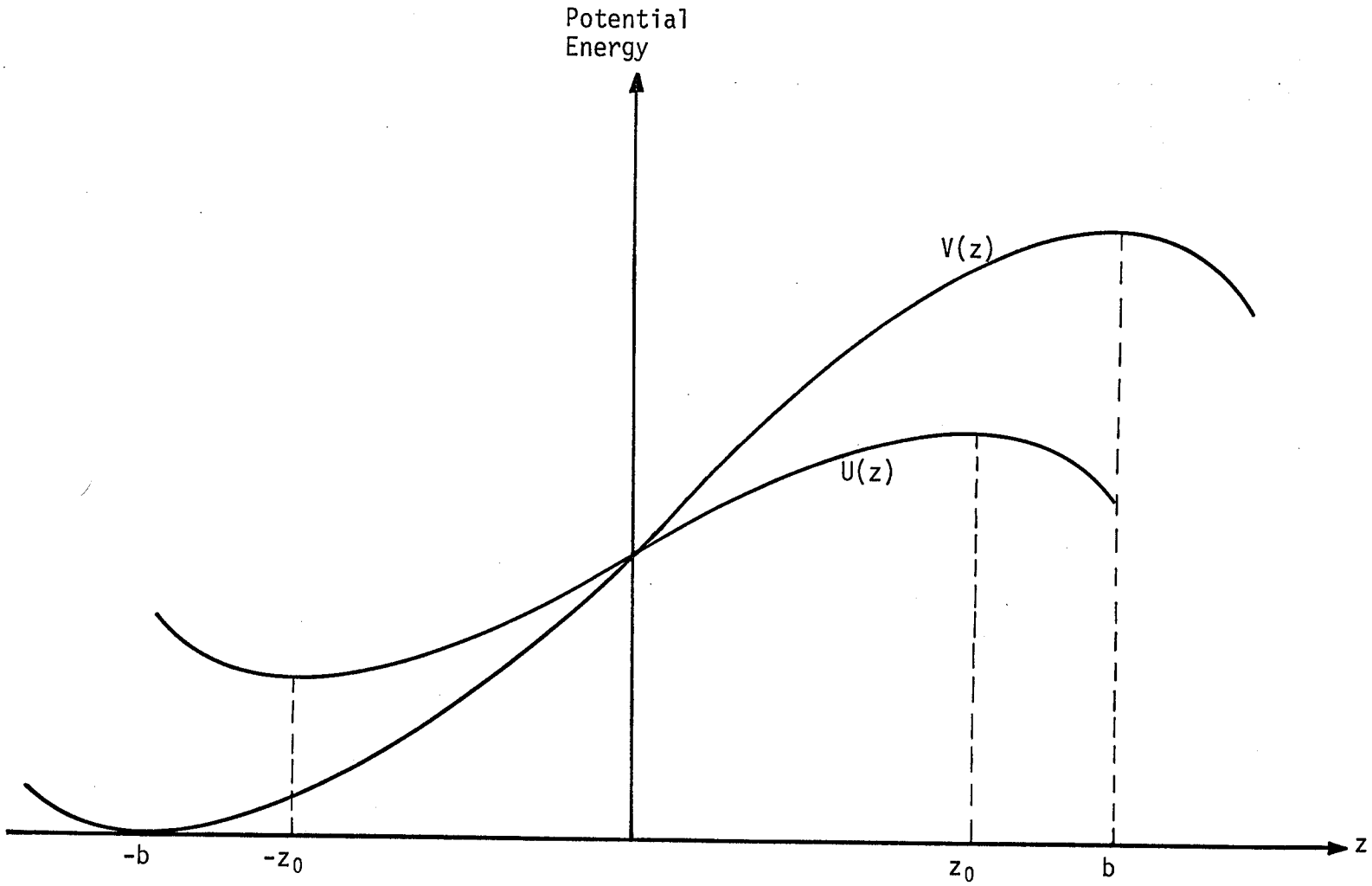

Figure 3.2-2 - The variation with position of potential energy with and without the presence of a field.

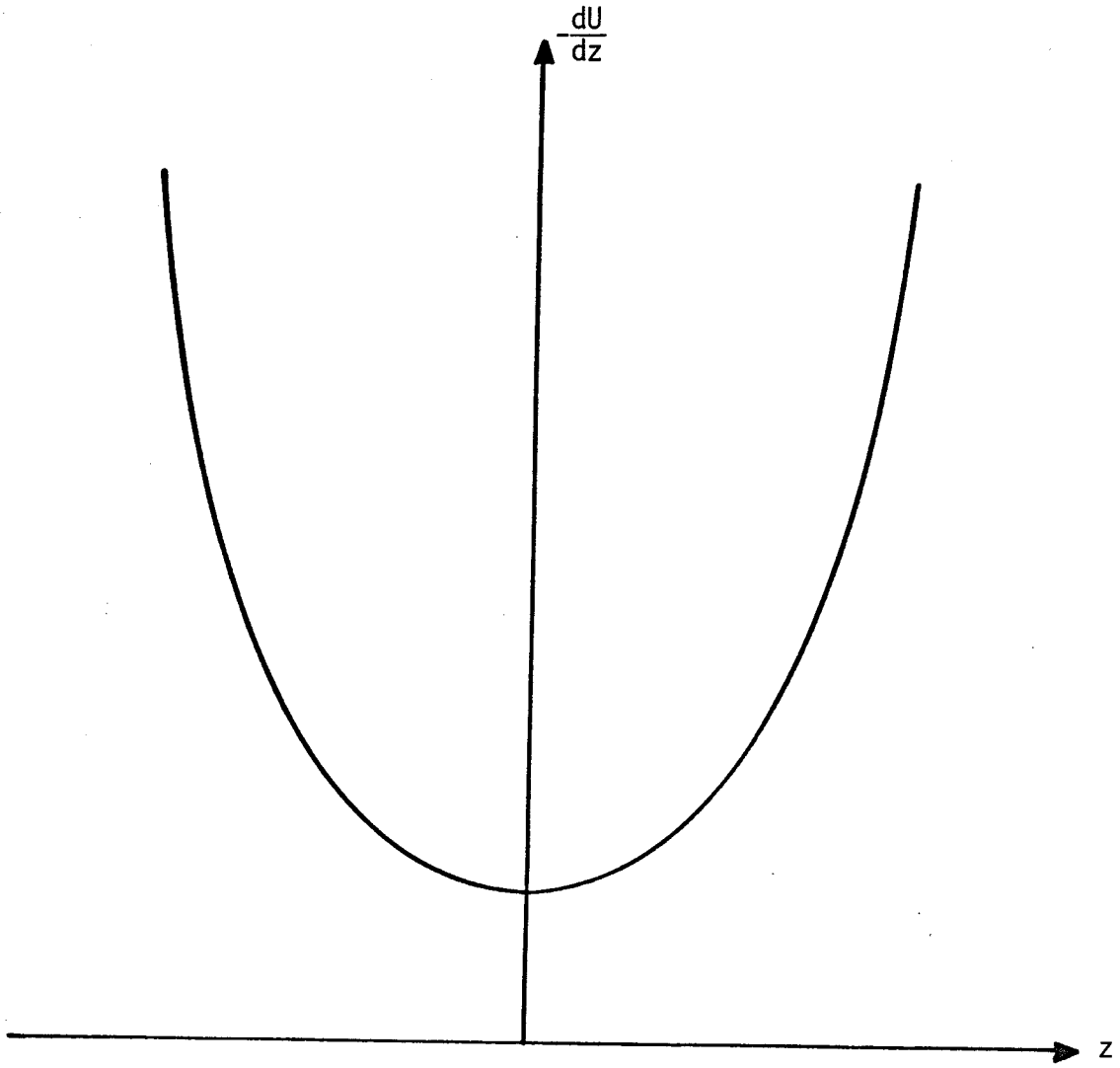

Figure 3.2-3 - The variation of the pinning force with position.

3.3 Effect of a Magnetic Field

Looking at the form of V, we see that escape from the pinning site will only be possible when the wall acquires the energy to rise to the level of the maximum at z = b. Consider therefore the effect of an applied magnetic field.

If the field is of magnitude H and the wall is displaced in the z-direction, the energy per unit area is now modified to read:

$$U = V - 2HI(z + b) \tag{3.3-1}$$

where I is the spontaneous magnetization per unit volume of the material.

Equilibrium values of z are obtained by differentiating U with respect to z and we get:

$$\frac{dU}{dz} = F\left(1 - \frac{z_0^2}{b^2}\right) - 2HI = 0 \tag{3.3-2}$$

$$\frac{d^2U}{dz^2} = \frac{2Fz}{b^2} = 0$$

at the point of inflection which is the position of maximum slope.

From eq.(3.3-1)

$$z_0 = \pm b\frac{(F - 2HI)^{\frac{1}{2}}}{F^{\frac{1}{2}}} \tag{3.3-3}$$

which are stationary states in the presence of the field.

The absolute zero coercive field, H_0 is the smallest field at which the wall can break free of the pin in the absence of thermal

activation. This will occur when the wall is in a position such that it has no energy barriers to climb and this condition is met when the energy maximum becomes a point of inflection,

$$\frac{d^2U}{dz^2} = 0.$$

Here $z_o = 0$ (from eq.(3.3-3)) and from this point onwards, the wall is free to slide down the negative slope region of the energy curve.

From eq.(3.3-1) therefore:

$$F = 2H_0 I \ ,$$

$$\text{or} \quad H_0 = \frac{F}{2I} \qquad (3.3\text{-}4)$$

The effect of the magnetic field, therefore, is to reduce the height difference between the maximum and minimum energy states of U, as shown in figure 3.2-2.

Since these states are, by substituting from eqs.(3.2-4), (3.3-3) and (3.3-4) in eq.(3.3-1),

$$U_{max} = \frac{2}{3}Fb\left(1 - \frac{H}{H_0}\right)^{\frac{3}{2}}$$

and

$$U_{min} = -\frac{2}{3}Fb\left(1 - \frac{H}{H_0}\right)^{\frac{3}{2}} \ ,$$

their difference, which is the energy barrier the wall must overcome for escape is:

$$E = \frac{4}{3}Fb\left(1 - \frac{H}{H_0}\right)^{\frac{3}{2}} \qquad (3.3\text{-}5)$$

For an area A, the barrier is $\frac{4}{3}FAb\left(1 - \frac{H}{H_0}\right)^{\frac{3}{2}}$. We see that the applied field reduces the height of the energy barrier.

For the wall to spring free, the barrier must be overcome. However, if A is large, the barrier will be large and the applied field must approach the absolute zero coercive field for escape to occur.

This however, neglects the possibility of wall curvature and if such a phenomenon is considered, the wall may escape at a field lower than the absolute zero coercive field.

3.4 Wall Curvature

The domain wall may be treated as a membrane with surface tension corresponding to the wall energy γ per unit area.

Suppose that under the action of the magnetic field, a blister of cylindrical symmetry about the z-axis forms on the wall. The forces acting at a point on the blister are therefore the surface tension force per unit area $\gamma(R_1^{-1} + R_2^{-1})$, where R_1 and R_2 are the principal radii of curvature at the point, the pinning force $-\frac{dV}{dz}$ which has been discussed in section 3.2 and the magnetic force of 2HI per unit area. The pinning and surface tension forces try to restrain the blister, while the magnetic force tries to enhance its growth.

Consider a point on the blister defined by cylindrical co-ordinates (r,z). Let the tangent to the blister at this point make an angle θ with the plane of the unblistered wall (figure 3.4-1).

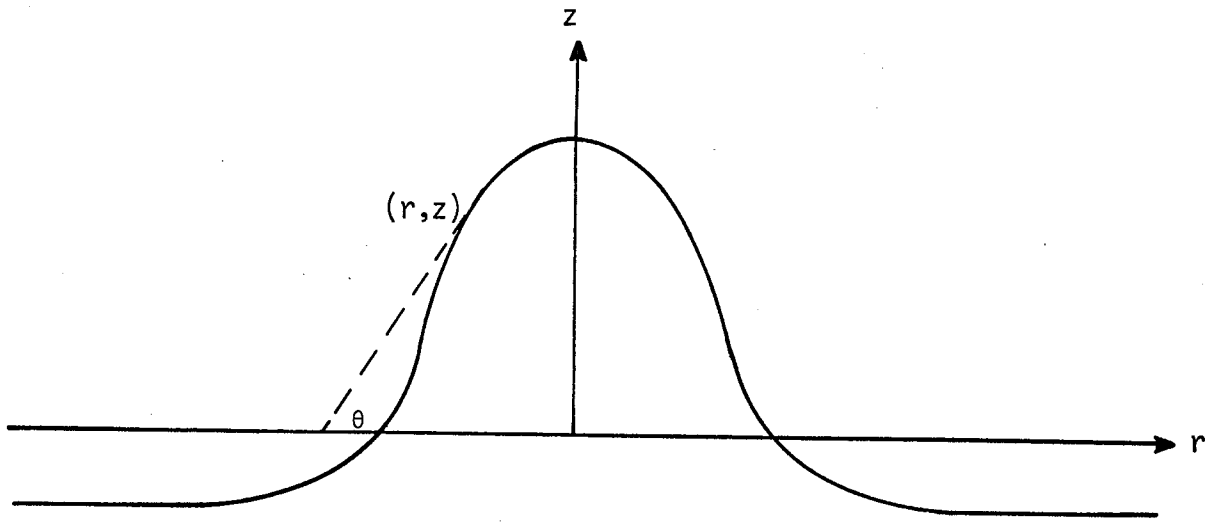

Figure 3.4-1 - The 'blister' in cylindrical coordinates

Then, for an element of blister surface, if the forces per unit area are resolved in the z-direction, the equilibrium condition is:

$$F\left(1 - \frac{z^2}{b^2}\right) + \gamma\left(R_1^{-1} + R_2^{-1}\right)\cos\theta = 2HI\cos\theta \qquad (3.4\text{-}1)$$

Now, $$\cos\theta = \left[1 + (z')^2\right]^{-\frac{1}{2}} \qquad (3.4\text{-}2)$$

where $$z' = \frac{dz}{dr}$$

Also, when the curvature is expressed in cylindrical co-ordinates,

$$R_1^{-1} + R_2^{-1} = -z''\left[1 + (z')^2\right]^{-\frac{3}{2}} - \frac{z'}{r} \qquad (3.4\text{-}3)$$

where $$z'' = \frac{d^2z}{dr^2}$$

Substituting from eqs.(3.4-2) and (3.4-3) into (3.4-1),

$$\gamma\left\{z''\left[1 + (z')^2\right]^{-\frac{3}{2}} + \frac{z'}{r}\right\} + 2HI = F\left(1 - \frac{z^2}{b^2}\right)\left[1 + (z')^2\right]^{\frac{1}{2}} \qquad (3.4\text{-}4)$$

Assume that the slope of the blister is gradual. i.e. that z' is small and $(z')^2 \ll 1$.

Then, eq.(3.4-4) reduces to:

$$z'' + \frac{z'}{r} = \frac{F - 2HI}{\gamma} - \frac{Fz^2}{\gamma b^2} \qquad (3.4\text{-}5)$$

This second order differential equation describes the wall displacement z as a function of r when the following boundary conditions

are taken into account.

When the wall is pinned at large distance (i.e. as $r \to \infty$) from an isolated blister,

$$z' = z'' = 0$$

Substituting this into eq.(3.4-5) gives

$$z = \frac{-b(F - 2HI)^{\frac{1}{2}}}{F^{\frac{1}{2}}} ,$$

which is the position for minimum energy as seen in eq.(3.3-3).

Also, as $r \to 0$, $z' = 0$ and due to the cylindrical symmetry of the blister, $z'' = \frac{z'}{r}$. $z = z_1$, the height of the blister.

The boundary conditions are therefore

$$\left.\begin{aligned} z'' &= z' = 0 \\ z &= \frac{-b(F - 2HI)^{\frac{1}{2}}}{F^{\frac{1}{2}}} \end{aligned}\right\} \text{ as } r \to \infty \qquad (3.4\text{-}6)$$

$$\left.\begin{aligned} z'' &= \frac{z'}{r} \\ z' &= 0 \\ z &= z_1 \end{aligned}\right\} \text{ as } r \to 0 \qquad (3.4\text{-}7)$$

For convenience in solving the differential equation, the following substitution is employed:

$$Z = b^{-1} F^{\frac{1}{2}} (F - 2HI)^{-\frac{1}{2}} z \qquad (3.4\text{-}8)$$

$$R = (\gamma b)^{-\frac{1}{2}} F^{\frac{1}{4}} (F - 2HI)^{\frac{1}{4}} r \qquad (3.4\text{-}9)$$

Both Z and R and dimensionless.

Eqs.(3.4-5) to (3.4-7) may then be rewritten as:

$$Z'' + \frac{Z'}{R} = 1 - Z^2 \qquad (3.4\text{-}5a)$$

$$\left.\begin{aligned} Z'' &= Z' = 0 \\ Z &= 1 \end{aligned}\right\} \text{ as } R \to \infty \qquad (3.4\text{-}6a)$$

$$\left.\begin{aligned} Z'' &= \frac{Z'}{R} \\ Z' &= 0 \\ Z &= Z_1 \end{aligned}\right\} \text{ as } R \to 0 \qquad (3.4\text{-}7a)$$

3.5 Activation Energy of the Blister

The activation energy required to produce the blister consists of the extra wall energy to create the blister, the field energy and the interaction energy.

The wall energy,

$$E_\gamma = \gamma \int_0^\infty (\sec\theta - 1)\, 2\pi r dr$$

Now, $\sec\theta = [1 + (z')^2]^{\frac{1}{2}}$

However, since $(z')^2 << 1$,

$$\sec\theta = 1 + \frac{1}{2}(z')^2$$

where higher order terms have been neglected.

Therefore,

$$E_\gamma = \pi\gamma\int_0^\infty (z')^2 \, r dr \qquad (3.5\text{-}1)$$

The field and interaction energies are given by:

$$E_I = \int_0^\infty U(z) \, 2\pi r dr$$

$$E_I = 2\pi\int_0^\infty \left[(F - 2HI)(z - z_0) - \frac{F(z^3 - z_0{}^3)}{3b^2}\right] r dr \qquad (3.5\text{-}2)$$

where z_0 is the wall position as $r \to \infty$, given by eq.(3.4-6).

The activation energy, $E = E_\gamma + E_I$, and when eqs.(3.5-1) and (3.5-2) are expressed in the reduced co-ordinates (3.4-8) and 3.4-9)

$$E = 2\pi\gamma b^2 \left(1 - \frac{2HI}{F}\right) \int_0^\infty \left[\frac{2}{3} + Z - \frac{Z^3}{3} + \frac{1}{2}(Z')^2\right] R dR \qquad (3.5\text{-}3)$$

The integral in eq.(3.5-3) can be solved numerically, utilising the differential eq.(3.4-5a) and the boundary conditions (3.4-6a) and (3.4-7a). It is independent of the constants of the material and yields a pure number N.

Eq.(3.5-3) may therefore be rewritten as

$$E = 2\pi N\gamma b^2 \left(1 - \frac{2HI}{F}\right) \qquad (3.5\text{-}4)$$

where

$$N = \int_0^\infty \left[\frac{2}{3} + Z - \frac{Z^3}{3} + \frac{1}{2}(Z')^2\right] R dR \qquad (3.5\text{-}5)$$

Differentiating (3.5-4) with respect to field, the energy barrier

distribution

$$\left(\frac{\partial E}{\partial H}\right)_T = \frac{-4\pi N I \gamma b^2}{F} \qquad (3.5\text{-}6)$$

is obtained.

3.6 Evaluation of the Integral

The integral has to be solved numerically in the absence of an analytical solution for eq.(3.5-5).

Choosing a value of Z at R = 0, Z = Z_1, the boundary conditions (3.4-7a) and eq.(3.4-5a) give

$$Z'' = \frac{1 - Z_1^2}{2}$$

Z and Z' are then Taylor expanded about R to give

$$Z(R + h) = Z(R) + hZ'(R) + \frac{h^2 Z''(R)}{2} + \frac{h^3 Z''(R)}{6} \qquad (3.6\text{-}1)$$

$$Z'(R + h) = Z'(R) + hZ''(R) + \frac{h^2 Z''(R)}{2} \qquad (3.6\text{-}2)$$

where h is a small interval in R.

Eq.(3.4-5a) when differentiated with respect to R gives

$$Z''' + \frac{Z''}{R} - \frac{Z'}{R^2} = 1 - 2ZZ' \qquad (3.6\text{-}3)$$

An initial value of Z_1 was chosen. Then, using eqs.(3.6-1) to (3.6-3), values of Z, Z' and Z''', and from the differential eq.(3.4-5a) the value of Z'' were obtained at R = h. These values were then taken as

the starting points and values of Z and its derivatives were calculated at R = 2h. The procedure was repeated until a table of values of Z and its first three derivatives had been obtained. The boundary condition on Z at large R, Z = -1, had to be satisfied. Z_1 was therefore varied coarsely until this condition was met. It then had to be fine tuned until it gave non-oscillatory solutions at large R. The starting point proved to be very sensitive as even small changes gave solutions that were oscillatory rather than asymptotic.

The integral (3.4-5) was numerically calculated using the table generated by the proper value of Z_1.

The value of Z_1 was 3.7890.

R was varied in intervals of 0.05 (i.e. h = 0.05)

When the calculation procedure was reversed using a large value of R as the starting point Z_1 was obtained as 3.7894 and Z_1' as 0.001.

The calculated profile of the blister is shown in figure 3.6-1. It is cylindrically symmetric about the Z-axis.

From the calculations, N = 4.929.

3.7 Thermal Activation for Unpinning

Using reaction rate theory, Glasstone, Laidler and Eyring (1941) have shown that when a process has an activation energy E, at a temperature T and the activation energy for the process to reverse itself is E_2 (figure 3.7-1), then the characteristic relaxation time τ of the process is given by:

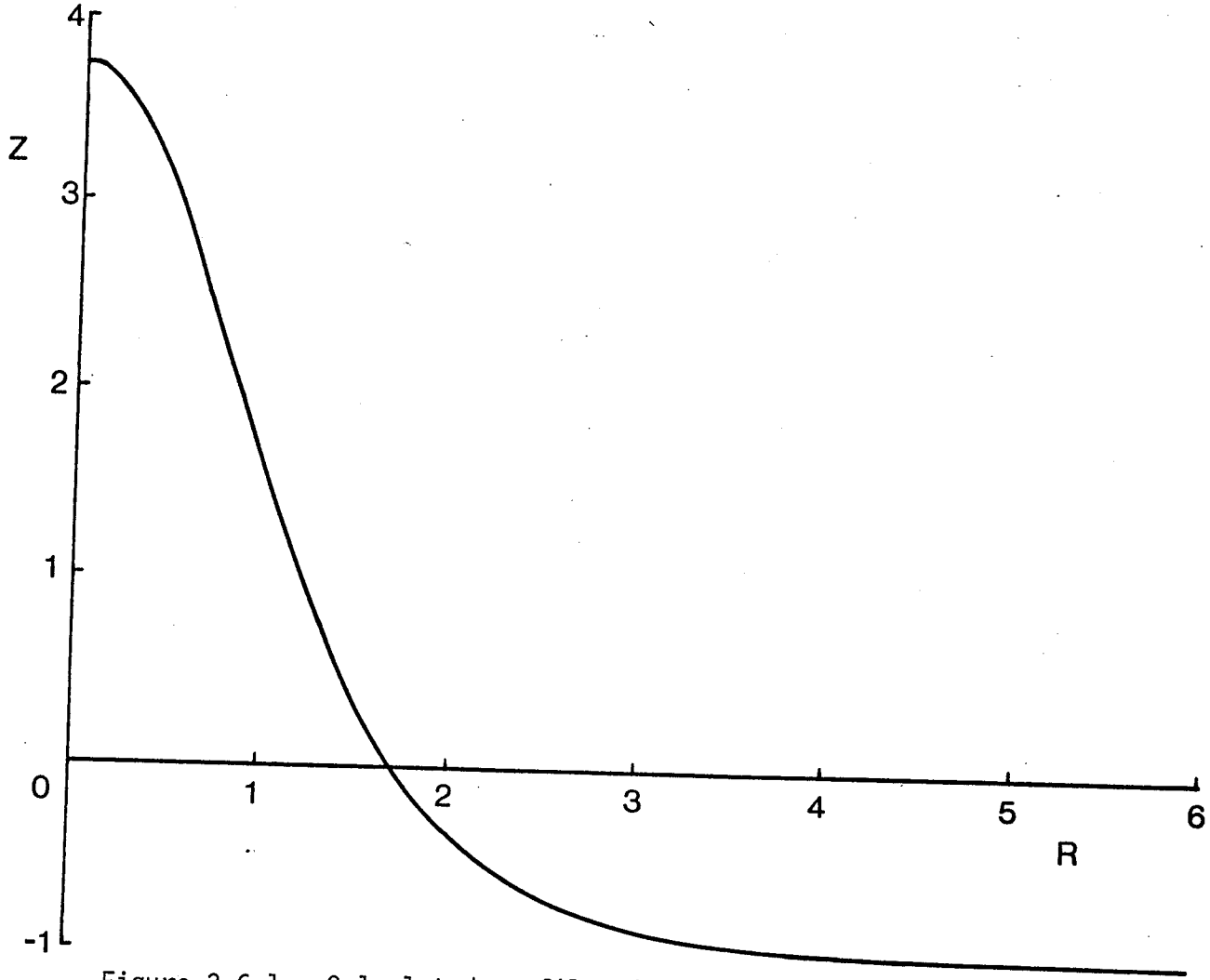

Figure 3.6-1 - Calculated profile of the 'blister'.

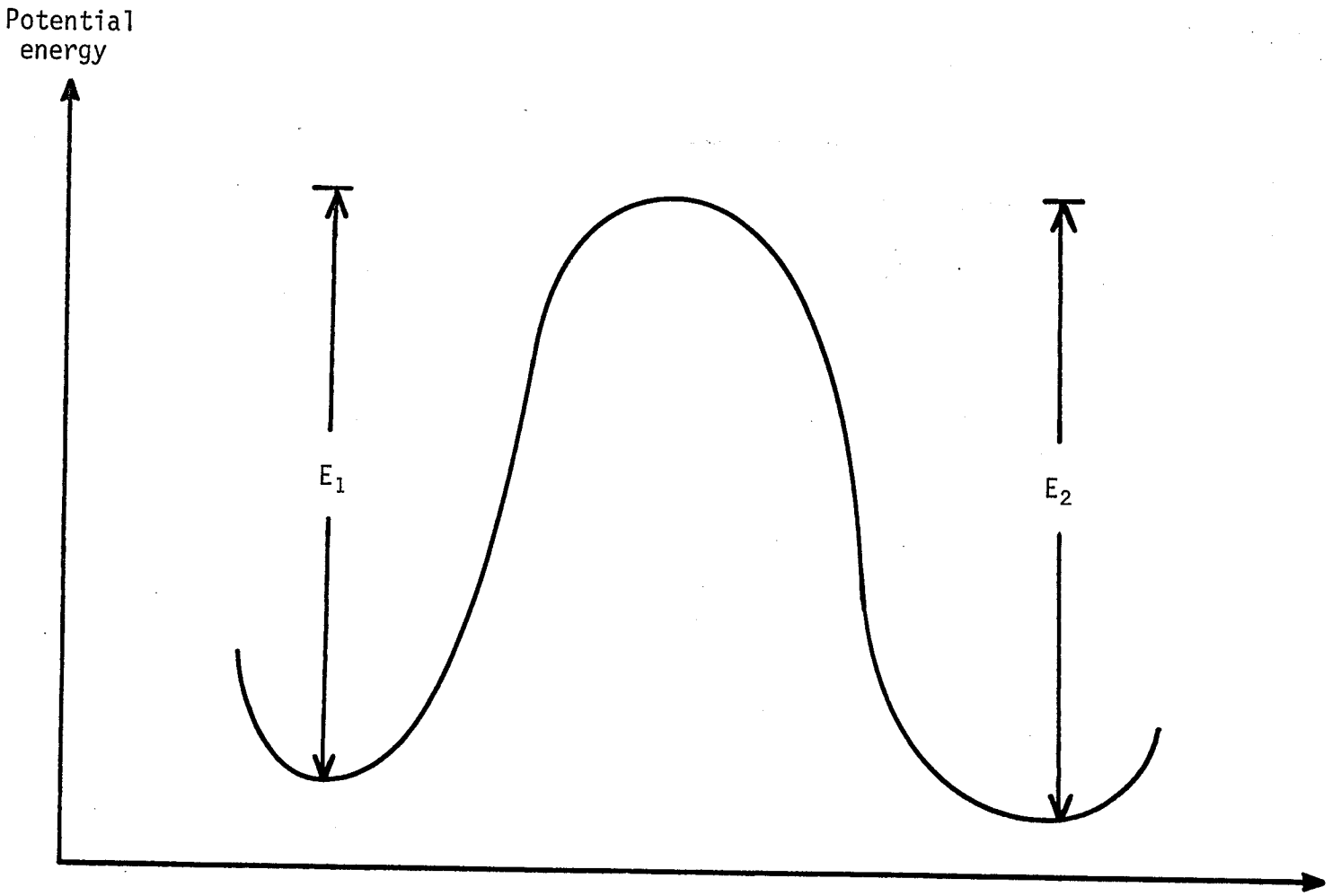

Figure 3.7-1 - Activation energies for forward and reverse processes.

$$\tau^{-1} = C\left[\exp\left(\frac{-E_1}{kT}\right) - \exp\left(\frac{-E_2}{kT}\right)\right]$$

where C is a constant known as the frequency factor.

As energy appears in an exponential term in the above expression, E_2 need only be slightly larger than E_1 for the second term to become negligibly small.

For example, if $E_2 = 1.2E_1$,

$$\exp\left(\frac{-E_2}{kT}\right) = 0.007 \exp\left(\frac{-E_1}{kT}\right)$$

For a ferromagnet, the barriers to thermal activation are such that the term in E_2 may usually be neglected in the presence of a field.

Bean and Livingston (1959) have shown that if E is the energy required for a domain wall to overcome an energy barrier and τ is the time required for thermal activation to take place,

$$C \simeq \exp(25)\text{Hz}$$

in the expression

$$\tau^{-1} = C \exp\left(\frac{-E}{kT}\right) \qquad (3.7\text{-}1)$$

A characteristic measuring time for after-effect is 1 second.

Then, from eq.(3.7-1)

$$E \simeq 25kT,$$

the activation energy.

Thus, for the wall to escape as a result of thermal activation, eq.(3.5-4) gives:

$$2\pi N\gamma b^2\left(1 - \frac{2H_c I}{F}\right) = 25kT$$

and $$H_c = H_0(1 - \frac{25kT}{2\pi N\gamma b^2}) \ , \qquad (3.7\text{-}2)$$

the coercive field with thermal activation.

We see, therefore, that when thermal activation is taken into account, the coercive field is lowered.

CHAPTER 4

MICROMAGNETIC CALCULATION

4.1 Introduction

4.1.1 Basis of the Model

The magnetization vector in a 180° domain wall rotates, as shown in figure 1.1-1. This rotation will be in either a clockwise or anticlockwise direction. Thus, the magnetization in neighbouring walls can have like or opposite sense of rotation. Pairs of walls having like sense will be called 'winding walls' and those with opposite sense will be known as 'unwinding walls'.

On application of a field, domains which are parallel to the field will expand, while those which are antiparallel will contract. Neighbouring 180° walls will therefore approach one another and while unwinding walls will annihilate each other, winding walls will become more and more tightly compressed, forming a 360° wall which springs back into two 180° walls when the field is removed.

As discussed in previous chapters, magnetic hardening may be the result of the pinning of domain walls by inhomogeneous regions of lower wall energy within the material. The effect of these inhomogeneities is to trap the tightly wound 360° wall which then acts

as a nucleation centre for magnetization reversal. The coercive field of such a configuration is the field that is required to separate the two 180° walls and to allow each of them to escape from the pin.

In this chapter, the interaction between a 360° domain wall and a planar inhomogeneity is considered. A micromagnetic model is used to derive an expression for wall energy in terms of the anisotropy, the exchange interaction and the field interaction. By minimizing the energy, the condition for wall unpinning is obtained.

4.1.2 Applicability of the Model

This model can be applied to any material where the domain wall can move unhindered within the grain itself. Livingston (1973) used Kerr microscopy to show that this was indeed the case for sintered $SmCo_5$. In the present study it was observed that it was possible to magnetize a virgin specimen to over 65% of its saturation magnetization and then obtain almost complete demagnetization by turning off the field (section 6.5.3). Also, demagnetizing factors calculated from the dimensions of the specimen were within a few percent of those obtained by magnetization measurements (section 6.5.2). Further confirmation is found in the measurements of the Barkhausen effect (chapter 8). All

this experimental evidence implies that there is impedance free movement of domain walls in over 82% of the volume of the sintered $SmCo_5$ specimens that were studied. Pinning must therefore be absent within grains and the model can be applied with confidence to sintered $SmCo_5$ alloys with planar Sm_2Co_{17} inhomogeneities at grain boundaries.

4.2 Zero Torque Condition

Consider the i^{th} element of a domain wall which is parallel to the xy plane. Suppose it makes an angle θ_i with the z-direction and also suppose that the spins are sited at a spacing 'a' along this direction as in figure 4.2-1.

Let the anisotropy energy of the material per unit volume be 'K' and let its magnetization be 'I' per unit volume.

Then, if there are N spins per unit volume, the energy of the i^{th} spin element is:

$$E_i = \frac{1}{N}K\sin^2\theta_i + Js^2[1 - \cos(\theta_i-\theta_{i-1})] + Js^2[1 - \cos(\theta_i-\theta_{i+1})] + \frac{1}{N}IH(1 - \cos\theta_i) \ , \qquad (4.2\text{-}1)$$

where the origins of these terms are as follows.

Since we are only dealing with uniaxial materials, the anisotropy term is of the form:

$$K_1\sin^2\theta + K_2\sin^4\theta \ ,$$

where in this case the easy direction coincides with the z-axis and

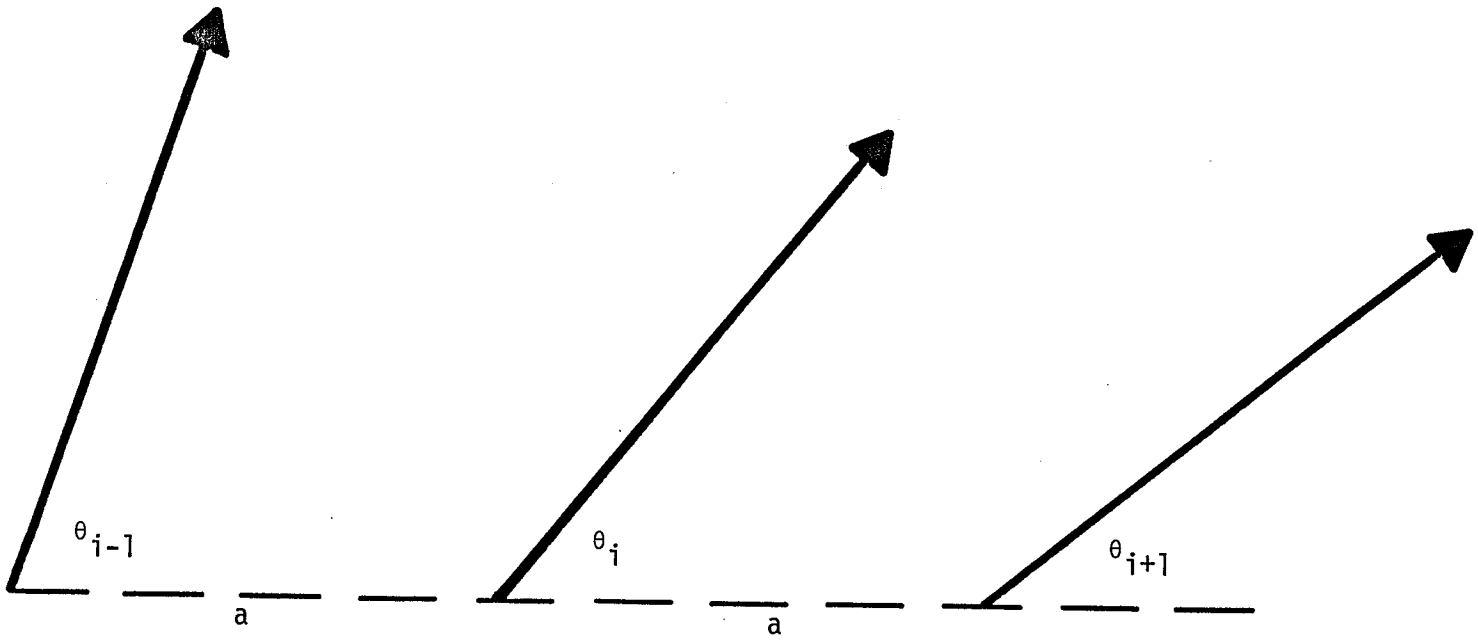

Figure 4.2-1 - Alignment of adjacent spins at spacing 'a' in a domain wall.

where θ is the angle that the moment makes with the easy direction. The fourth power term is dropped because $K_2 << K_1$.

The exchange interaction is only considered between nearest neighbours. Thus, when s is the spin and J is the usual exchange integral, we get the second and third terms.

The final term is the field interaction energy where we have assumed a field in the easy direction of the crystal.

The torque on this element is obtained by differentiating eq.(4.2-1) with respect to θ_i:

$$\frac{\partial E_i}{\partial \theta_i} = \frac{2K}{N}\sin\theta_i\cos\theta_i + Js^2[\sin(\theta_i-\theta_{i-1}) + \sin(\theta_i-\theta_{i+1})] + \frac{I}{N}H\sin\theta_i \qquad (4.2\text{-}2)$$

For the wall to be at rest, each element of spin must have zero torque.

$$\text{i.e. } \frac{\partial E_i}{\partial \theta_i} = 0$$

and

$$2K\sin\theta_i\cos\theta_i - Js^2N[\sin(\theta_i-\theta_{i-1}) + \sin(\theta_i-\theta_{i+1})] + IH\sin\theta_i = 0 \qquad (4.2\text{-}3)$$

Since the difference in inclination between adjacent spins must be small, we can replace $\sin(\theta_i-\theta_{i-1})$ by $(\theta_i-\theta_{i-1})$ and $\sin(\theta_i-\theta_{i+1})$ by $(\theta_i-\theta_{i+1})$.

If we Taylor expand θ_{i+1} and θ_{i-1} ,

$$\theta_{i+1} = \theta_i + a\frac{d\theta_i}{dz} + \frac{a^2 d^2\theta_i}{2\ dz^2} + \ldots.$$

and $$\theta_{i-1} = \theta_i - a\frac{d\theta_i}{dz} + \frac{a^2 d^2\theta_i}{2\ dz^2} + \ldots.$$

Neglecting higher powers in a, these are substituted into eq.(4.2-3) to give:

$$Js^2a^2N\frac{d^2\theta_i}{dz^2} = 2K\sin\theta_i\cos\theta_i + IH\sin\theta_i \qquad (4.2\text{-}4)$$

In effect we are now moving towards an approximation of a continuum by making 'a' small.

Multiplying both sides of eq.(4.2-4) by $d\theta_i$ and integrating, we get:

$$\frac{1}{2}Js^2a^2N\left(\frac{d\theta_i}{dz}\right)^2 = K\sin^2\theta_i - IH\cos\theta_i + \text{constant} \qquad (4.2\text{-}5)$$

If the exchange constant,

$$A = \frac{1}{2}Js^2a^2N \quad ,$$

eq.(4.2-5) reads:

$$A\left(\frac{d\theta}{dz}\right)^2 = K\sin^2\theta - IH\cos\theta + c \quad , \qquad (4.2\text{-}6)$$

the condition for a stable domain wall and where c is a constant.

4.3 Contributions to the Wall Energy

The origins of the various contributions to the energy of the domain wall have been discussed in the previous section.

For a domain wall lying parallel to the xy plane, the energy per unit area is given by:

$$E = \int[K\sin^2\theta + A(\frac{d\theta}{dz})^2 - IH\cos\theta + \text{constant}]dz \qquad (4.3\text{-}1)$$

The limits of the integral are the dimensions of wall width over which the energy is to be calculated.

4.4 Energy of the Domain Wall and Boundary Condition

Figure 4.4-1 shows how the spins are distributed with respect to position within the domain wall in the presence of a planar inhomogeneity of thickness Y and parallel to the xy plane. Let the angles of spin at the matrix-inhomogeniety boundaries be θ_1 and $2\pi-\theta_1$. Assume that $\frac{d\theta}{dz} \to 0$ as $\theta \to 0$ at $z \to -\infty$ and as $\theta \to 2\pi$ at $z \to +\infty$

Therefore, from eq.(4.2-6), c=IH in the matrix phase.

We have therefore,

$$A_1(\frac{d\theta}{dz})^2 = K_1\sin^2\theta + I_1H(1-\cos\theta) \qquad (4.4\text{-}1)$$

where the suffix '1' will be used for the matrix parameters and suffix '2' for the parameters belonging to the inhomogeneity.

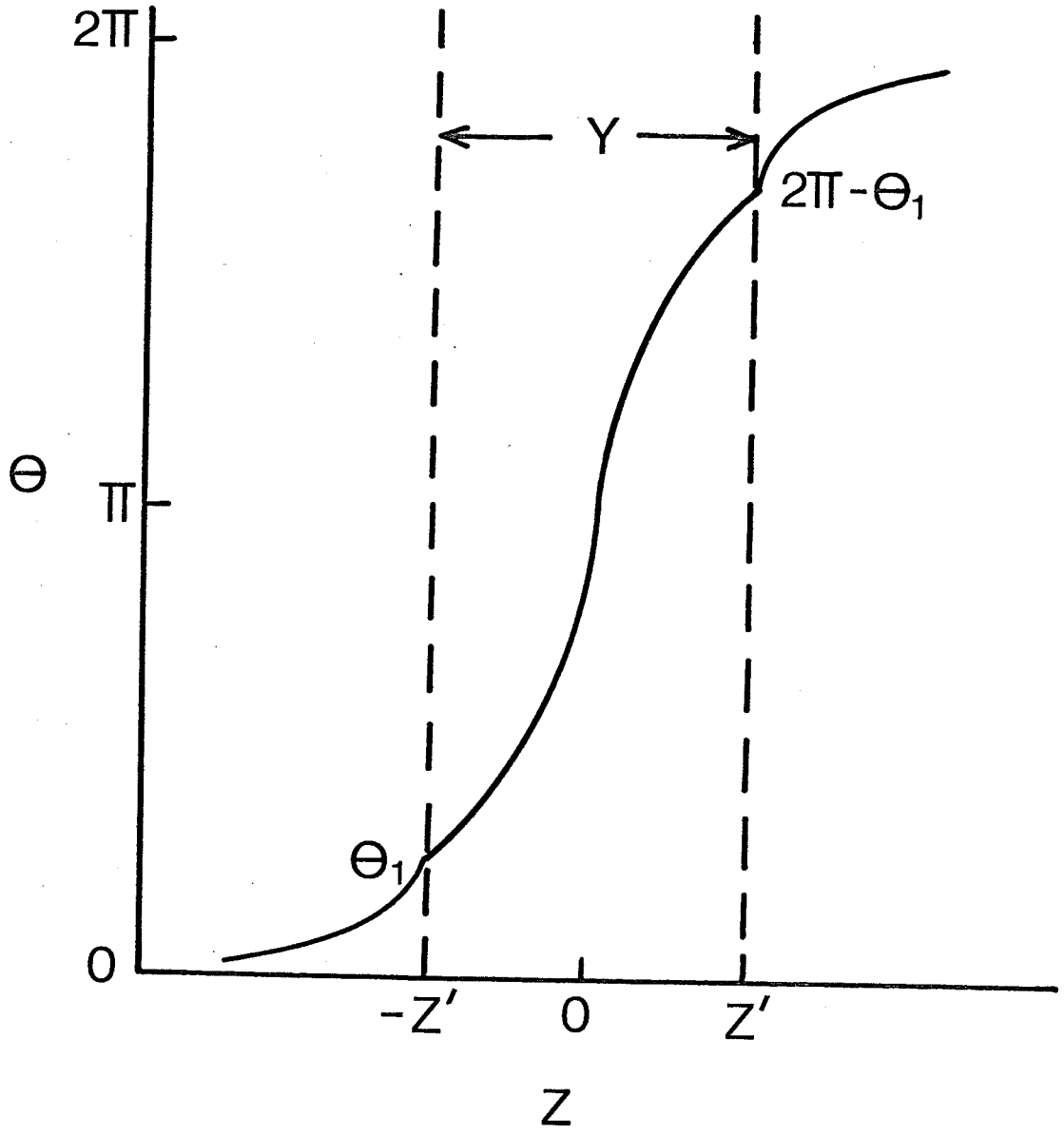

Figure 4.4-1 - Variation of spin angle with position for a 360° domain wall in the presence of a planar inhomogeneity.

From eq.(4.4-1),

$$dz = A_1^{\frac{1}{2}}[K_1\sin^2\theta + I_1H(1-\cos\theta)]^{-\frac{1}{2}}\, d\theta \qquad (4.4\text{-}2)$$

The energy of the portion of the wall within the matrix is:

$$E_1 = 2\int_{-\infty}^{-z'} [K_1\sin^2\theta + A_1\left(\frac{d\theta}{dz}\right)^2 - I_1H\cos\theta + \text{constant}]\, dz \qquad (4.4\text{-}3)$$

$$= 2\int_{-\infty}^{-z'} [2K_1\sin^2\theta + 2I_1H(1-\cos\theta)]\, dz, \qquad (4.4\text{-}4)$$

where the energy zero has been defined by setting the constant of eq.(4.2-6) equal to I_1H.

Substituting for dz from eq.(4.4-2) into eq.(4.4-4),

$$E_1 = 4A_1^{\frac{1}{2}} \int_0^{\theta_1} [K_1\sin^2\theta + I_1H(1-\cos\theta)]^{\frac{1}{2}}\, d\theta \qquad (4.4\text{-}5)$$

Similarly, inside the inhomogeneity,

$$E_2 = 4A_2^{\frac{1}{2}} \int_{\theta_1}^{\pi} [K_2\sin^2\theta - I_2H\cos\theta + c]^{\frac{1}{2}} d\theta + Y[I_2H - c] \qquad (4.4\text{-}6)$$

The last term arises because the energy zero is defined at $\theta = 0$ and $\frac{d\theta}{dz} = 0$.

Eqs.(4.4-5) and (4.4-6) are written in reduced terms with $e = \frac{E}{K}$, $h = \frac{IH}{2K}$ and $a = \frac{A}{K}$.

Then,

$$e_1 = 4a_1^{\frac{1}{2}} \int_0^{\theta_1} [\sin^2\theta + 2h_1(1-\cos\theta)]^{\frac{1}{2}} \, d\theta \qquad (4.4\text{-}5a)$$

and

$$e_2 = 4a_2^{\frac{1}{2}} \int_{\theta_1}^{\pi} [\sin^2\theta - 2h_2\cos\theta + c]^{\frac{1}{2}} \, d\theta + 2Y(h_2 - \tfrac{1}{2}c) \qquad (4.4\text{-}6a)$$

where the constant c in eq.(4.4-6a) is a new constant.

If the total energy is

$$E = E_1 + E_2 \, ,$$

the variation in energy with respect to θ_1 ,

$$\frac{dE}{d\theta_1} = \frac{\partial E}{\partial \theta_1} + \frac{\partial E}{\partial c}\cdot\frac{dc}{d\theta_1}$$

i.e.

$$\frac{dE}{d\theta_1} = K_1\frac{\partial e_1}{\partial \theta_1} + K_2\frac{\partial e_2}{\partial \theta_1} + \left(K_1\frac{\partial e_1}{\partial c} + K_2\frac{\partial e_2}{\partial c}\right)\frac{dc}{d\theta_1} \qquad (4.4\text{-}7)$$

Now

$$\frac{\partial e_1}{\partial \theta_1} = 4a_1^{\frac{1}{2}}[\sin^2\theta_1 + 2h_1(1-\cos\theta_1)]^{\frac{1}{2}} \qquad (4.4\text{-}8)$$

$$\frac{\partial e_2}{\partial \theta_1} = -4a_2^{\frac{1}{2}}[\sin^2\theta_1 - 2h_2\cos\theta_1 + c]^{\frac{1}{2}} \qquad (4.4\text{-}9)$$

$$\frac{\partial e_1}{\partial c} = 0 \qquad (4.4\text{-}10)$$

$$\frac{\partial e_2}{\partial c} = 2a_2^{\frac{1}{2}} \int_{\theta_1}^{\pi} (\sin^2\theta - 2h_2\cos\theta + c)^{-\frac{1}{2}} \, d\theta - Y \qquad (4.4\text{-}11)$$

From eq.(4.2-6) the thickness of the inhomogeneity,

$$Y = 2a_2^{\frac{1}{2}} \int_{\theta_1}^{\pi} (\sin^2\theta - 2h_2\cos\theta + c)^{-\frac{1}{2}}\, d\theta \qquad (4.4\text{-}12)$$

Eq.(4.4-11) therefore reads:

$$\frac{\partial e_2}{\partial c} = 0 \qquad (4.4\text{-}13)$$

Substituting from eqs.(4.4-8) to (4.4-10) and (4.4-13) into (4.4-7),

$$\frac{1}{4}\frac{dE}{d\theta_1} = a_1^{\frac{1}{2}}K_1[\sin^2\theta_1 + 2h_1(1-\cos\theta_1)]^{\frac{1}{2}} - a_2^{\frac{1}{2}}K_2(\sin^2\theta_1 - 2h_2\cos\theta_1 + c)^{\frac{1}{2}} \qquad (4.4\text{-}14)$$

At the energy minimum, the variation of energy with θ_1 must be zero.

Therefore, using eq.(4.2-6),

$$A_1\left(\frac{d\theta}{dz}\right)_{\text{matrix}} = A_2\left(\frac{d\theta}{dz}\right)_{\text{inhomogeneity}}$$

at the boundaries, where $\theta = \theta_1$ or $2\pi - \theta_1$.

4.5 Condition for Wall Pinning

The wall can only remain pinned if an energy minimum exists in zero field after application of a forward field.

$$\text{i.e. } \frac{dE}{d\theta_1} = 0 \quad \text{when } H = 0$$

Then, from eq.(4.4-14)

$$(A_1K_1)^{\frac{1}{2}}\sin\theta_1 = (A_2K_2)^{\frac{1}{2}}(\sin^2\theta_1 + c)^{\frac{1}{2}}$$

Eq.(4.2-6) tells us that c must be greater than zero if $\frac{d\theta}{dz}$ is real when $\theta=\pi$.

Thus the condition for pinning to take place is

$$A_2K_2 < A_1K_1$$

i.e. The zero field wall energy within the inhomogeneity must be lower than that within the matrix if we can have pinning.

This condition is obeyed for $SmCo_5$ with Sm_2Co_{17} inhomogeneities and thus the model can be applied to this particular case.

4.6 Procedure for Calculation of Coercive Field

Eq.(4.4-12) is converted to an incomplete elliptic integral of the first kind using a technique given by Forlani and Minnaja (1969). θ_1 can be obtained from the inverse of this elliptic integral using a series expansion (Gradshteyn and Ryzhik 1965). Details of this calculation may be found in the appendix. Keeping thickness and field fixed, a range of values of θ_1 is calculated by varying c. Then, substituting into eq.(4.4-14), the variation of $\frac{dE}{d\theta_1}$ with θ_1 is obtained. A curve with a single maximum is observed as shown in figure 4.6-1a.

This corresponds to the energy having a maximum and minimum value with the energy barrier being the height difference between the two turning points (as in figure 4.6-1b). This is obtained by integrating the area below the $\frac{dE}{d\theta_1}$ vs.θ_1 curve.

As the reverse field is increased, the peak in the $\frac{dE}{d\theta_1}$ curve becomes shallower until finally it touches the θ_1 axis (figure 4.6-2a). This corresponds to the maximum and minimum of the energy curve approaching each other until finally they merge, giving a point of inflection (figure 4.6-2b). The energy barrier disappears and we are at the absolute zero coercive field, H_0.

As predicted by eq.(3.3-5) for a parabolic interaction force the graph of $E^{2/3}$ vs. H is linear with a negative slope, intercepting the abscissa at H_0 (see figure 4.15-3). Thus, from its slope and intercept H_0, b and F can be calculated.

The calculation is repeated at different thicknesses and also with variation in temperature which affects the values of I, K and A. The variation of coercive field with temperature and inhomogeneity thickness is thus observed.

4.7 The Constants of the Material

I and K for $SmCo_5$ were given by Benz and Martin (1972), while the values for Sm_2Co_{17} were taken from a paper by Deryagin, Kudrevatykh and Bashkov (1974).

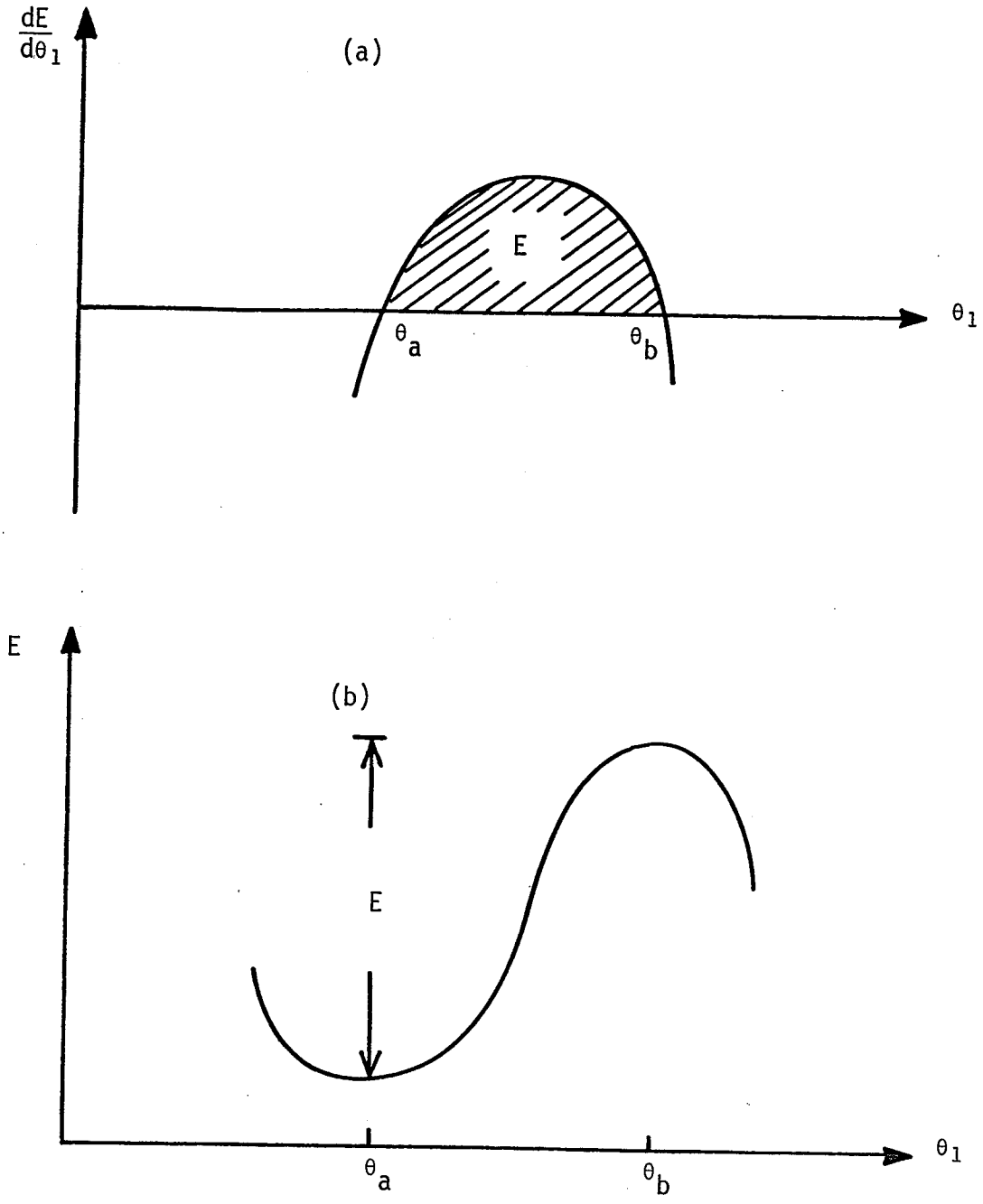

Figure 4.6-1 - (a) $\frac{dE}{d\theta_1}$ and (b) E vs. θ_1 when $H < H_0$.

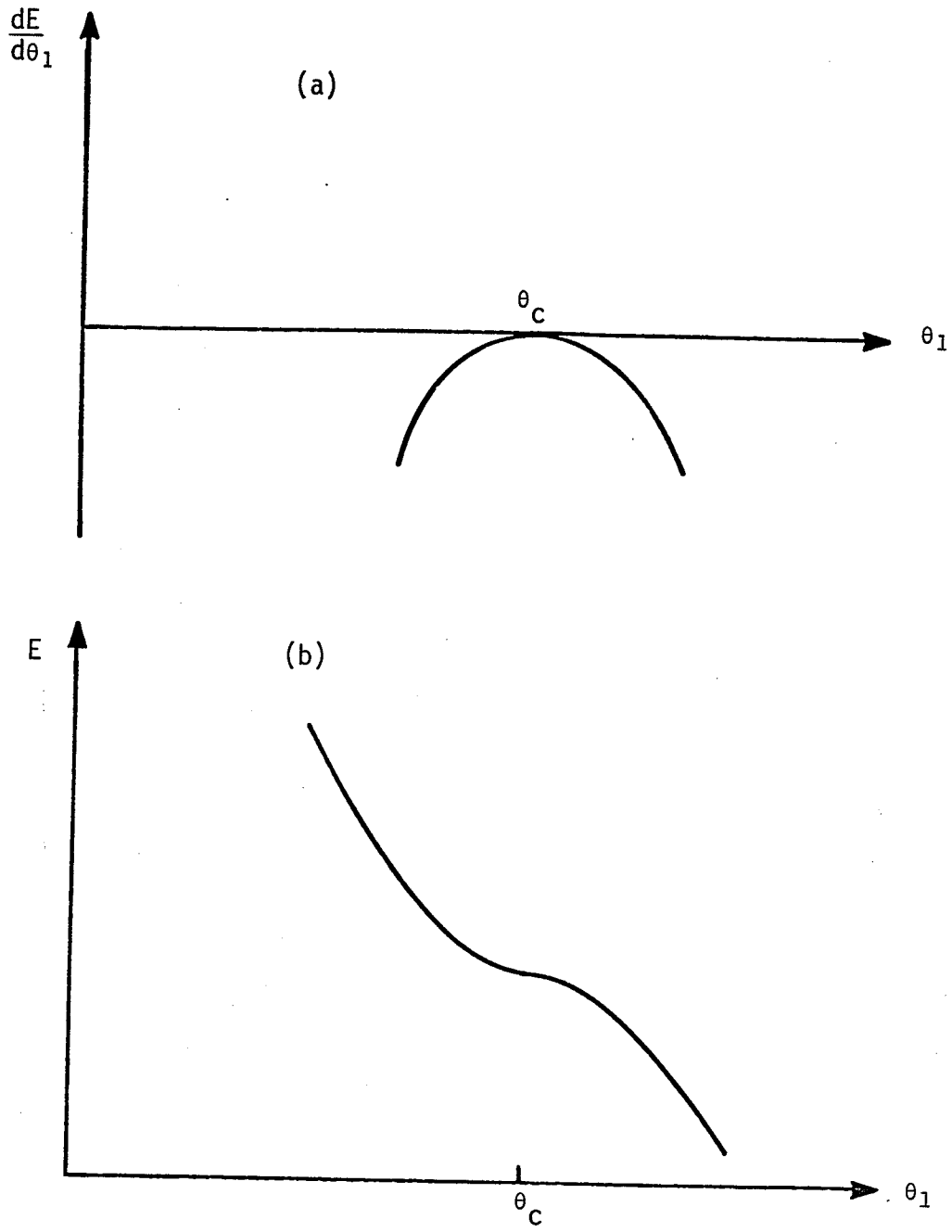

Figure 4.6-2 - (a) $\frac{dE}{d\theta_1}$ and (b) E vs. θ_1 when $H = H_0$.

The exchange constant A was calculated using an expression derived by Stoner and Wohlfarth (1948) and subsequently modified by Benz and Martin (1972) to read:

$$A = \frac{1}{8} \frac{kT_c}{r} \left(\frac{I}{I_0}\right)^2$$

where T_c is the Curie temperature of the material, given by Taylor (1971), r is the atomic radius, which is defined as the cube root of the average atomic volume and k is Boltzmann's constant.

Temperature variation appears in the $\left(\frac{I}{I_0}\right)^2$ term, where I_0 is the spontaneous magnetization at absolute zero. In practice, the value of I at 4.2K was used instead of I_0.

4.8 Calculation of Coercivity without Thermal Activation

Inhomogeneity thickness is the only independently chosen parameter in the calculation described in section 4.6. The coercive fields in the absence of thermal activation, H_0 were calculated for different thicknesses at temperatures ranging from 4.2K to 500K. The results for 75Å Sm_2Co_{17} and Co inhomogeneities have been plotted in figure 4.8-1.

The difference in coercivity, particularly at low temperatures, is immediately obvious, with the Co inhomogeneity causing a much larger coercive field. The values obtained with Co are greater than the coercivities measured by Benz and Martin (1972), while those obtained with Sm_2Co_{17} provide fairly good agreement. The improbability of

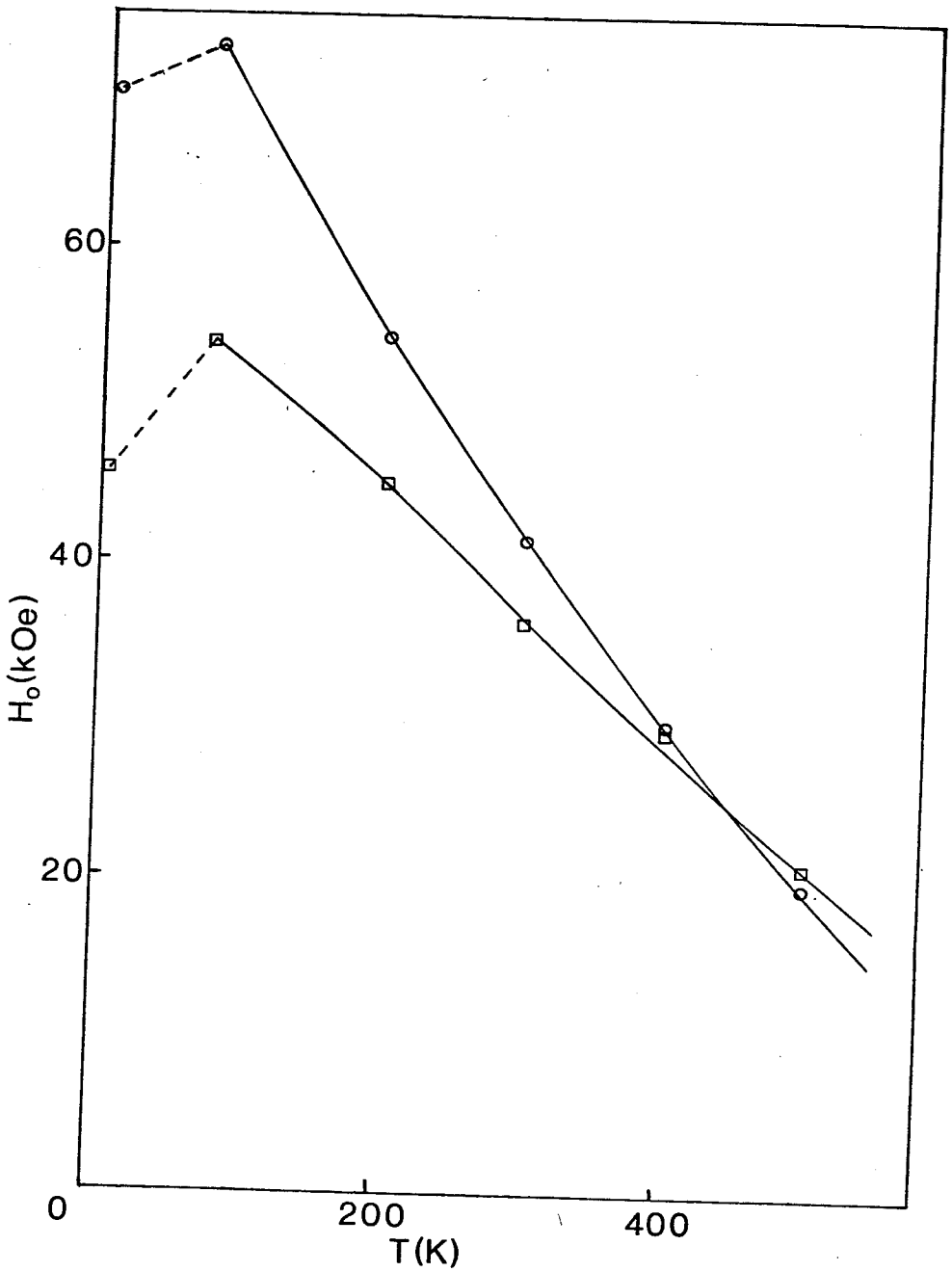

Figure 4.8-1 - Graph of absolute zero coercivity vs. temperature for 75A Co (circles) and Sm_2Co_{17} (squares) inhomogeneities.

unalloyed Co existing within the $SmCo_5$ matrix is therefore given further support.

4.9 Variation of H_0 with Obstacle Thickness

The curve of calculated coercive field against obstacle thickness at 77K is displayed in figure 4.9-1. This graph is typical of those seen for all temperatures. Initially coercivity increases steeply with thickness, but then levels off. Extrapolating back, this curve gives a finite thickness at which coercivity may be expected to disappear. At this 'cut-off thickness' the inhomogeneity is too small to be 'seen' by the wall. According to the graph, at 77K the cut-off thickness is 17Å.

This minimum thickness can also be calculated analytically by locating the thickness at which there was no activation energy required for escape in the absence of the field. The following expression for minimum thickness, Y_0, was derived.

$$Y_0 = 2\left(\frac{A_2}{K_2}\right)^{\frac{1}{2}}\left\{\ell n\left[\frac{1}{\varepsilon_0}+\left(1+\frac{1}{\varepsilon_0 2}\right)^{\frac{1}{2}}\right]\right\}$$

where

$$\varepsilon_0 = \left(\frac{A_1 K_1}{A_2 K_2} - 1\right)^{\frac{1}{2}}$$

Using this expression, minimum thicknesses have been calculated for Sm_2Co_{17} inhomogeneities in a $SmCo_5$ matrix. The results have been tabulated in 4.9-1.

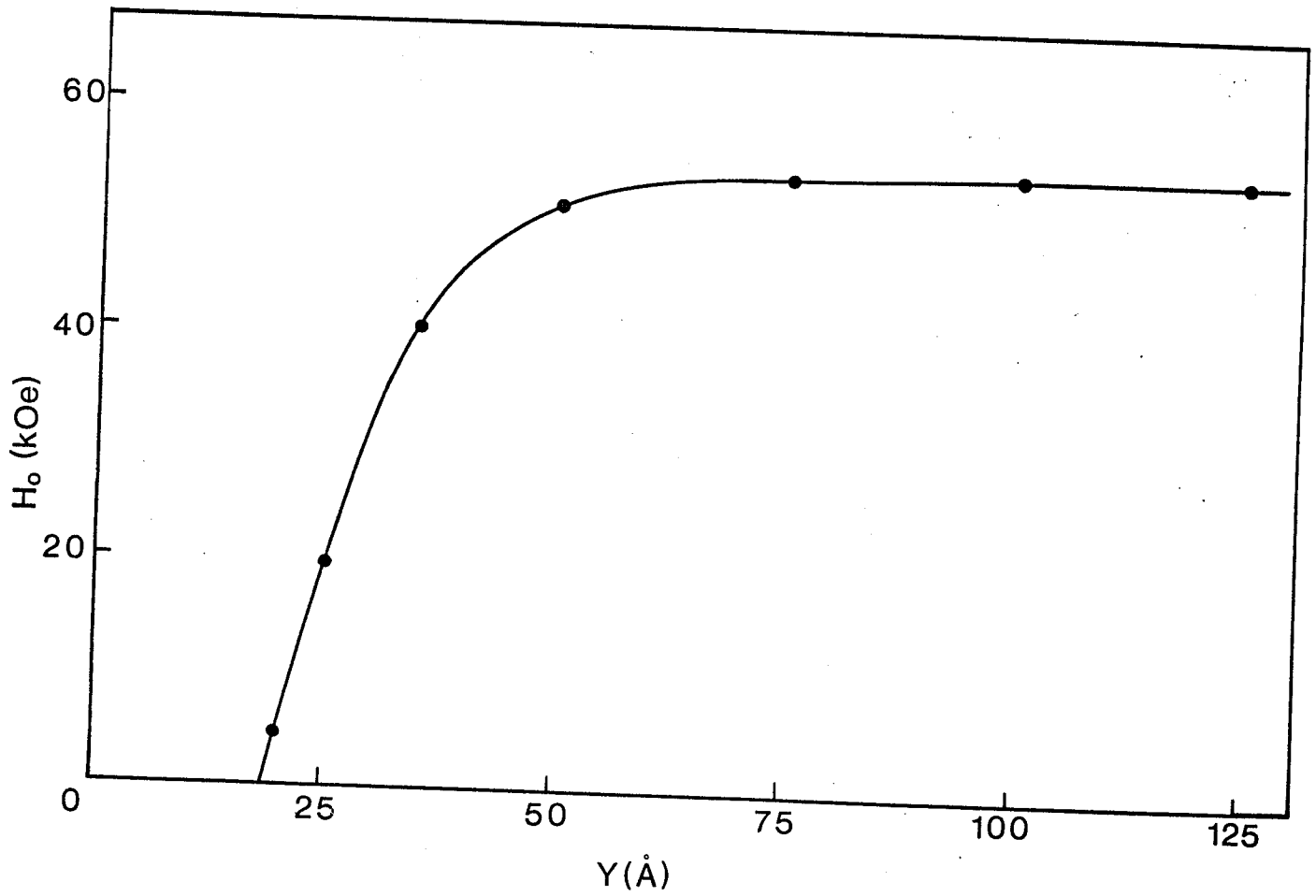

Figure 4.9-1 - Theoretical absolute zero coercivity plotted against inhomogeneity thickness at 77K.

Table 4.9-1

Dependence of Critical Thickness on Temperature for a Sm_2Co_{17} Inhomogeneity

T(K)	Y_0(Å)
4.2	18.2
77	17.0
200	18.7
300	20.7
400	22.6
500	26.4

The calculated dependence of coercivity upon inhomogeneity thickness may be explained by considering the forces which act upon the two 180° walls which make up the 360° domain wall.

There is, firstly, a repulsive force acting between winding walls. The magnitude of this force decreases as the separation between the walls increases.

The energy of the domain wall when it is within the inhomogeneity is lower than when it is in the matrix. This results in a force which attempts to keep each wall within the inhomogeneity and thus may be regarded as an attractive force.

For unpinning to take place, the field must be applied so as to augment the repulsive force. The coercive field is that field at which the net repulsive forces are just balanced by the attractive force.

Consider then the behaviour of the coercive field as inhomogeneity thickness increases from zero. Initially the two 180° walls are very close together and the ensuing repulsive force is larger than the constant attractive force. The wall cannot therefore be trapped and the coercivity will be zero and remain so until the thickness grows to the point where the repulsion between the walls is just balanced by the attractive force. This is the 'cut-off thickness'. From this point on the coercivity increases with thickness, as the wall-wall repulsion decreases. However, the rate of decrease will decline as thickness grows and so, consequently, will the rate of increase of coercivity, until at very large thicknesses the coercive field will reach a plateau where the entire 360° wall is confined in the inhomogeneity or has escaped into the matrix.

4.10 Variation of Spin Angle with Thickness

At the absolute zero coercive field, the spin angle at the matrix-inhomogeneity interface takes a value θ_1' which varies with obstacle thickness. This variation, once again at 77K, is displayed in figure 4.10-1. θ_1' increases as thickness decreases, reaching π at the cut-off thickness. The variation of spin within the domain wall at the critical thickness is sketched in figure 4.10-2.

4.11 Calculation of the Interaction Parameter, b

As stated in section 4.6, the interaction parameter is derived from the graph of (activation energy)$^{2/3}$ vs. magnetic field, an example of which is shown in figure 4.15-3.

The slope of that graph,

$$S = \frac{(\frac{4}{3} Fb)^{2/3}}{H_0}$$

$$= \frac{-(\frac{8}{3} Ib)^{2/3}}{H_0^{1/3}}$$

H_0, which is the intercept of the abscissa is easily obtained.

Thus,

$$b = \frac{\frac{3}{8}(-S^3 H_0)^{1/2}}{I} \qquad (4.11\text{-}1)$$

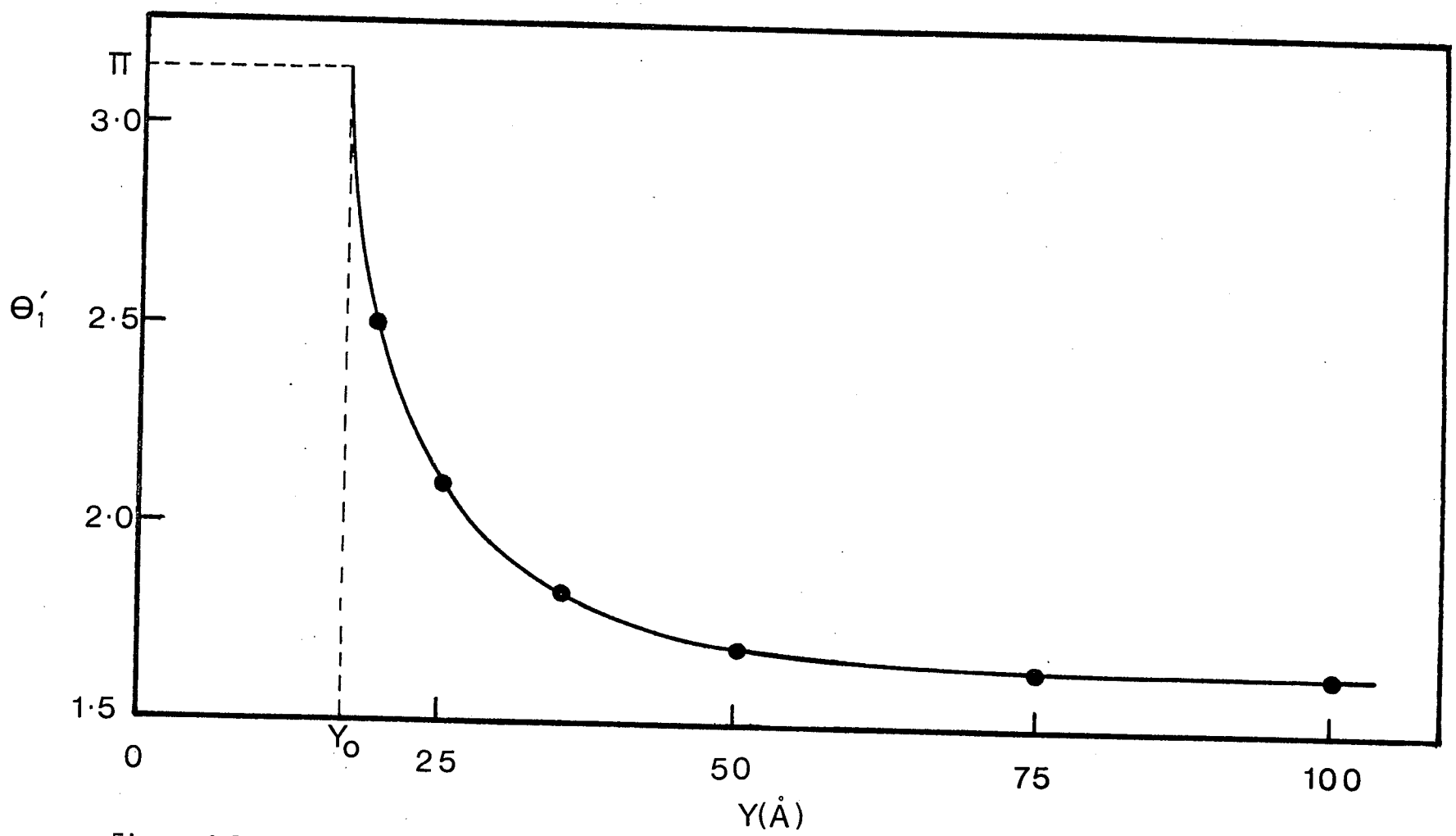

Figure 4.10-1 - Variation of the spin angle at the matrix-inhomogeneity boundary with inhomogeneity thickness at the coercive field (77K).

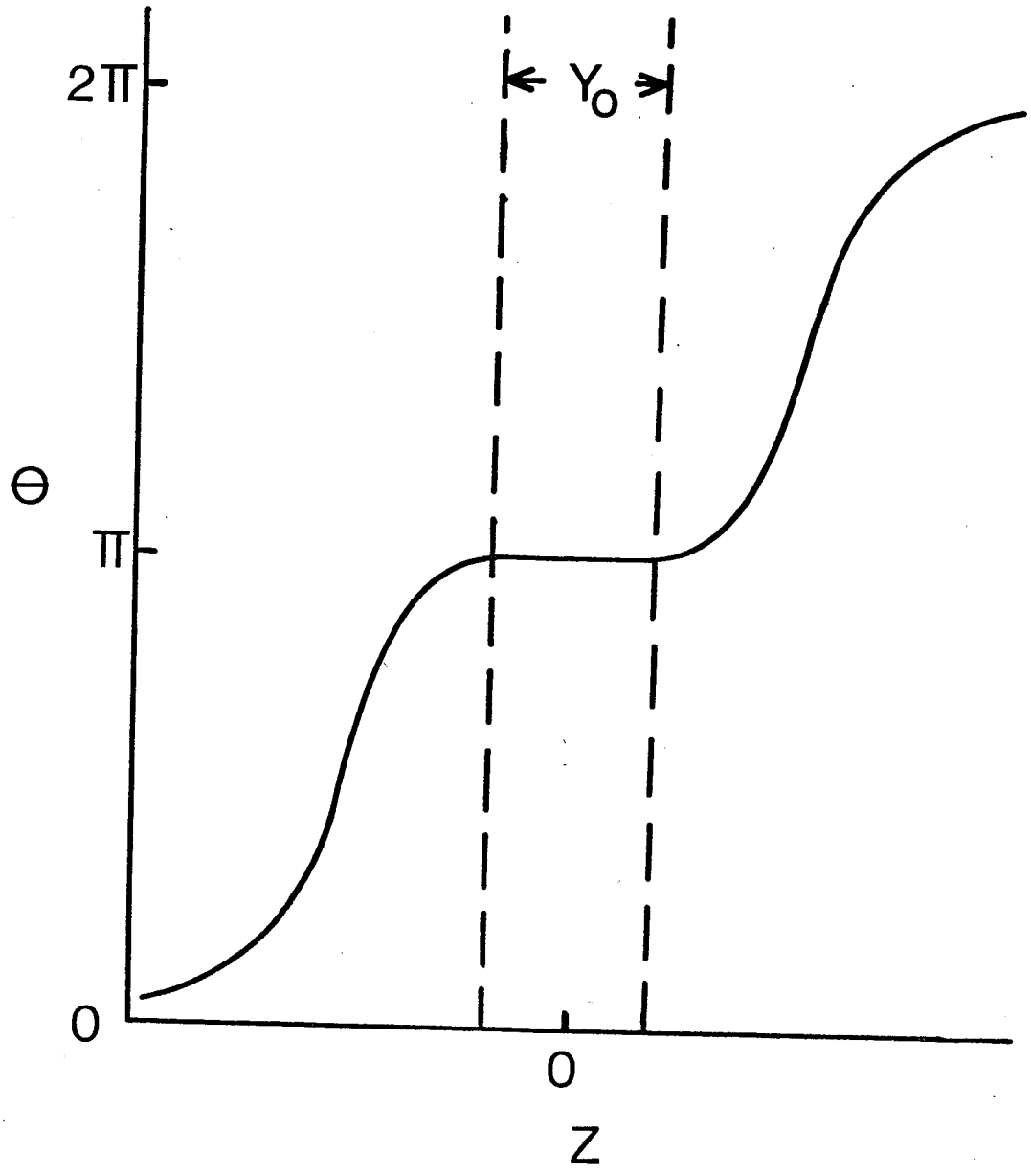

Figure 4.10-2 - The variation of spin angle in a 360° wall with position at the critical inhomogeneity thickness.

The variation of b with obstacle thickness and temperature is shown in table 4.11-1. It can be seen that as thickness increases, b becomes more sensitive to temperature variation. Even more pronounced is the dependence of b on H_0, shown in figure 4.11-1 for a temperature of 77K. (H_0 has been varied by changing the inhomogeneity thickness). b decreases with field, approaching the inter-atomic spacing as H_0 tends to zero.

4.12 Calculation of Wall Energy, γ, for the Pinned 360° Wall

The total energy per unit area is given by the energy outside the obstacle,

$$E_1 = 4(A_1K_1)^{\frac{1}{2}}\int_0^{\theta_1}[\sin^2\theta + 2h_2(1-\cos\theta)]^{\frac{1}{2}}\,d\theta \qquad (4.4\text{-}5)$$

plus the energy within the obstacle,

$$E_2 = 4(A_2K_2)^{\frac{1}{2}}\int_{\theta_1}^{\pi}[\sin^2\theta - 2h_2\cos\theta + c]^{\frac{1}{2}}\,d\theta + 2\gamma K_2(h_2-\tfrac{1}{2}c) \qquad (4.4\text{-}6)$$

This total energy, E_t contains magnetostatic as well as magneto-crystalline terms. At the coercive field H_0, the interaction energy will disappear. The wall energy is therefore obtained by subtracting the magnetostatic contribution from the total energy when $H = H_0$

Thus,

$$\gamma = E_t(H_0) - H_0\left(\frac{\partial E_t}{\partial H}\right)_{H_0}$$

Table 4.11-1

Dependence of the Interaction Parameter (in Å) on Temperature and Inhomogeneity Thickness

Y (Å) \ T (K)	4.2	77	200	300	400	500
50	6.89	7.15	7.34	7.75	7.95	8.08
75	7.88	7.91	8.57	9.32	9.93	10.63
100	7.77	7.74	9.47	10.87	12.34	13.24

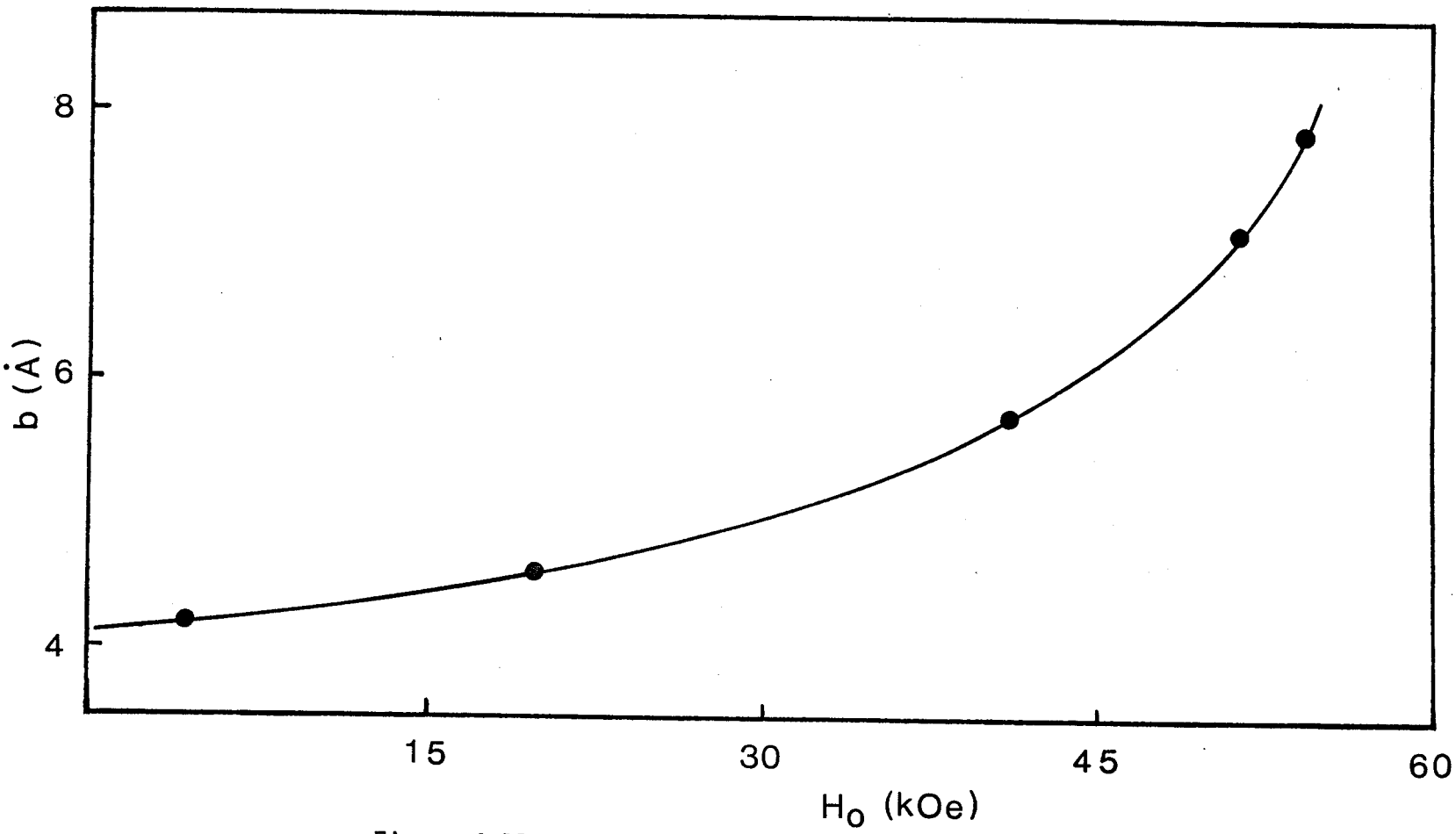

Figure 4.11-1 - Plot of interaction parameter vs. coercive field at 77K.

The energy of the portion of the wall outside the obstacle can be expressed analytically as:

$$\gamma_1 = 8(A_1K_1)^{\frac{1}{2}}[(h_{01}+1)^{\frac{1}{2}} - (h_{01}+\cos^2\tfrac{\theta_1'}{2})^{\frac{1}{2}}] \ ,$$

where h_{01} is the reduced coercive field, equal to $-\frac{I_1H_0}{2K_1}$

The wall energy inside the obstacle is:

$$\gamma_2 = 4(A_2K_2)^{\frac{1}{2}}\int_{\theta_1'}^{\pi}[(\sin^2\theta-2h_{02}\cos\theta + c)^{\frac{1}{2}} - h_{02}\cos\theta(\sin^2\theta-2h_{02}\cos + c)^{-\frac{1}{2}}]d\theta - K_2YC \ ,$$

where $h_{02} = -\frac{I_2H_0}{2K_2}$

and c takes the value at the point of inflection.

This latter contribution had to be computed numerically using the IMSL subroutine DCADRE with a relative error of less than 10^{-5} and with no absolute error.

The wall energy per unit area, $\gamma = \gamma_1 + \gamma_2$, is thus calculated.

Table 4.12-1 shows the variation of γ with obstacle thickness and temperature. While variation with thickness is relatively small, a strong dependence on temperature can be discerned. This is to be expected, because the anisotropy constants vary quite rapidly, particularly at higher temperatures and γ is more or less proportional to $K^{\frac{1}{2}}$, since A is slowly varying with temperature.

Table 4.12-1

Dependence of the Wall Energy (in erg/cm ^{2}) on Temperature and Inhomogeneity Thickness

T (K) / Y (Å)	4.2	77	200	300	400	500
50	81.6	81.1	68.7	60.1	50.5	42.0
75	80.6	80.0	67.1	57.8	48.0	39.3
100	84.2	84.3	67.2	57.3	48.5	38.7

4.13 Calculation of the Thermally Activated Coercive Field, H_c

The thermally activated coercive field, H_c is calculated using eq.(3.7-2) as

$$H_c = H_0(1 - \frac{25kT}{2\pi N\gamma b^2})$$

From section 3.6, N is 4.929, while b and γ have been calculated in sections 4.11 and 4.12 respectively.

H_c is therefore easily calculated and is shown along with H_0 in figure 4.13-1 for a Sm_2Co_{17} inhomogeneity of thickness 75Å.

4.14 Normalised Coercivity

It is evident from figures 4.9-1 and 4.13-1 that coercivity can vary with parameters such as inhomogeneity thickness that are not intrinsically dependent on the nature of the material. As such, a unique coercive field for a particular type of inhomogeneity at a given temperature does not exist and it is possible to have a variety of coercivity-temperature curves. Benz and Martin (1972) have, however, shown that all these curves reduce to a single curve when the coercivity is normalised to its value at 77K. This is therefore a facet of uniqueness against which the theoretical calculations of sections 4.8 and 4.13 can be compared.

Figure 4.14-1 shows the calculated normalised coercivities with and without thermal activation plotted against temperature for a

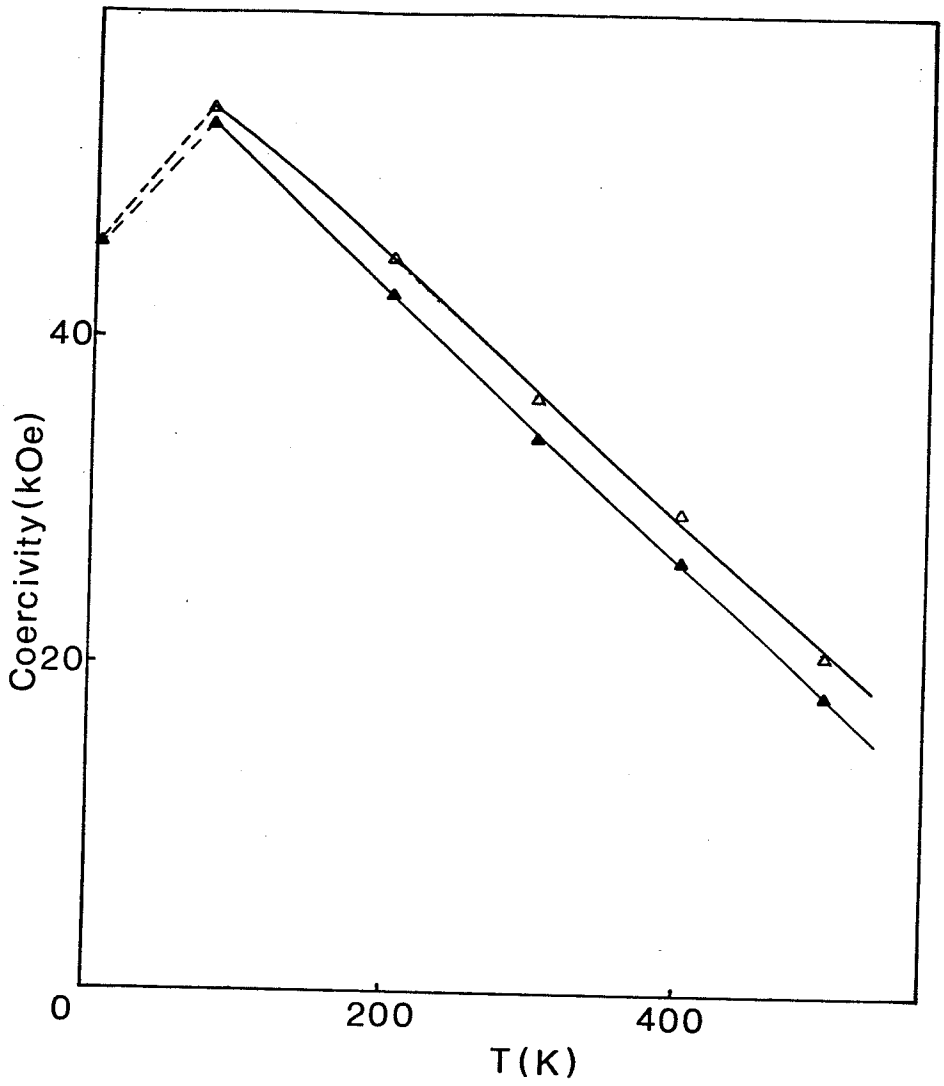

Figure 4.13-1 - Graphs of theoretical coercive fields with (filled symbols) and without (hollow symbols) thermal activation for a 75Å inhomogeneity.

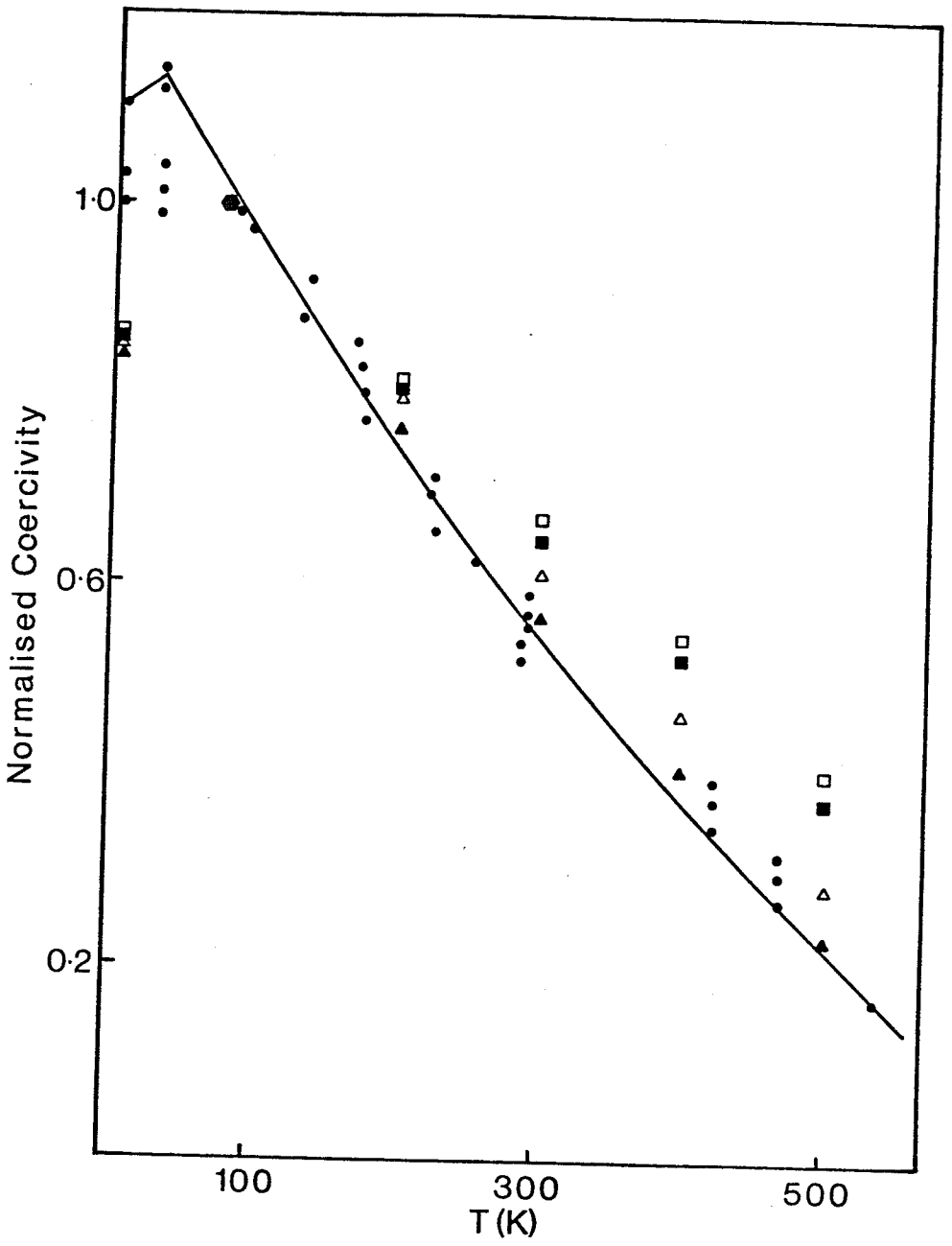

Figure 4.14-1 - Theoretical normalised coercivity with (filled symbols) and without (hollow symbols) thermal activation for 50A (triangles) and 100A (squares) inhomogeneities. The filled circles are experimental points of Benz and Martin (1972).

variety of thicknesses. The graph has been superimposed on the experimental data of Benz and Martin (1972). Agreement between the two sets of results is seen to be quite good, improving as thickness gets smaller.

4.15 Multiple Double Walls

To this point the trapping of a single double wall has been considered. The possibility exists however, that more than one double wall may be present in large grains. For these walls to be trapped, the inhomogeneity thickness must be sufficiently large. The variation of both activation energy, E and $\frac{dE}{d\theta}$ with spin angle θ for such a multiple wall case is illustrated in figures 4.15-1a and 4.15-1b. The coercive field of such a configuration is the lowest field at which the first pair of walls can escape from the trap.

It must be emphasized here that a large inhomogeneity thickness does not imply that two or more double walls must necessarily exist. Their presence depends on grain size, as well as upon the existence of sufficient energy to nucleate the walls when the grain was cooled below the Curie temperature. The inhomogeneity merely provides the environment for trapping the walls.

Coercivity in the presence of a second pair of walls is calculated as for the single double wall and its variation with obstacle thickness at 77K is displayed in figure 4.15-2, which also contains the variation for one double wall, which was previously shown in figure 4.9-1. It can

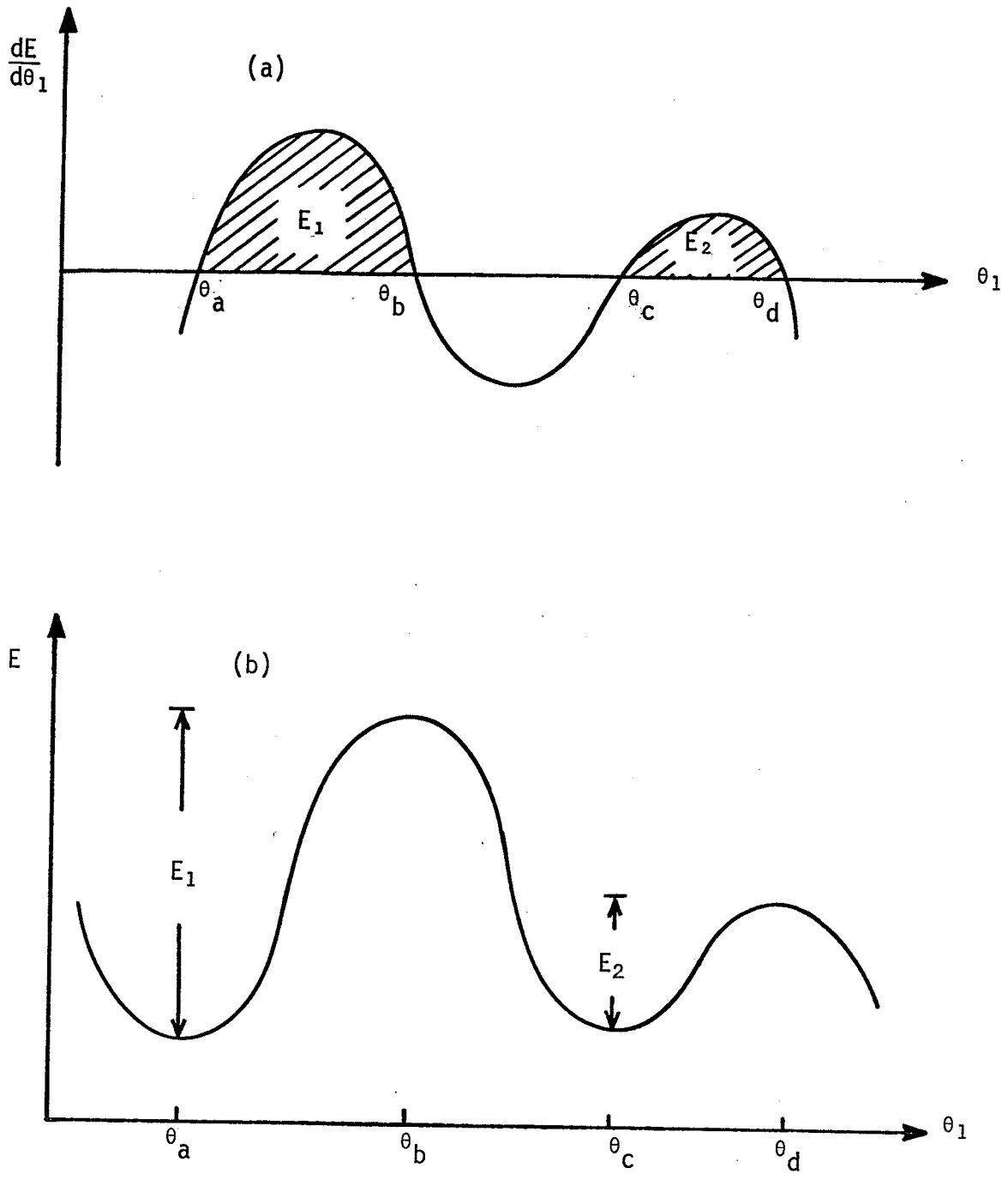

Figure 4.15-1 - (a) $\frac{dE}{d\theta_1}$ and (b) E vs. θ_1 for two double walls.

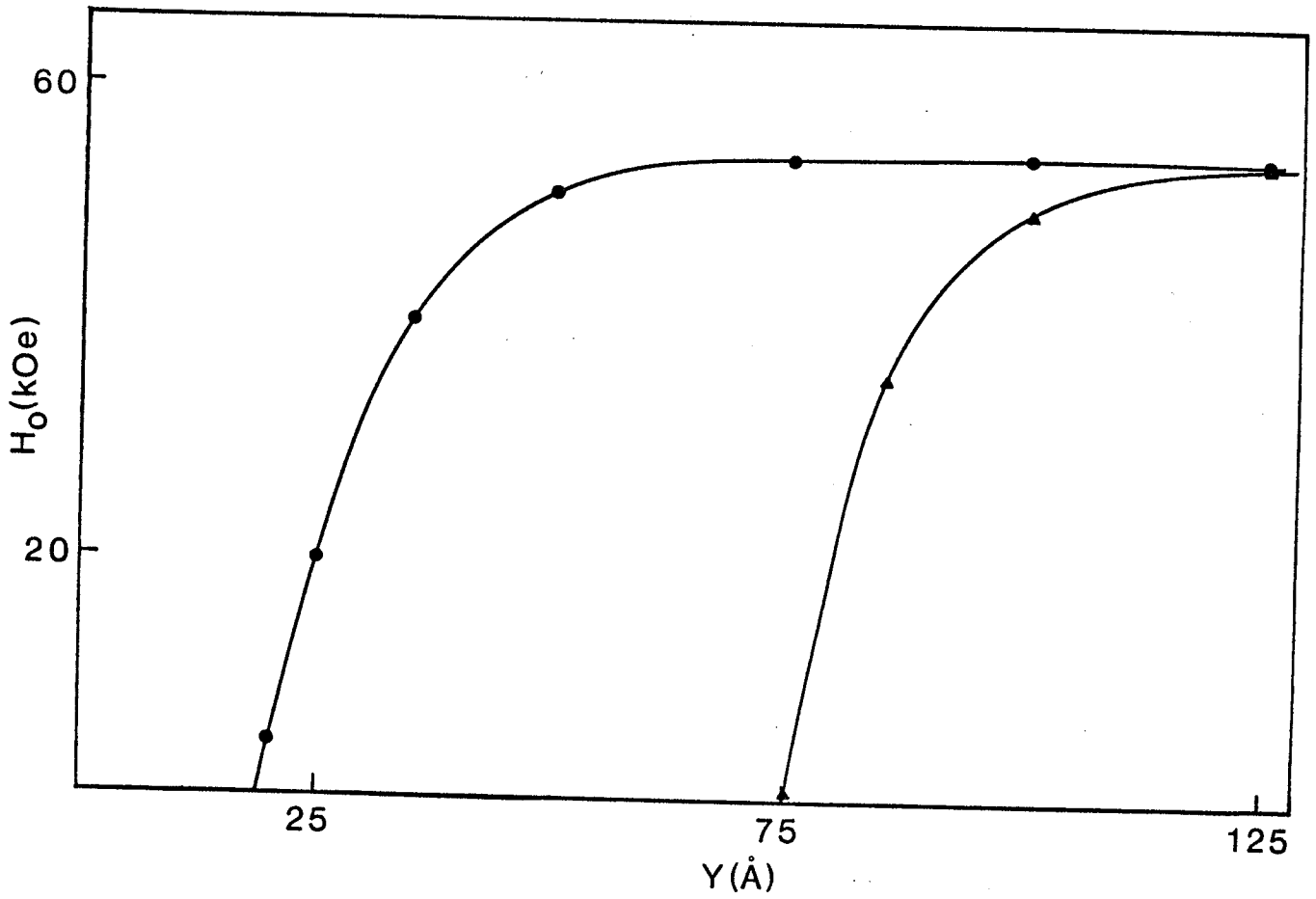

Figure 4.15-2 - Theoretical curve of absolute zero coercivity against inhomogeneity thickness for the first (circles) and second (triangles) double walls.

be seen that the coercive field for a given inhomogeneity thickness depends on the number of walls that are present within the grain and also that the coercivity of the second wall pair approaches that of the first when the inhomogeneity is sufficiently thick, dropping to zero at a larger critical thickness than for the single wall pair.

Figure 4.15-3 contains graphs of (activation energy)$^{2/3}$ versus magnetic field for the first and second pair of double walls trapped by a 125Å inhomogeneity at 77K. The coercivities are almost equal, as are the slopes of the graphs. Using eq.(4.11-1) therefore, it is plain that the two interaction parameters are very close to each other. Similar results were obtained in other situations when the coercive fields for the first and second double walls were equal, despite differences in inhomogeneity thickness, leading one to the conclusion that the interaction parameter is most directly tied to coercivity and not to inhomogeneity thickness, further bearing out the results of section 4.11.

4.16 Summary

The preceding calculations show that before a domain wall is trapped, a prescribed minimum inhomogeneity thickness is required. Coercivity steadily increases with this thickness before flattening out. If the inhomogeneity is sufficiently large however, more than one double wall may be trapped, leading to the possibility of reduced coercive fields. Experimental support for this finding comes from the observation

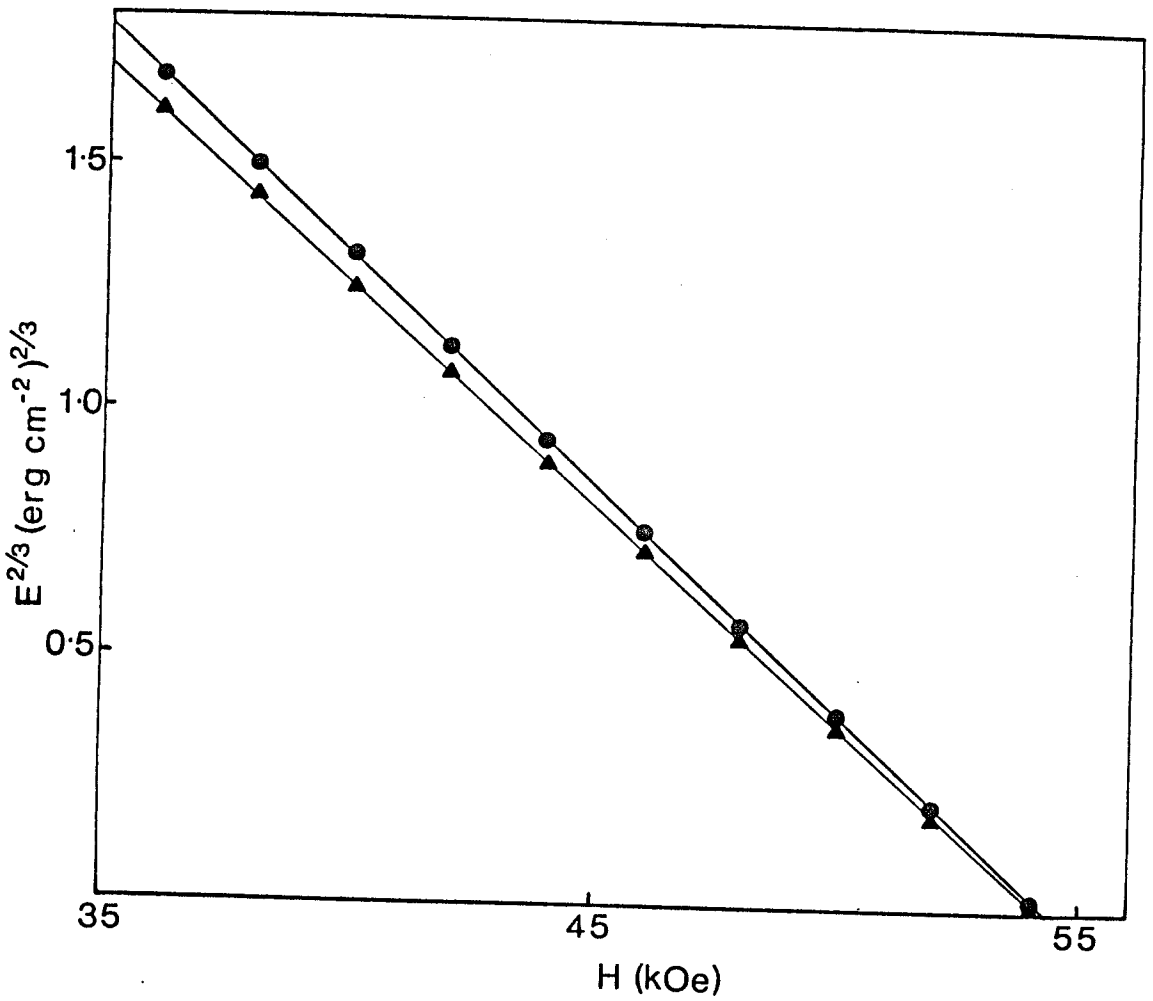

Figure 4.15-3 - (Activation energy)$^{2/3}$ plotted against field for the first (circles) and second (triangles) double walls for a 125A inhomogeneity at 77K.

of Barkhausen effect in chapter 8.

It has also been seen that the interaction parameter, b, varies monotonically with the coercive field, or conversely and perhaps more appropriately, that the coercive field increases as b increases.

Correlation between experimental and theoretical coercivities is quite good when an Sm_2Co_{17} inhomogeneity is chosen. Particularly convincing is the agreement between the two sets when the normalised coercivity is used. Co inhomogeneities yield coercive fields that are too large and therefore need not be considered.

It can be seen that the contribution to coercivity from thermal activation is relatively small. This calculation of coercivity therefore, while it may be said to verify the micromagnetic model of this chapter, cannot be regarded as adequately supportive of the interaction model of chapter 3. The validity of those concepts will be tested by the after-effect measurements of chapter 7.

It must be noted that conclusive experimental evidence for the existence of 360° winding walls can only come from Lorentz electron microscopy as Kerr microscopy does not offer the resolution required for the observation of the narrow 360° wall nuclei. Some evidence for a 360° wall has been observed (Riley and Jones 1973), but as the effective field seen by the specimen was near zero and as the positions and nature of obstacles, if any, were not clear, this cannot be regarded as being very convincing.

Until more supportive evidence is obtained, the concept of the 360° wall must be treated as an inferred hypothesis which leads to reasonably close agreement between theory and experiment.

CHAPTER 5

MICROSTRUCTURE AND COMPOSITION

5.1 The Magnetic Materials

Experimental measurements for this study were made on three different pieces of sintered $SmCo_5$. They were labelled B, C and M.

B was manufactured by the Hitachi Magnetics Corporation of Edmore, Michigan. It was a slightly curved bar with rectangular cross-section. B was obtained in an unmagnetized state and was therefore suitable for determination of demagnetizing factors and for investigation of the reversibility of magnetization.

C was also manufactured by Hitachi and was a rectangular block with square cross section. It had been previously magnetized.

M was manufactured by the General Electric Corporation of Schenectady, New York and was cylindrically shaped. It too had undergone prior exposure to a magnetic field.

The c-axes of the component crystallites appeared to have been well aligned in all three blocks, resulting in very clear indications of their easy directions.

B and C were provided by Professor C.W. Searle of this department. M was provided by Dr. D.L. Martin of the General Electric Corporation.

5.2 Experimental Procedure

Since experimental observations were made using magnet alloys that were obtained from external sources, it was essential to ensure

that the material was, in fact, $SmCo_5$. The following techniques were employed to verify this, as well as to identify some of the differences between the specimens.

X-ray diffraction was used to verify that the structure was hexagonal and had lattice parameters that were consistent with the accepted values for $SmCo_5$. By looking at the small variations in the lattice parameters, the precise composition of the alloy can be estimated (Martin, Benz and Rockwood 1972).

Transmission electron microscopy was used to confirm these results and also to investigate for any secondary phases or other inhomogeneities that may have been in the material.

Grain sizes were estimated by viewing the specimens in an optical microscope.

5.3 X-ray Diffraction

5.3.1 Specimen Preparation

Small pieces of magnet material were ground to a fine powder using a mortar and pestle and glued with Canada balsam onto a fine glass fibre. The fibre was aligned in a Debye-Scherrer powder camera so that while it rotated about the camera axis, it remained in the path of the filtered, collimated X-ray beam which was emitted by a cobalt tube with an anode current of 16mA at 40kV. The specimen was irradiated for 4 to 5 hours and the ensuing photographs were analysed.

5.3.2 Analysis

The photographs from all three specimens (B, C and M) were indexed for a hexagonal structure. All lines from all specimens fitted the expected pattern for $SmCo_5$, albeit with slight differences in their lattice parameters as shown in table 5.3.2-1. These lattice parameters are consistent in themselves with the previous work of Martin et al (1972) and making use of the results of their study, more exact estimates of the composition of the $SmCo_5$ matrix can be made. These have been included in table 5.3.2-1.

The $K\alpha_1$ and $K\alpha_2$ wavelengths produced sharp lines at the higher angle reflections, indicating a high degree of homogeneity within the $SmCo_5$ matrix. This contrasted with the broader lines that were observed with specimens which had been heated to the Curie temperature of 724°C. The broadening could have conceivably been the result of strain, induced by precipitation of a secondary phase. However, as previously, no extraneous lines that may have belonged to a secondary phase were observed.

The absence of reflections that did not belong to the $SmCo_5$ pattern does not mean that secondary phases are absent in the alloys. Unless they constitute over 5% of the material, it is unlikely that they would be readily detected by X-ray diffraction techniques.

Table 5.3.2-1

Measured Lattice Parameters and Corresponding Composition

Specimen	a (Å)	c (Å)	At.% of Sm	Composition
B	4.997	3.977	16.55	Co-rich
C	4.999	3.973	16.67	Near-Stoichiometric
M	5.001	3.968	16.80	Sm-rich

5.4 Electron Microscopy

5.4.1 Foil Preparation

A thin slice of $SmCo_5$ was cut from the bulk material with a diamond wheel. As the material was extremely brittle, the smallest thickness that could be obtained without crumbling was only 0.4 mm. From this slice, a 3 mm diameter disc was cut using a spark erosion machine. The disc was placed in a Struers Tenupol jet polisher and electropolished in a solution of 15% perchloric acid in acetic acid. The polishing potential was 14V. A photo-electric cell arrangement triggered an alarm when the foil became transparent. The foil was removed from the solution and washed in methyl alcohol and then in ethyl alcohol. It was examined in a Phillips EM300 electron microscope at 100kV. Despite the relatively large initial thickness of the foil, satisfactory specimens were obtained.

5.4.2 Analysis of Micrographs

Electron diffraction patterns were indexed by measuring the distance of diffraction spots from the central spot as well as the angles between spots. A chart was made of the expected distances that might be expected on the photograph for the various reflections of a hexagonal $SmCo_5$ lattice. Using this chart, the possible indices for

each diffraction spot were obtained. The angles between spots were then checked against a stereographic projection which had been constructed using the lattice parameters of $SmCo_5$. In this manner a consistent indexing scheme was determined for each diffraction pattern.

All micrographs were readily indexable for $SmCo_5$ as expected. A typical diffraction pattern is shown in figure 5.4.2-1.

However, as typified by figure 5.4.2-2, a few micrographs also had secondary diffraction patterns. These were not, as initially suspected, caused by the presence of a secondary Sm-Co phase, but were rather the result of slightly misoriented ($\sim 10^{\circ}$) particles within the sintered material. The dark field image of a spot belonging to such a pattern is shown in figure 5.4.2-3. The misoriented particles are clearly visible. (The c-axes of this region and the bulk material are parallel for this case).

Figure 5.4.2-2 also displays a series of four diffraction rings; three of which are readily identifiable as belonging to the oxide, Sm_2O_3. Also, additional diffraction spots which do not belong to the $SmCo_5$ diffraction pattern can be seen along the (001) direction. These spots are not indexable for any of the Sm-Co phases. However, examination of the diffraction pattern indicated that they were caused by a compound which had grown coherently, parallel to the basal plane of the $SmCo_5$ matrix. It is possible that this contamination could have occurred during the polishing stage.

Figure 5.4.2-1 - An Electron Diffraction Pattern from $SmCo_5$

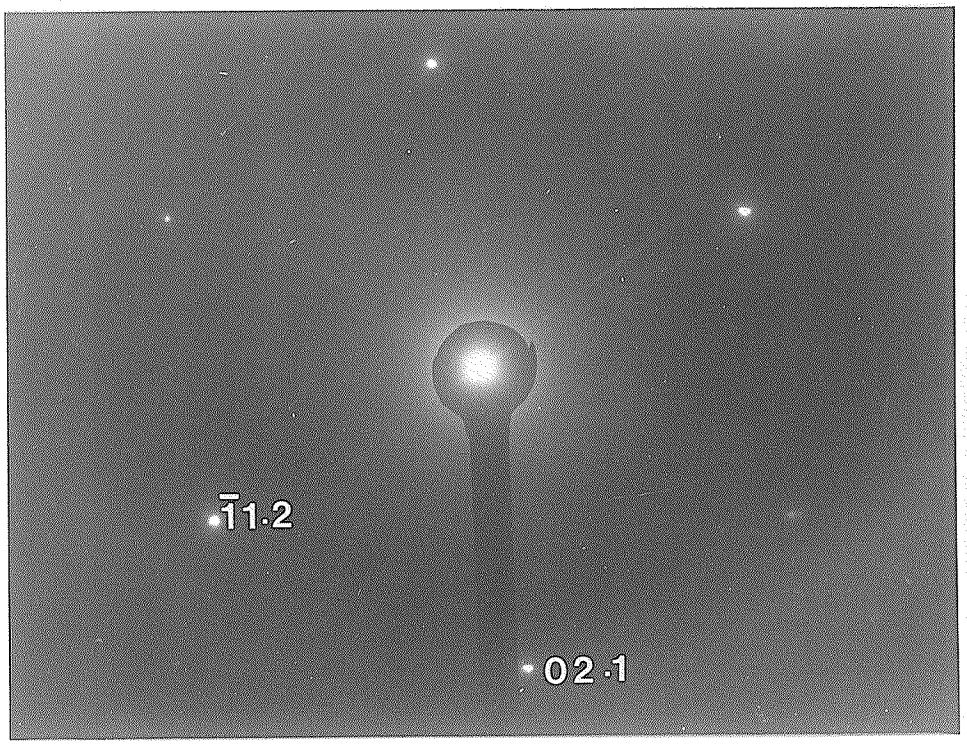
$\bar{1}1.2$
02.1

Figure 5.4.2-2 - An Electron Diffraction Pattern from a $SmCo_5$ specimen. The 00.1 reflection is common to all the patterns. The other three marked reflections belong to different patterns.

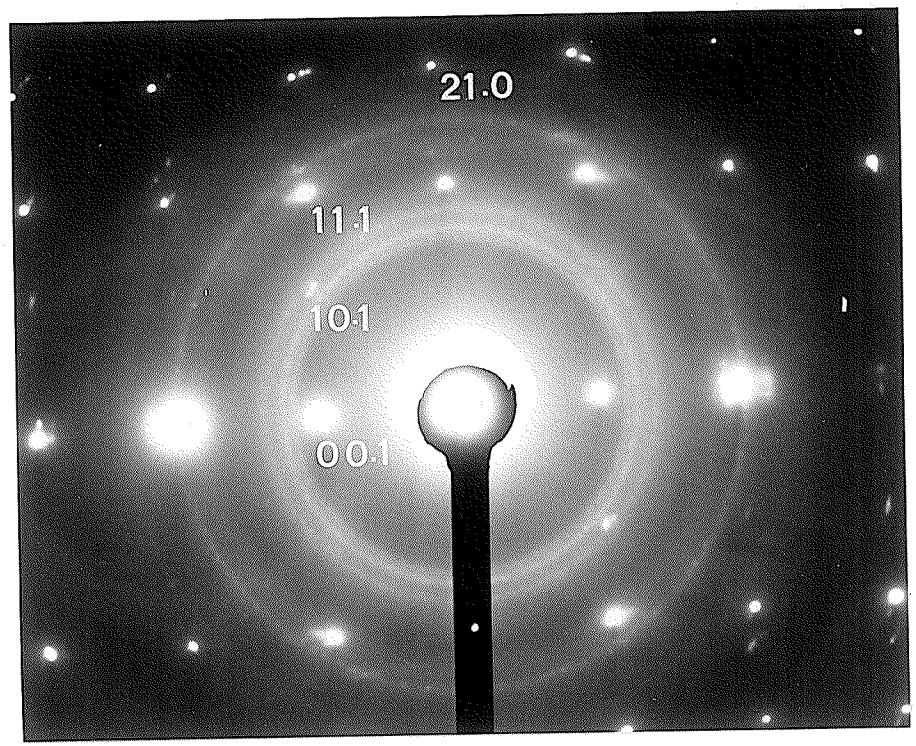
21.0
11.1
10.1
00.1

Figure 5.4.2-3 - Dark field image, magnified 72000 times, of the 11.1 reflection in figure 5.4.2-2.

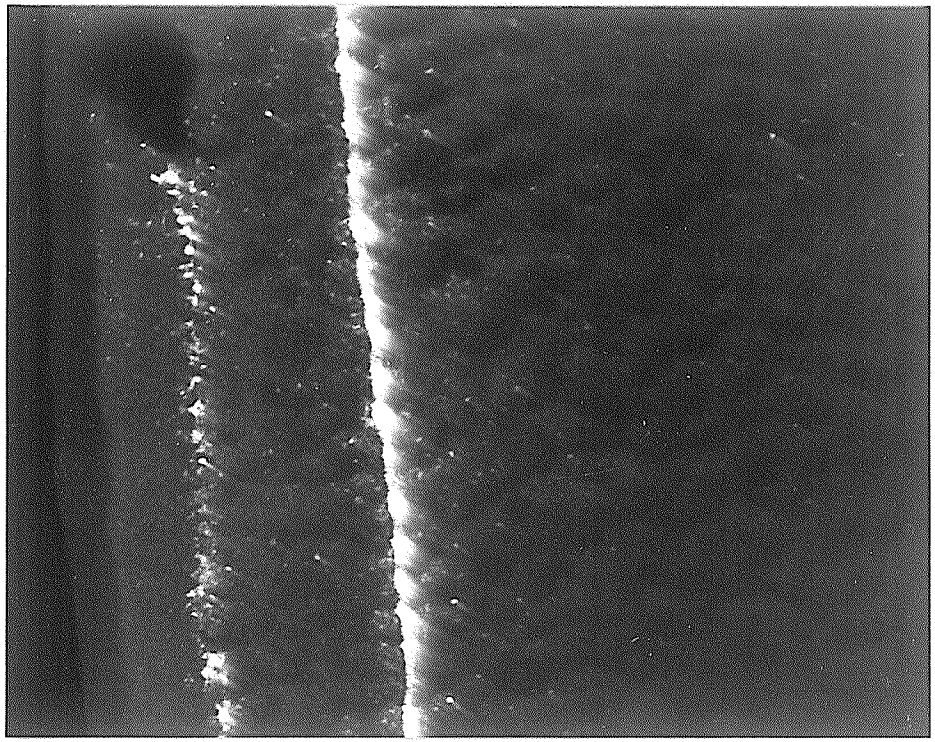

A feature of all the bright field micrographs was that grain boundaries were not observed. This implied, that the micrograph foils were being preferentially polished in the centre of the grain because grain boundaries were proving resistant to the polishing solution being used. This was confirmed when a specimen which had been prepared for the electron microscope was examined under an optical microscope. The 'hole' was positioned entirely within a grain. Furthermore it was necessary to raise the objective lens to focus on the grain boundaries, showing their preferential resistance to erosion.

All this would seem to indicate that the grain boundaries had a different composition from the grain itself. A previous electron microscope study by Fidler, Kirchmayr and Wernisch (1979) has revealed the presence of Sm_2Co_{17} precipitates in $SmCo_5$ alloys. As discussed in chapter 2, the sintering procedure makes the presence of secondary Sm-Co phases within the $SmCo_5$ matrix almost unavoidable. It is therefore very likely that the grain boundaries are composed of such a secondary phase.

5.5 Grain Size Determination

Grain structure was easily observed by viewing a cut face of the specimen in a Leitz Wetzlar optical microscope. The dimensions of grains were determined, using a calibrated eyepiece scale. A large number of measurements were made on each material and the resulting maximum,

minimum and average grain sizes are given in table 5.5-1.

B had a larger overall grain size than M or C which were similar in size.

5.6 Discussion

Using X-ray diffraction it has been confirmed that the material under examination is indeed $SmCo_5$.

The attempt to use electron microscopy to identify the nature of the secondary phase, the existence of which, paradoxically, the electropolishing seems to confirm, was unsuccessful. This will be discussed further in the final chapter. An interesting finding here was the presence of fairly sizeable misoriented regions of the $SmCo_5$ material itself. It is quite conceivable that such regions could act as pinning sites, because the angles between their easy directions and the magnetic field would be different from that in the properly oriented material. However, the rather small angle of misorientation suggests that such an effect would be of relatively minor proportions, though this could conceivably account for the small coercivities of $\sim$100 Oe observed in virgin samples (section 6.5.2).

The grain sizes were correlated with the measurements of the Barkhausen effect. This has been discussed more fully in chapter 8.

Table 5.5-1

Grain Dimension (in μ)

Specimen	Maximum	Minimum	Average
B	72	33	48 ± 14
C	50	28	38 ± 7
M	48	24	34 ± 9

CHAPTER 6

MAGNETIZATION MEASUREMENTS

6.1 Specimen Preparation

For most measurements of magnetization, the sintered $SmCo_5$ magnet material was cut into cubes of side ∿4 mm with a diamond wheel. For some of the demagnetizing factor experiments different sizes were used, so that different demagnetizing factors could be obtained. These pieces were placed in the apparatus shown in figure 6.1-1. The interior of the chamber was lined with a hardened paste of alumina powder and epoxy resin. When a continuous jet of pressurised air was passed into the chamber, the spinning specimen ricocheted around it. The specimen's corners and sharp edges were thus gradually ground away. In this manner ellipsoids were obtained. Interestingly, the most erosion appeared to be along the easy axis of the strongly anisotropic $SmCo_5$ crystallites. Typically, the largest dimension of the sample was 2.5 mm. The mass was ∿0.15g.

6.2 Extraction Method

When a magnetized specimen is placed in a sensing coil and then withdrawn, the resulting change in magnetic flux through the coil generates an electromotive force in the coil. This force, when measured, enables us to calculate the magnetization of the specimen, as shown below.

Suppose that the specimen has magnetization I. To simplify this

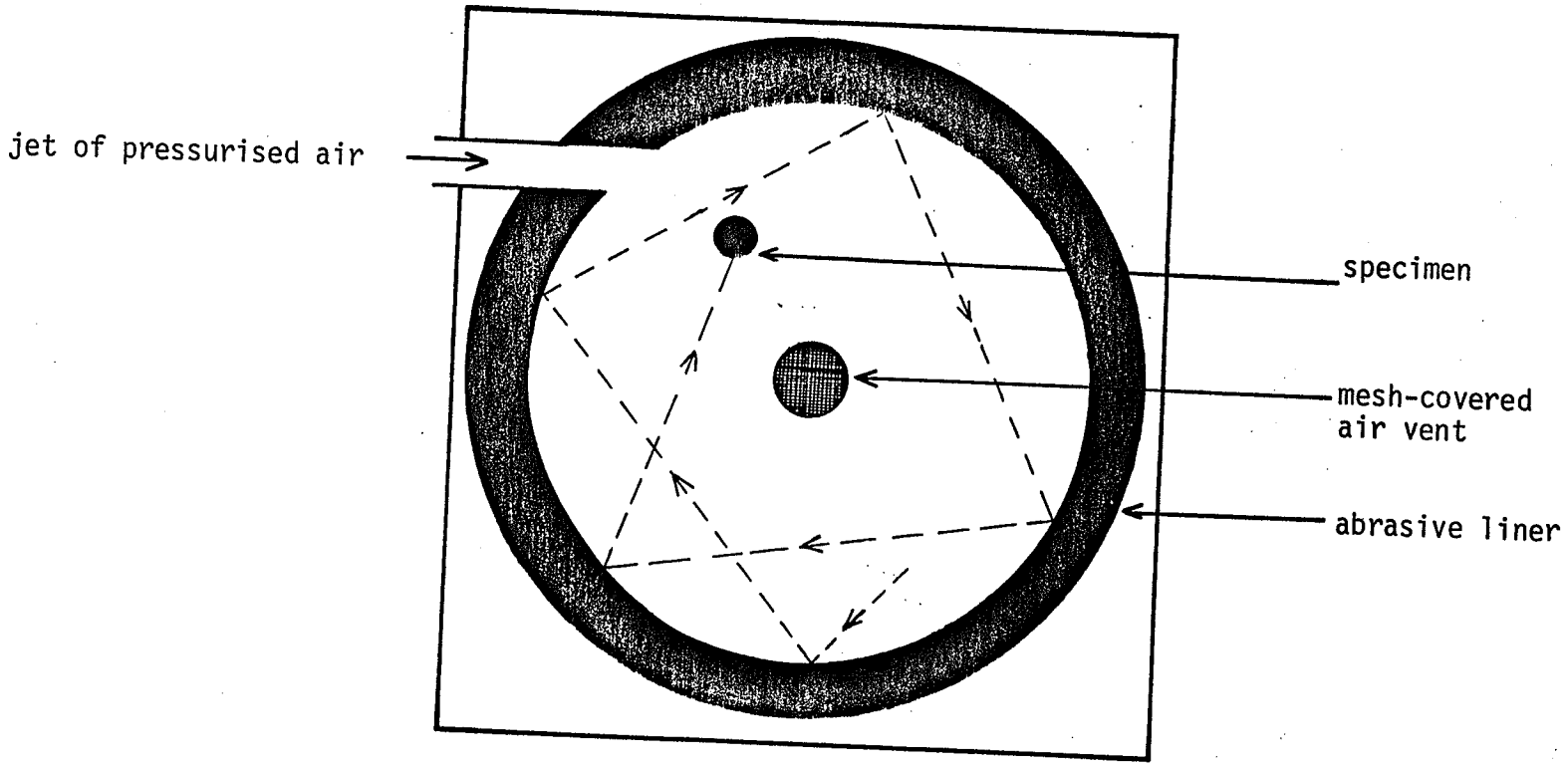

Figure 6.1-1 - Apparatus for grinding specimens

illustration, let the specimen have a cross-sectional area A, equal to that of the sensing coil.

Then, the flux through the coil,

$$\phi_1 = (H_i + 4\pi I)A \quad ,$$

where H_i is the internal field of the specimen and is given by,

$$H_i = H_a + H_D \quad ,$$

where H_a is the external field and H_D is the demagnetizing field of the specimen.

If D is the demagnetizing constant,

$$H_D = -DI$$

Therefore,

$$\phi_1 = [H_a + (-D + 4\pi)I]A$$

When the specimen is withdrawn from the coil, the flux through the coil is now given by

$$\phi_2 = H_a A$$

Therefore, the change in flux,

$$\Delta\phi = (D - 4\pi)AI$$

and

$$\Delta\phi \propto I$$

The e.m.f. generated in the coils due to a flux change,

$$\varepsilon_i \propto \frac{d\phi}{dt}$$

$$\Delta\phi = \int \frac{d\phi}{dt}\, dt$$

or

$$\Delta\phi \propto \int \varepsilon_i\, dt$$

and

$$I \propto \int \varepsilon_i\, dt$$

Thus, the integral with respect to time of the e.m.f. generated in the coils is directly proportional to the magnetization of the specimen.

6.3 Measurements in the Electromagnet

6.3.1 Electromagnet

A water-cooled Magnion electromagnet was used to obtain fields of magnitude up to 17kOe. The magnet was driven by a 25A regulated power supply. Polarity of the field could be reversed by reversing the coil current. A hole was bored in the pole faces along the axis of the core to facilitate insertion and removal of the specimen. The field was varied using a potentiometer in the power supply. The current passing through the magnet coils was measured. Calibration of the field was done against this current, using a flip coil flux meter.

6.3.2 Field Profile

The field should ideally be uniform in the entire volume occupied

by the specimen. In practice though, it will change in magnitude as one moves away from the precise centre of the pole face gap. This variation was observed using a small sensing coil. It was found that the fractional change in field in the longitudinal direction was given by,

$$\Delta h_l = -0.00126\ l^3 \quad ,$$

where l is in mm.

In the radial direction the fractional change was

$$\Delta h_r = 0.00121\ r^2 \quad ,$$

where r is in mm.

Therefore, the maximum fractional changes across the entire sample, taking l = r = 1.25 mm, are:

$$\Delta h_l(\text{max}) = -0.00246$$

and

$$\Delta h_r(\text{max}) = 0.00190 \quad ,$$

which are well within experimental error.

6.3.3 Measurement of Magnetization

A 15000 turn coil of B.S. 44 gauge copper wire was placed between the pole faces with axis along the field direction. This served as the pick up coil. When the sample was removed from the middle of the pole faces and the pick-up coil, the resulting change in flux generated an

e.m.f. in the pick-up coil circuit. This e.m.f. was integrated using an electronic integrator (figure 6.3.3-1) based on a chopper stabilized operational amplifier. The resulting output voltage was read on a digital voltmeter. As shown in section 6.2 this reading was directly proportional to the magnetization of the specimen.

6.3.4 Image Effect

Because the pole faces are made of permeable material, a magnetic image of the specimen was formed. This phenomenon is known as the image effect and must be corrected for, since it interacts with the specimen and increases the flux density around it (figure 6.3.4-1). The image effect is strongly field dependent and causes the apparent moment to decrease by as much as 8% at 17kOe.

The correction factor, L, was determined by using a small coil with a constant current flowing through it, so as to produce a constant magnetic moment. This coil was placed in the field and as the field increased, a decline in the output was observed. The ratio of apparent reduced moment at a particular field to real moment, when inverted, gives the image correction factor at that field. The variation of this factor with field is shown in figure 6.3.4-2.

6.3.5 Calibration of the Coil-Integrator System

The moment sensing system was calibrated using an annealed nickel

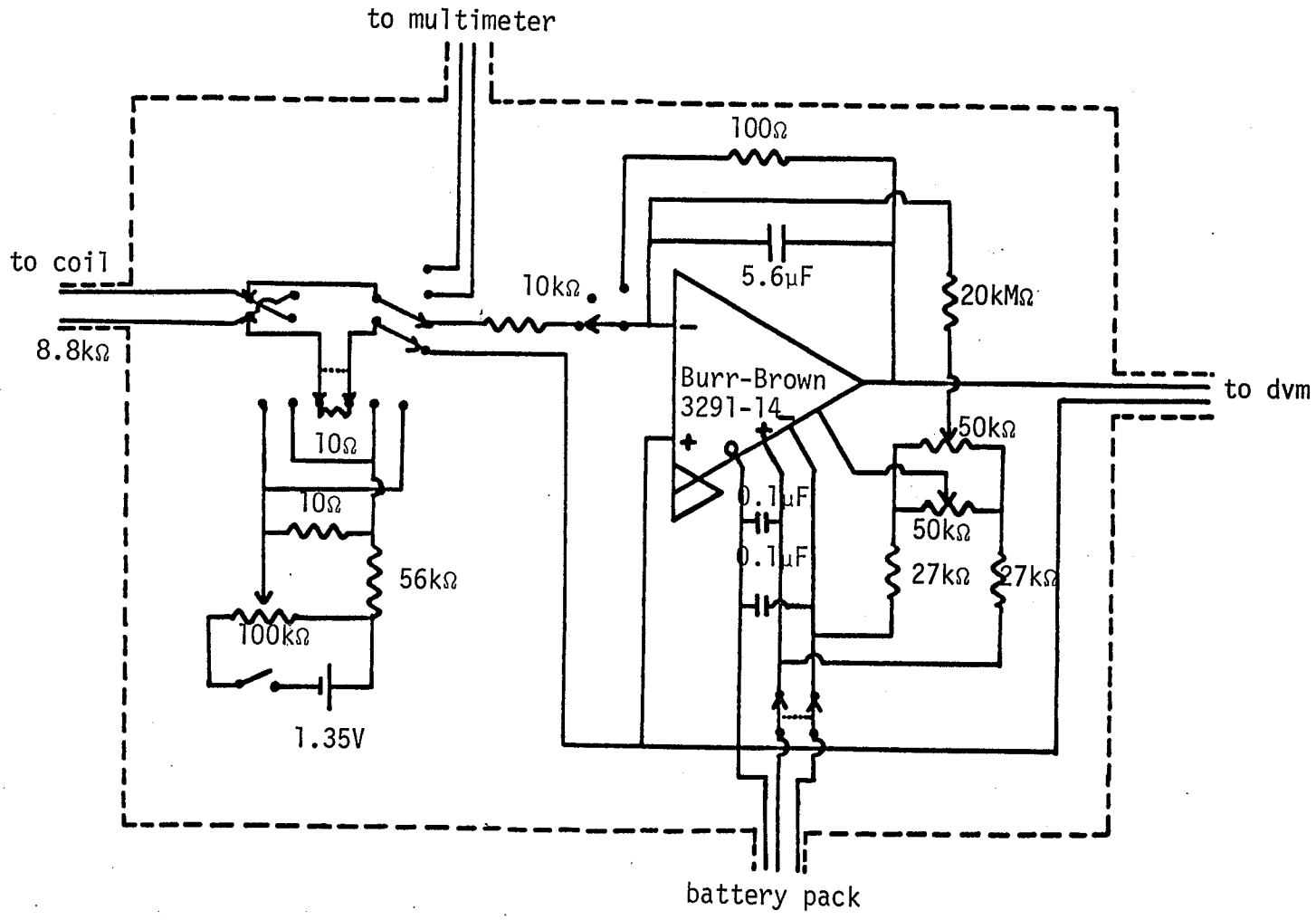

Figure 6.3.3-1 - Schematic diagram of the integrator.

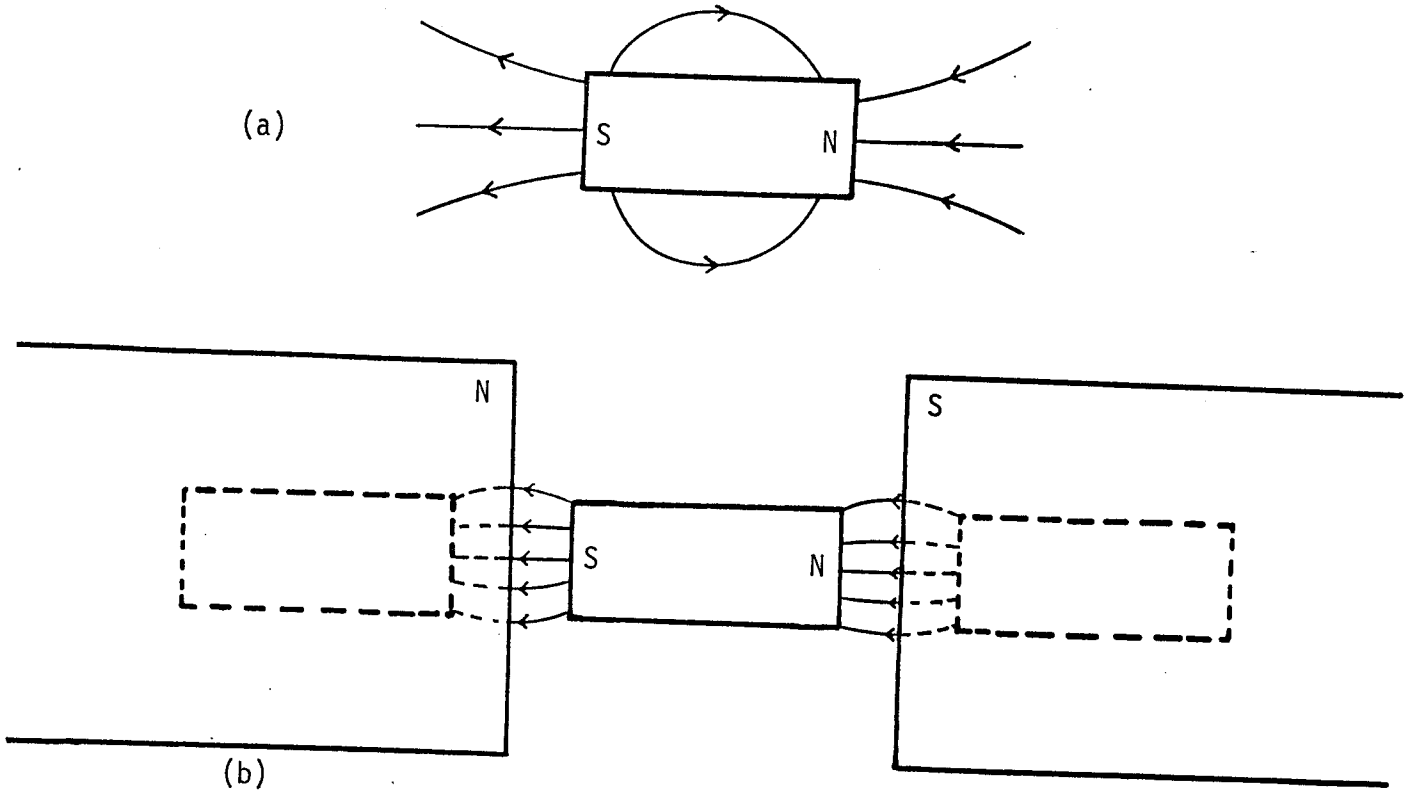

Figure 6.3.4-1 - (a) Magnetized specimen away from the poles.
(b) Image effect in the poles caused by the magnetized specimen.

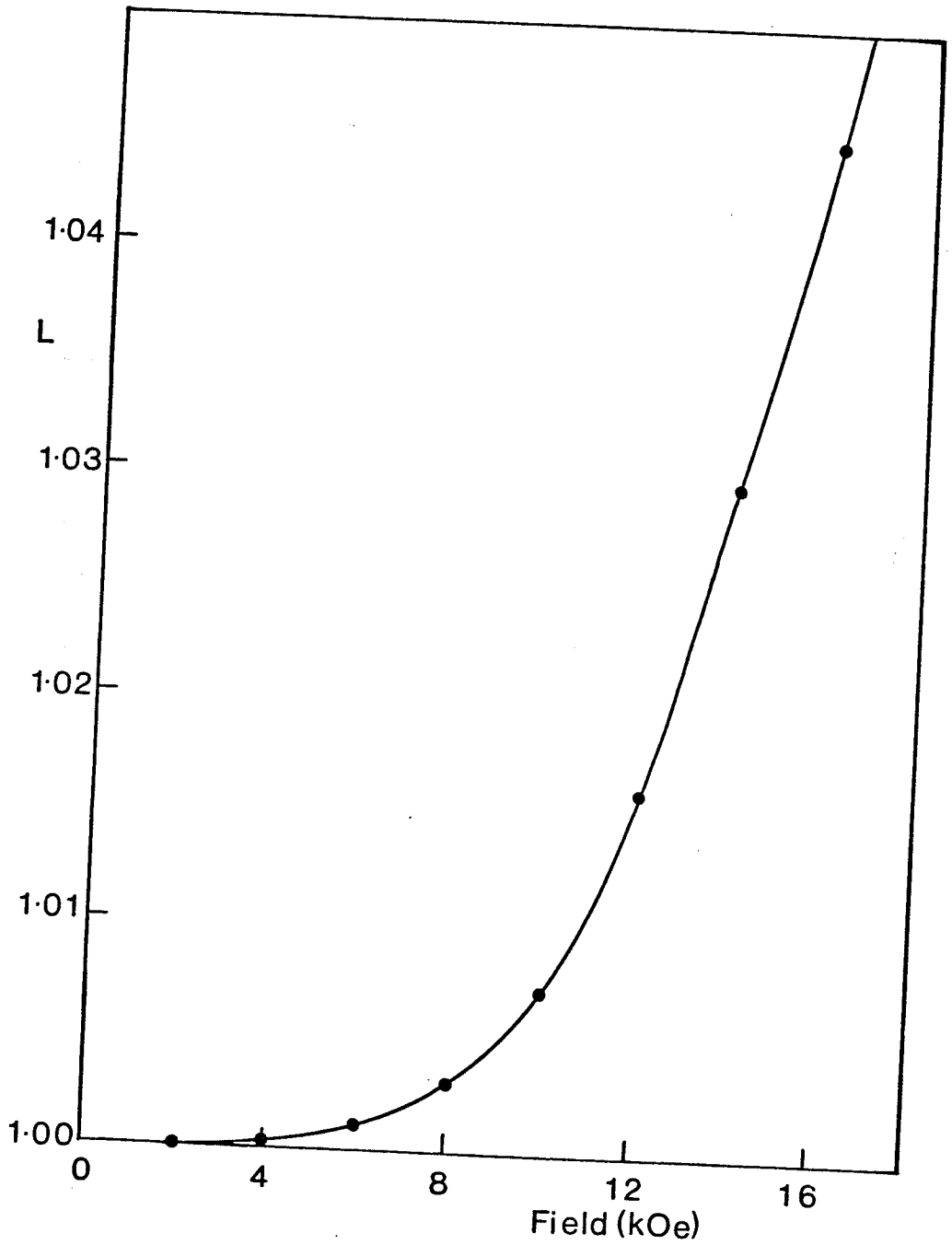

Figure 6.3.4-2 - Dependence of the image correction factor, L, on the applied field.

specimen. Corrected readings produced constant results above 8kOe. Using 55.11 emu/g as the saturation magnetization moment of nickel (Crangle and Goodman 1971), the calibration factor was determined to be (107.8 ± 0.5)emu/V.

6.3.6 Cold Finger

A 'cold finger' was used to make measurements of magnetization below room temperature. This consisted of four coaxial stainless steel tubes as shown in figure 6.3.6-1, numbered 1 to 4 from the innermost outward. Liquid nitrogen (or liquid helium for measurements below 77K) flowed down tube 1. The space between 1 and 2 was in vacuo. Nitrogen (or helium) gas flowed out between 2 and 3. The outermost space was also a vacuum. Tubes 1 and 2 were soldered to an oxygen-free copper block. A hole in the block permitted the outflow of gas. Teflon spacers prevented the tubes from coming into contact with each other. Bellows reduced the possibility of damage caused by thermal expansion and contraction.

The specimen was heated by nichrome wire which was wound around the top of the copper block. The resistance of the wire was 40Ω. Temperature was controlled using a feedback system with a gold-0.03 at.% iron thermocouple at the end of the heater.

The sample holder was threaded so as to screw onto the bottom of the copper block. It was made of copper or aluminum and slit lengthwise

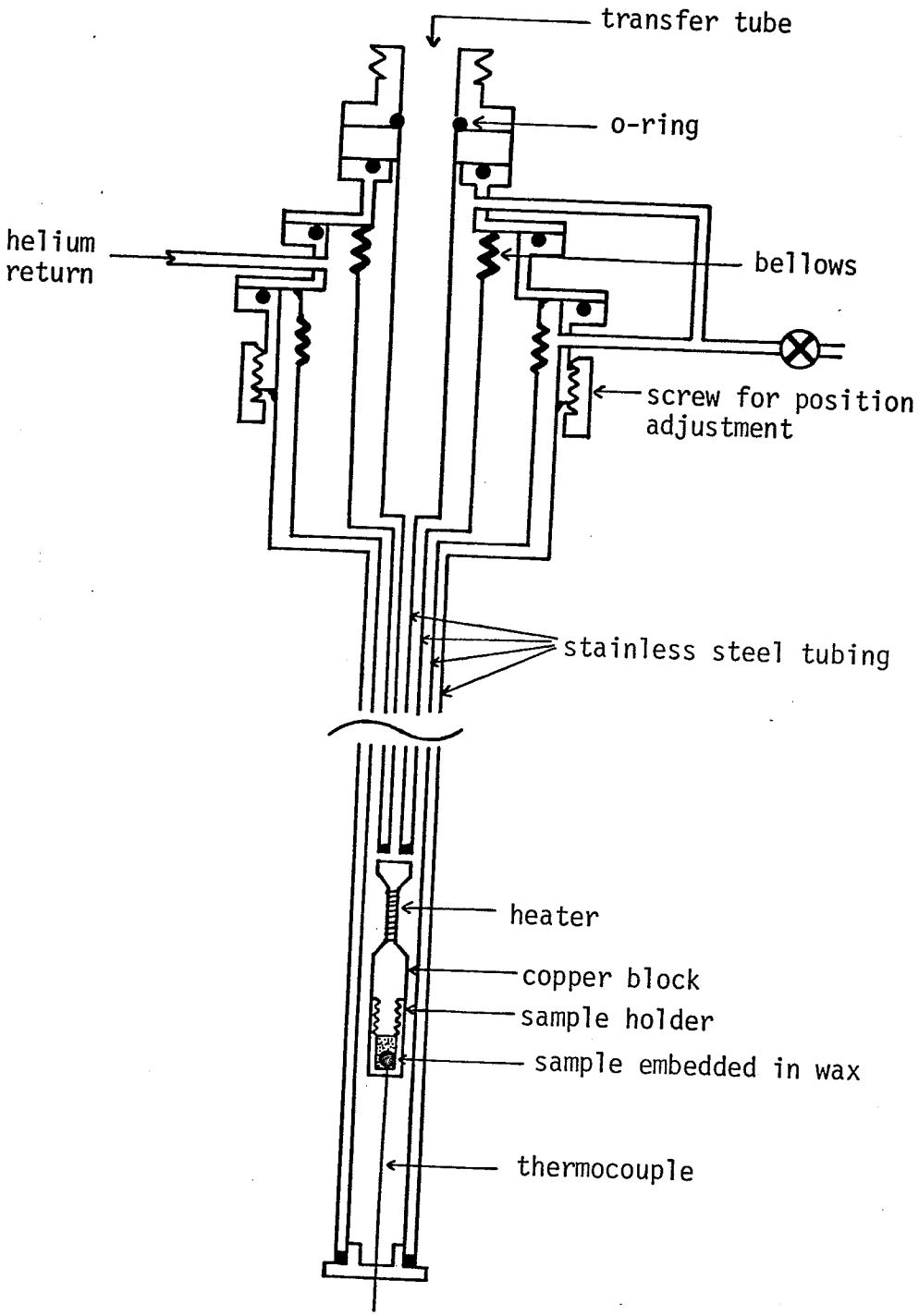

Figure 6.3.6-1 - Cold finger

to eliminate the possibility of eddy currents. It had two chambers. One contained the sample embedded in paraffin wax. The other had a copper plug screwed in. The plug was attached to a copper-constantan thermocouple which gave a direct measurement of specimen temperature.

Measurements were taken by moving the entire cold finger such that the sample was in or out of the sensing coils.

6.3.7 Room Temperature Measurements

For room temperature measurements the bulky cold finger arrangement was dispensed with. Here the sample holder was mounted on a threaded copper rod, which easily slid in and out of the coils.

6.4 Measurements in the Superconducting Magnet

6.4.1 Superconducting Magnet

Measurements of magnetization in fields up to 85kOe were made in a superconducting magnet manufactured by the Superconducting Helium Electronics Manufacturing Company.

The magnet consisted of a layer wound solenoid of filamentary superconducting Niobium-44% Titanium alloy conductors. The filaments were symmetrically arrayed in a high purity copper matrix. The windings were mechanically strengthened by impregnation with epoxy resin.

The solenoid was wound on a non-magnetic anodized aluminum former. The working bore was 40 mm and the length was 220 mm. The manufacturer's calculations indicated a vertical field homogeneity of 0.041% over a distance of 40 mm in the centre of the magnet.

The magnet was suspended in a Pope dewar by means of stainless steel tubes. This dewar contained liquid helium during operation, so as to keep the magnet in the superconducting state. It was placed in a second dewar filled with liquid nitrogen to minimize boil-off of liquid helium. Details of construction may be seen in figure 6.4.1-1. They have been further described by Hadjipanayis (1979).

6.4.2 High Temperature Insert

The high temperature insert was used to take measurements between 77K and 300K. It is detailed in figure 6.4.2-1 and has the following assembly. A copper nitrogen dewar jacket is vacuum isolated from the sample and helium spaces. The thermal mass of copper enables it to act as a heat sink to the furnace, preventing excessive helium boil off. This jacket contains a stainless steel tube, to the lower end of which is attached a flat ended copper tube which serves as the furnace. The copper tube has a groove along which the heater, a nichrome wire with resistance of 15Ω, runs up and down. Sensing and compensating coils are fixed at the lower end of the outer copper jacket. This portion of the jacket sits in the magnet bore.

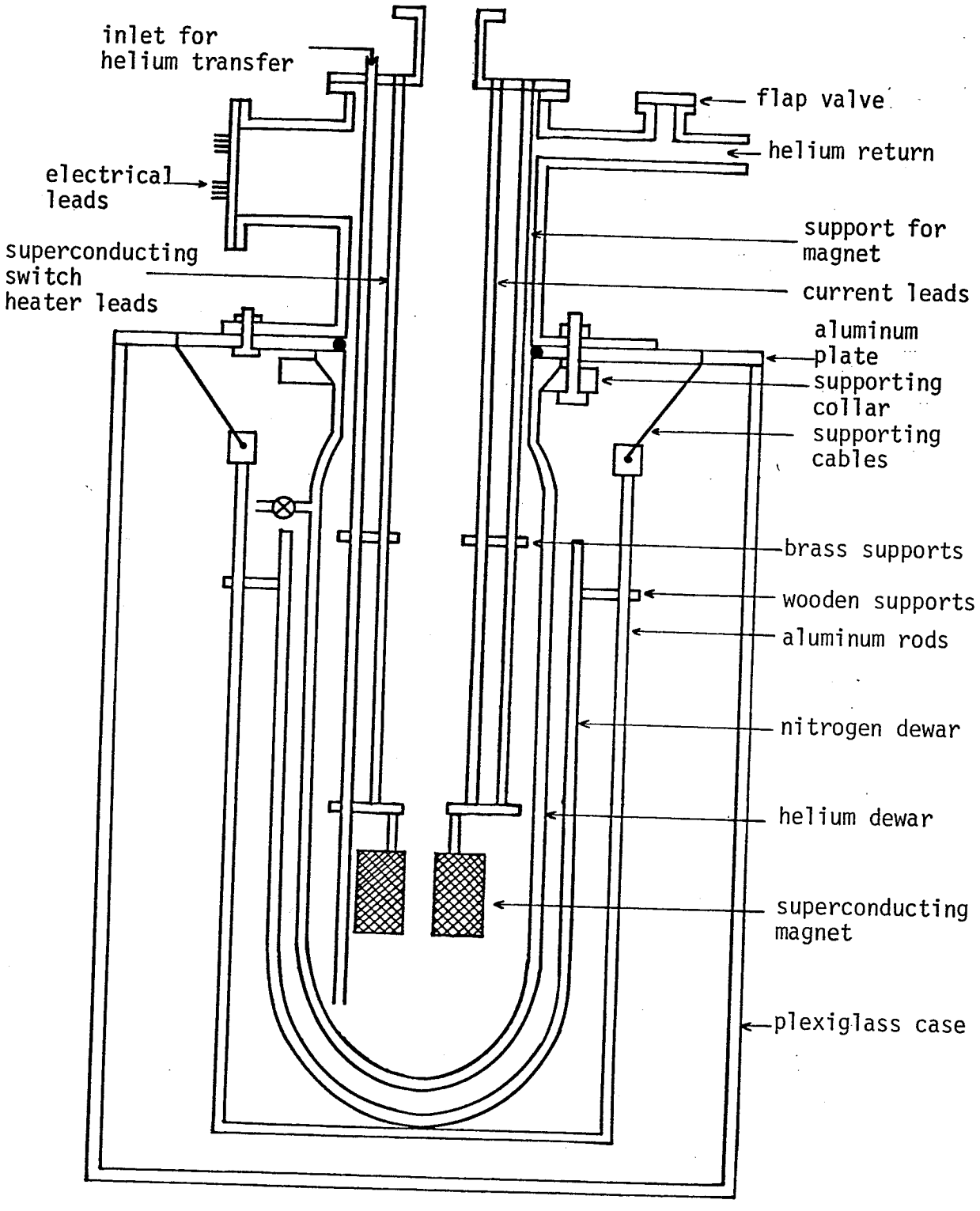

Figure 6.4.1-1 - Superconducting magnet
and cryostat

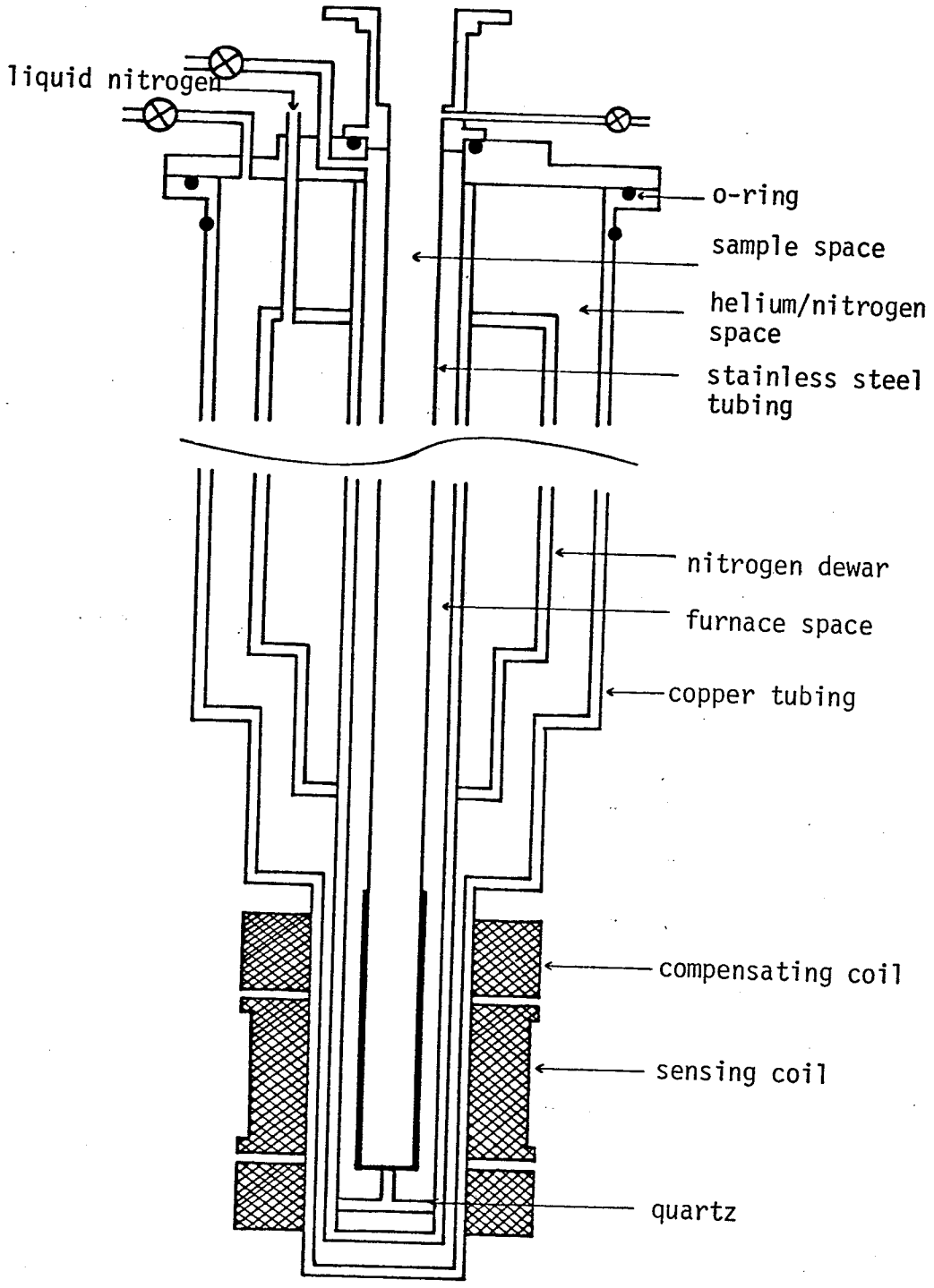

Figure 6.4.2-1 - High temperature insert

The sample is attached to the sample rod described in section 6.4.4. It is moved in and out of the sensing coils using a gas-powered piston. The range of movement is such that even when the sample is out of the sensing coils, it is still within the furnace, ensuring a constant temperature.

The furnace temperature was controlled using a null detector with analogue output. Temperatures were measured with a copper-constantan thermocouple which was coupled to the temperature controller. Using this arrangement it was possible to regulate temperatures to within 1K.

6.4.3 Low Temperature Insert

This insert, which can only be used at 4.2K, is shown in figure 6.4.3-1. The coils were compensated to give magnetization measurements to an accuracy of 0.01%. Here the sample sits in vacuo.

6.4.4 Sample Rod

The sample rod which was used with both inserts is shown in figure 6.4.4-1. The sample holders were hollow aluminum cylinders closed at one end and threaded at the other so as to screw on to the bottom of the sample rod. As previously, specimens were mounted in paraffin wax.

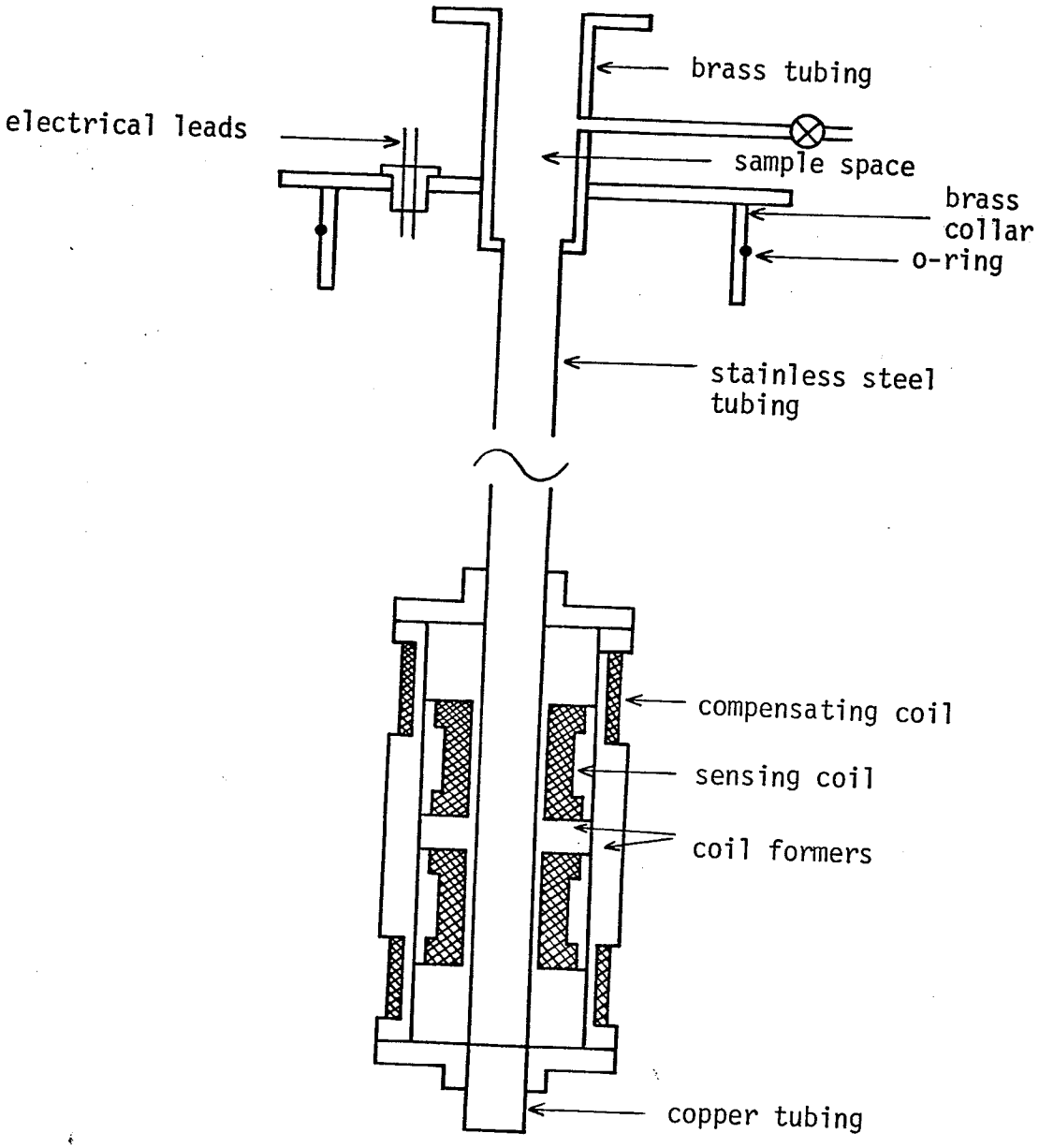

Figure 6.4.3-1 - Low temperature insert

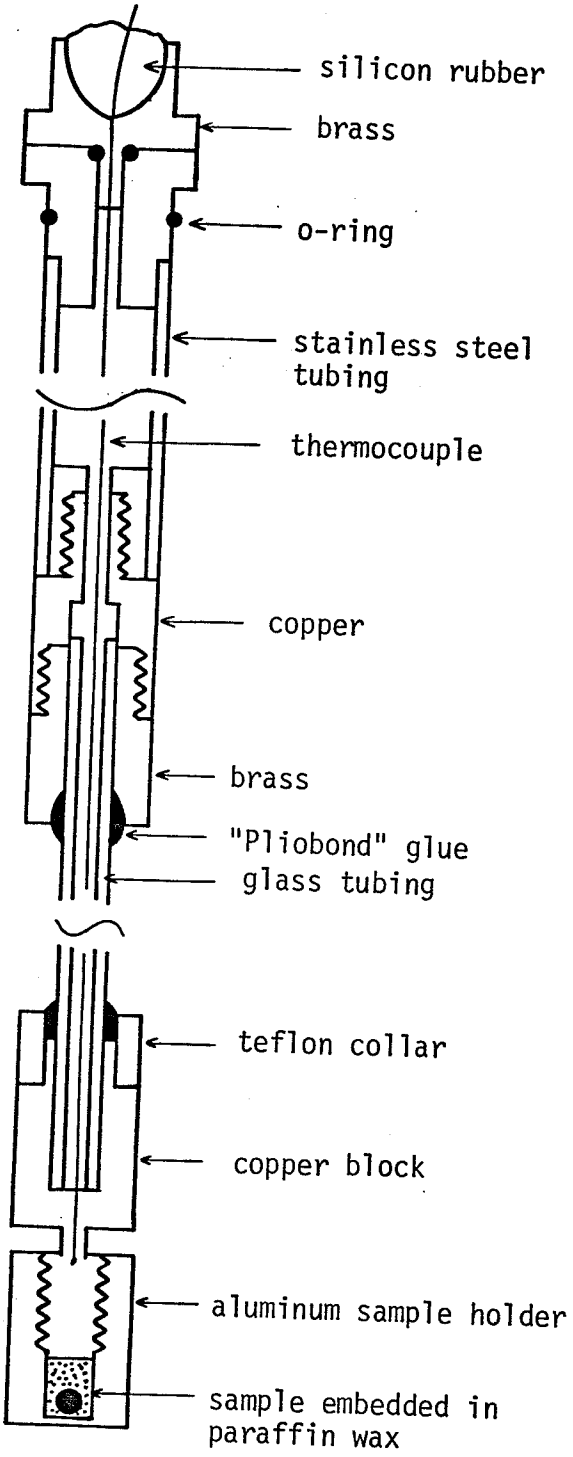

Figure 6.4.4-1 - Sample rod

6.4.5 Integrator

The integrator was the same as that used with the electromagnet.

6.4.6 Modifications to the Measuring Technique

Because of flux creep in the superconducting magnet, which is dealt with more fully in section 7.7, it was desirable to allow some time to elapse between extracting or inserting the specimen and taking the reading off the voltmeter. This would have allowed creep to decay. Any such delay, however, would have resulted in contributions to the reading from the integrator's drift and the longer the time lapse, the greater the magnitude of this effect. It was therefore necessary to employ a technique whereby the sample was successively lowered into and raised out of the sensing coils with integrator output voltage being read in each position. Using these readings it was possible to make corrections for the effects of flux creep and integrator drift as shown below.

Figure 6.4.6-1 shows how integrator output varies with time during a measurement. Initially the specimen is in the coil for a time t_1. If the integrator drift is b, then the reading at point A in the figure is:

$$V_A = bt_1$$

The specimen is then raised out of the coil and kept there for a

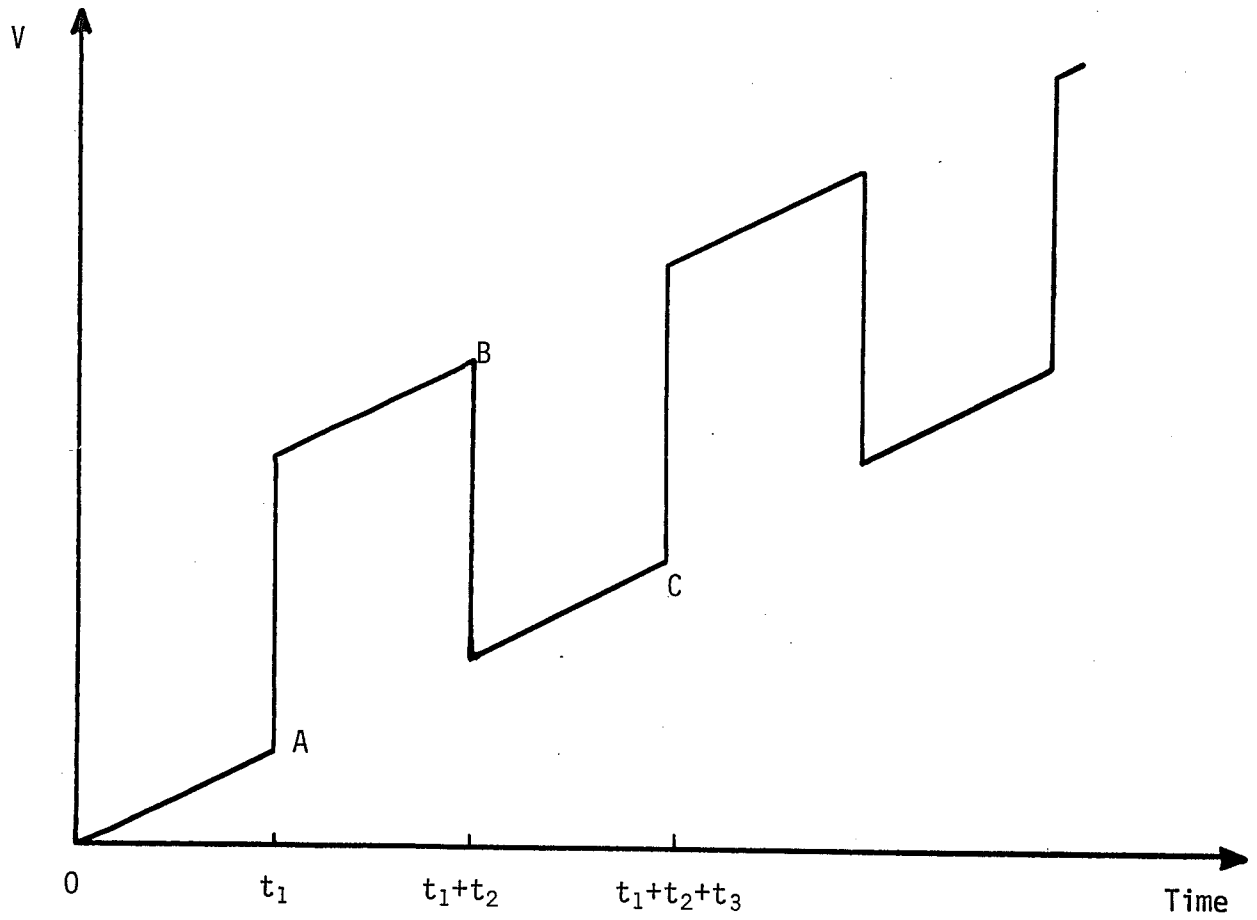

Figure 6.4.6-1 - Variation of integrator output with time during a measurement in the superconducting magnet.

time t_2. This corresponds to point B in the figure. The flux creep due to the imperfect Meissner effect during a time interval t is proportional to $M \ln(\frac{t_0+t}{t_0})$ when a specimen has magnetization M. This has been discussed more fully in section 7.7.

The reading at B is therefore,

$$V_B = V_A + c(M + aM \ln \frac{t_0+t_2}{t_0}) + bt_2$$

where a is a constant and c is the constant of the coil system that relates magnetization to the observed reading of voltage.

The specimen is then reinserted into the coil for a time t_3. The reading at this position (point C in the figure) is:

$$V_C = V_B - c(M + aM \ln \frac{t_0+t_3}{t_0}) + bt_3$$

This procedure is repeated several times.

The difference between V_A and V_B is

$$V_{BA} = c(M + aM \ln \frac{t_0+t_2}{t_2}) + bt_2$$

The difference between V_B and V_C is

$$V_{BC} = c(M + aM \ln \frac{t_0+t_3}{t_0}) - bt_3$$

The piston which moves the sample in and out of the sensing coils is controlled by a timer which ensures that $t_1=t_2=t_3= \ldots =t$, say.

The average difference between readings does not therefore include the contribution of drift, since

$$\bar{V} = cM\left(1 + a\, \ell n \frac{t_0+t}{t_0}\right)$$

i.e. $$M = K\bar{V} \quad ,$$

where K is a constant.

Thus, the value obtained when a number of such measurements are arranged is once again proportional to the magnetic moment of the specimen.

6.4.7 Calibration

Magnetization, it has been shown, is directly proportional to the integrator output, such that $M \propto \bar{V}$.

The necessary calibration was performed using an iron specimen as had been previously done by Rebouillat (1972). The calibration was valid in the range 20 to 70kOe. It was observed that K was field dependent and a polynomial fit was obtained using a least squares method.

For the high temperature coils,

$$K(H)_{H.T.} = 52.71536 + 6.79682H + 13.93258H^2 - 5.88728H^3$$

and for the low temperature coils,

$$K(H)_{L.T.} = 53.82651 - \frac{5.81619}{H} + \frac{3.75412}{H^2} - \frac{1.38369}{H^3} + \frac{0.29453}{H^4} - \frac{0.003377}{H^5} + \frac{0.00162}{H^6} ,$$

where H is in kOe.

6.5 Experimental Observations

6.5.1 Demagnetizing Factors

The demagnetizing factor, N is defined by Bozorth (1951) in the relationship,

$$H_D = NI \quad ,$$

where H_D is the demagnetizing field and I is the intensity of magnetization.

The effective field on the specimen,

$$H = H_a - H_D \quad ,$$

where H_a is the applied field.

Thus,

$$H_a = NI + H \qquad (6.5.1\text{-}1)$$

Initially H is zero, because the demagnetizing field perfectly compensates the applied field. In this region therefore, a linear relationship between applied field and magnetization exists and the

demagnetizing coefficient is obtained from the slope of the graph.

B was obtained in the unmagnetized state. Its initial magnetization was found to vary linearly with applied field. Such behaviour means that either there are no obstacles to domain wall motion, or any obstacles that are present are uniformly distributed. If the former is true, eq.(6.5.1-1) is obeyed and the slope of this linear region will give N. These measurements were made at room temperature in the electromagnet.

All specimens were either prolate or oblate ellipsoids. Their theoretical demagnetizing coefficients were obtained by measuring their dimensions and referring to the charts of Osborn (1945). These values were compared with the values of N determined experimentally.

Table 6.5.1-1 exhibits the results of these determinations. Agreement between both sets of values are excellent, ranging from 96 to 100%. This is consistent with the type of behaviour that is displayed by a soft ferromagnet in which there is no trapping of domain walls.

6.5.2 Reversibility of Magnetization

A virgin specimen was magnetized in the electromagnet at room temperature in incrementally increasing fields. Each insertion into the magnet was followed by measurement of magnetic moment and remanence. Initially the magnetization was almost completely reversible with coercivity rising to 0.15kOe when a magnetic intensity of 48.6 emu/g

Table 6.5.1-1

Comparison of Demagnetizing Factors

N from magnetization measurements	N from dimensions	Difference (as a percentage)
5.18	4.96	4.4
4.84	4.71	2.8
4.16	4.17	0.2
2.59	2.56	1.2

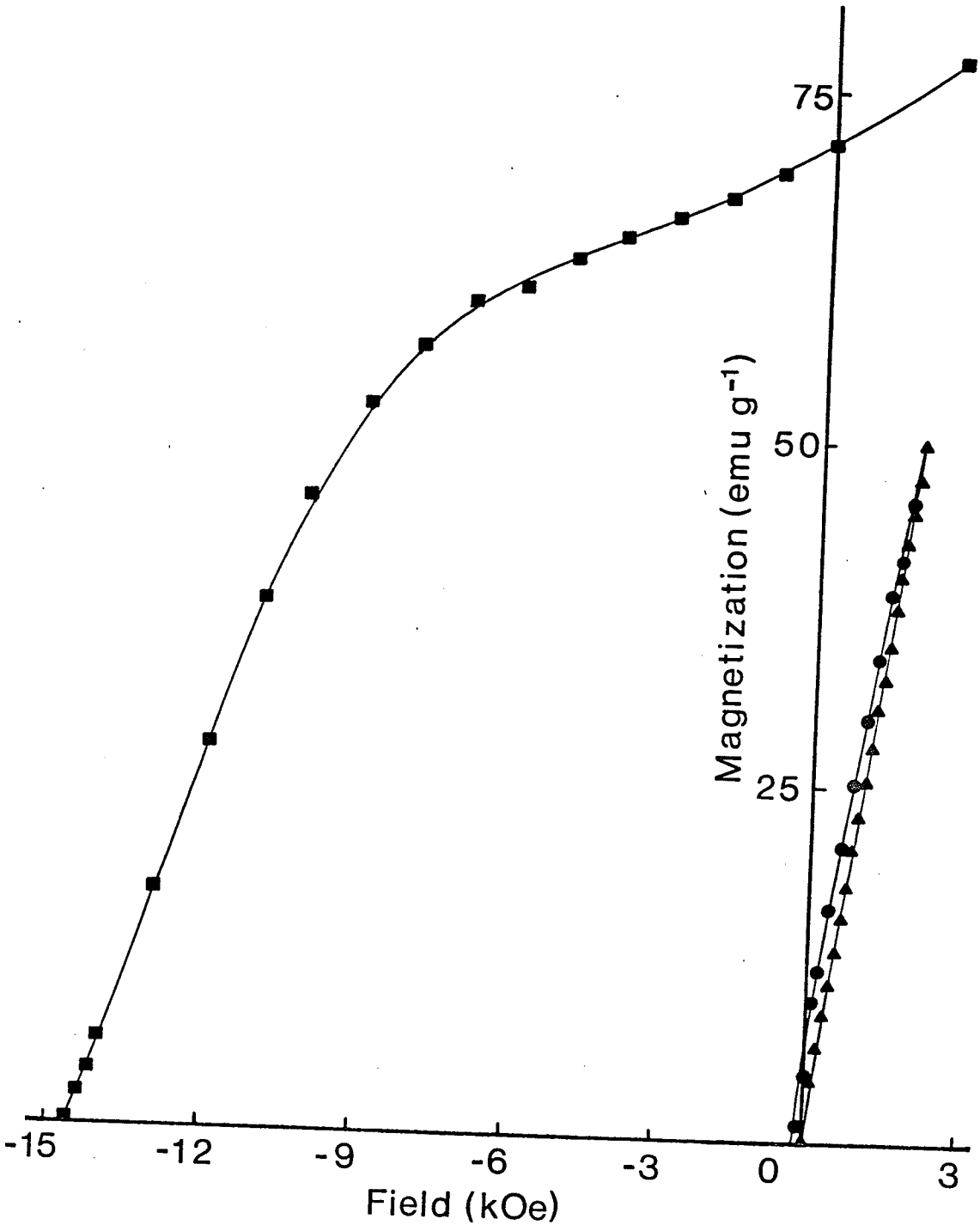

Figure 6.5.2-1 - Magnetization curves for specimen B at room temperature. The initial magnetizing (triangles) and demagnetizing (circles) curves are shown, as well as the demagnetizing curve (squares) after application of a larger field.

was reached. This occurred when a field of 2kOe had been applied and is shown in figure 6.5.2-1. However, as seen in the same figure, when the field was increased to 2.5kOe, the specimen reached an intensity of 75.0 emu/g, which was later discovered to be its saturation intensity and the coercivity jumped to its maximum value for that specimen of 14.6kOe.

The departure of magnetization from a reversible path coincided with the appearance of a non-zero effective field and occurred only when the magnetic moment had reached 65% of its saturation moment. This meant that 82% of the volume was magnetized in the forward direction and 18% in the reverse direction, indicating that domain walls were free to sweep through 82% of the specimen with little or no impedance. Since the maximum demagnetizing field was reached shortly after the first appearance of hysteresis, it seems apparent that trapping of domain walls is a highly localized phenomenon.

6.5.3 Coercivity

Measurements of coercive field were made in the superconducting magnet, using the appropriate inserts. The specimen was first magnetized to saturation in a field of 75kOe and then gradually demagnetized. An entire major hysteresis loop was obtained and the field at which magnetization disappeared, the coercive field, was thus determined. This procedure was followed for each specimen at 4.2, 77, 200 and 300K.

Table 6.5.3-1 gives the variation of coercivity with temperature for each specimen. These coercivities, when normalised at 77K, are, as shown in figure 6.5.3-1, consistent with the data of Benz and Martin (1972) which has been discussed in section 4.14.

Figure 6.5.3-2 is the demagnetizing portion of the hysteresis loop obtained for specimen B at 200K. It was typical of all the loops observed in its 'square' shape, indicative of the hardness of the material.

6.5.4 Discussion

The results of sections 6.5.1 and 6.5.2 show that domain walls are able to move without hindrance over 82% of the material. The large coercivities that appear shortly after the first evidence of domain wall pinning indicate that pinning sites are concentrated at certain regions and are not evenly distributed throughout the material. This is consistent with observations made by Livingston (1973) in which he used the Kerr effect to show that pinning sites in sintered $SmCo_5$ were concentrated at grain boundaries.

The resulting picture therefore, is of a material in which domain walls are able to move freely through the bulk of the material, but are trapped by highly localized concentrations of pinning sites. This is extremely significant, for it is an important basis of the model developed in chapters 3 and 4.

Table 6.5.3-1

Measured Coercive Fields (kOe)

Specimen \ Temperature (K)	4.2	77	200	300
B	20.50	20.20	16.02	11.74
C	38.55	35.47	30.50	22.44
M	43.70	46.90	36.10	25.33

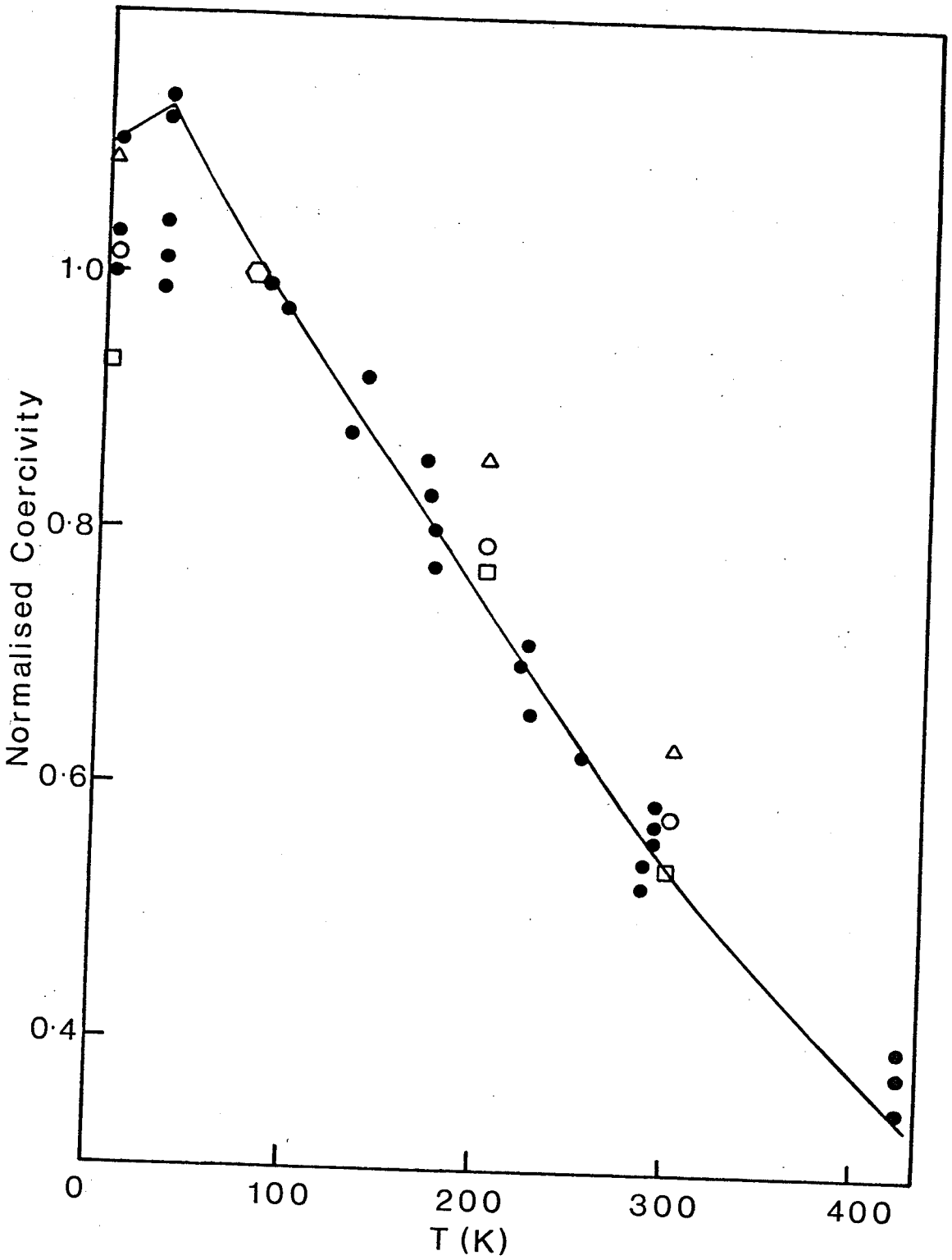

Figure 6.5.3-1 - Variation of coercive field normalised at 77K with temperature for specimens B (circle), C (triangle) and M (square). The hexagon at 77K is common to all specimens. The filled circles are from the data of Benz and Martin (1972).

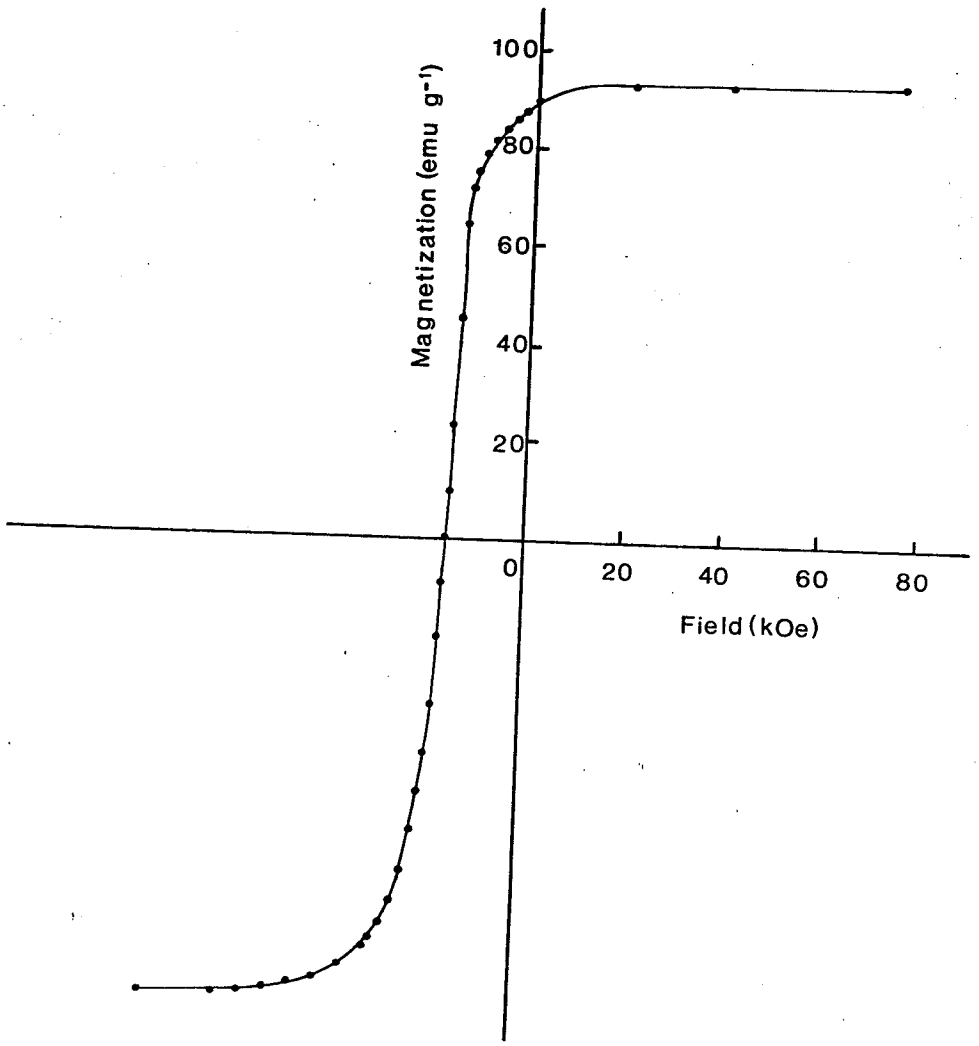

Figure 6.5.3-2 - Demagnetizing portion of the hysteresis loop for specimen B at 200K.

CHAPTER 7

MAGNETIC AFTER-EFFECT

7.1 Introduction

Consider a magnetic field applied to a ferromagnetic material. If the field is suddenly changed, the resulting change in the material's magnetization is more gradual (Figure 7.1-1). This time lag is, in many cases, due to eddy currents, but in some materials the change in magnetization persists for too long to be explained away by this phenomenon. These materials are said to exhibit 'magnetic viscosity'.

Experiments by Street and Woolley (1949) demonstrated that for alnico, the change in magnetization per unit volume varied linearly with the logarithm of time:

$$\Delta I = S \ln t$$

S is known as the viscosity parameter.

This logarithmic behaviour is also exhibited by $SmCo_5$ as shown by the experimental results detailed later in this chapter. This implies the presence of a range of activation energies, as will be shown below.

7.2 Viscosity with a Range of Activation Energies

The following treatment is essentially that of Gaunt (1976). From eq.(3.7-1) we had:

$$\tau^{-1} = C \exp(\frac{-E}{kT}).$$

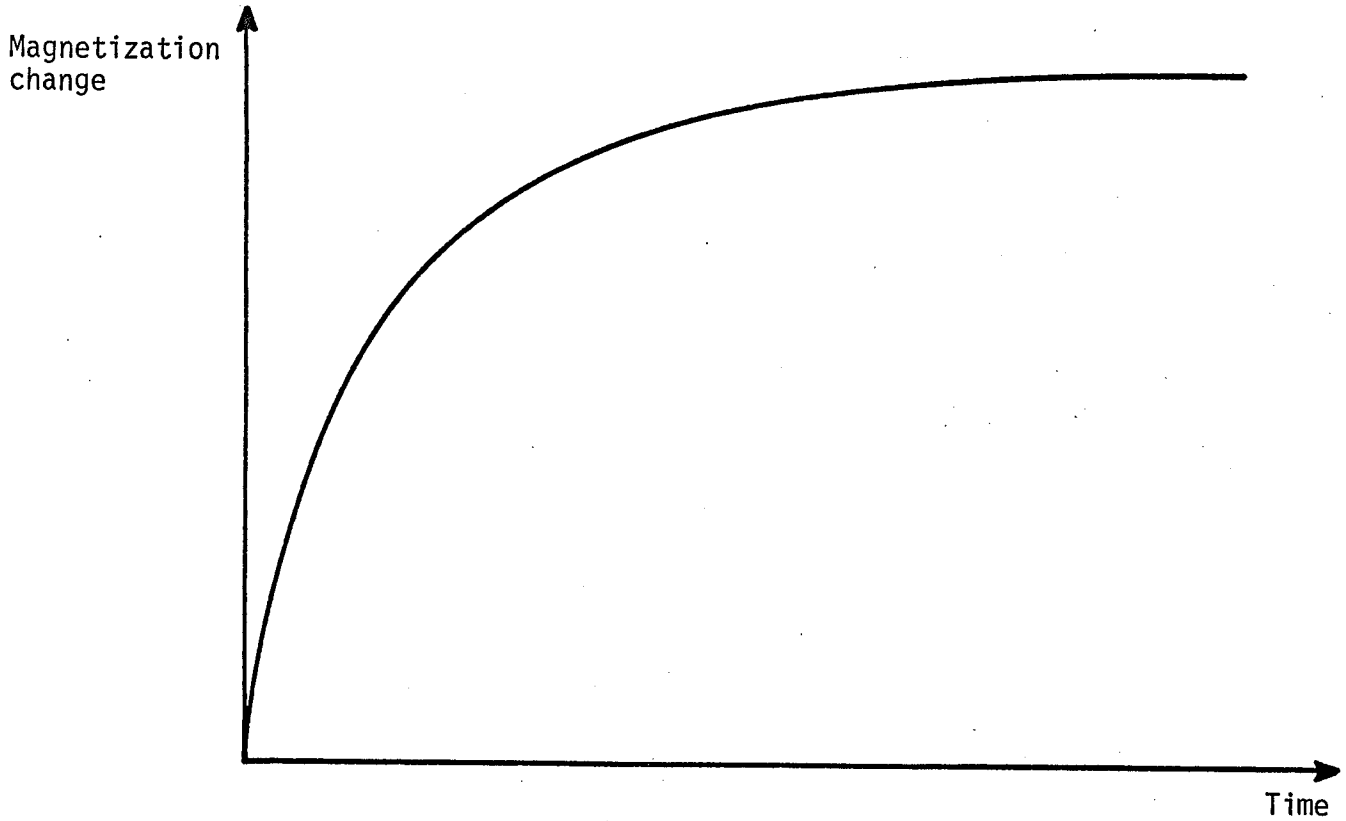

Figure 7.1-1 - Magnetic after-effect

Then, if I_0 is the saturation magnetization and I is the magnetization per unit volume at time t,

$$\frac{dI}{dt} = -C(I_0 + I)\exp(\frac{-E}{kT}) \quad , \tag{7.2-1}$$

where E is the activation energy required to jump over barriers in a reverse field, H.

Integrating eq.(7.2-1),

$$I = 2I_0 \exp[-Ct \exp(\frac{-E}{kT})] - I_0 \quad . \tag{7.2-2}$$

We see that if E has a single value, I must then vary exponentially with time.

Suppose, however, that there exists a range of activation energies and the barriers have an energy dependent distribution function f(E), such that:

$$\int_{-\infty}^{\infty} f(E)dE = 1$$

Then, eq.(7.2-2) is rewritten as:

$$I = 2I_0 \int_{0}^{\infty} \exp[-Ct \exp(\frac{-E}{kT})]f(E)dE - I_0 \tag{7.2-3}$$

where the integral is carried out over positive energies only, because negative activation energies correspond to instantaneous reversals which are not observed in an after effect measurement.

Differentiating eq.(7.2-3) with respect to ℓnt,

$$\frac{dI}{d(\ell nt)} = -2I_0 \int_0^\infty Ct \exp(\frac{-E}{kT}) \exp[-Ct \exp(\frac{-E}{kT})] f(E)dE \qquad (7.2\text{-}4)$$

Let

$$\lambda = Ct \exp(\frac{-E}{kT}) \qquad (7.2\text{-}5)$$

Then eq.(7.2-4) reads:

$$\frac{dI}{d(\ell nt)} = -2I_0 \int_0^\infty \lambda \exp(-\lambda) f(E)dE \qquad (7.2\text{-}6)$$

Since $\lambda \exp(-\lambda)$ is a sharply spiked function, with non zero values over a very small range of E and since f(E) varies slowly in comparison, we can write

$$\frac{dI}{d(\ell nt)} \simeq -2I_0 f(E') \int_0^\infty \lambda \exp(-\lambda)dE \quad , \qquad (7.2\text{-}7)$$

where $E' = kT\ \ell nCt$, the value of the energy when $\lambda \exp(-\lambda)$ takes its maximum value at $\lambda = 1$.

From eq.(7.2-5),

$$d\lambda = -\frac{\lambda}{kT} dE$$

Then,

$$\int_0^\infty \lambda \exp(-\lambda)dE = kT \int_0^{Ct} \exp(-\lambda)d\lambda$$

$$= -kT[1 - \exp(-Ct)]$$

Substituting this into eq.(7.2-6), if $Ct \gg 1$,

$$\frac{dI}{d(\ell nt)} = 2I_0 kTf(E') = S, \text{ say.} \qquad (7.2\text{-}8)$$

In many experiments, this slope S is a constant for a time range 0.5 to 1000 seconds. This implies that the distribution function f(E') does not vary for the energy range 24.3kT to 31.9kT. Viscosity experiments therefore serve to probe the distribution of energy barriers over a range of approximately 7.6kT.

7.3 Effect of Change Due to the Magnetic Field

Differentiating eq.(7.2-2) ,

$$\left(\frac{\partial I}{\partial H}\right)_T = 2I_0 \frac{1}{kT} Ct \exp\left(\frac{-E}{kT}\right)\left[\exp -Ct \exp\left(\frac{-E}{kT}\right)\right]\left(\frac{\partial E}{\partial H}\right)_T dE$$

or

$$kT\left(\frac{\partial I}{\partial H}\right)_T = 2I_0 \lambda \exp(-\lambda)\left(\frac{\partial E}{\partial H}\right)_T dE$$

This is the expression for a single activation in the range E to E + dE.

Over the entire range of activation energies therefore,

$$kT\left(\frac{\partial I}{\partial H}\right)_T = 2I_0 \int_0^\infty \lambda \exp(-\lambda)\left(\frac{\partial E}{\partial H}\right)_T f(E)dE$$

Assume once again that $(\frac{\partial E}{\partial H})_T f(E)$ is slowly varying, compared with the spiked function $\lambda\exp(-\lambda)$.

$(\frac{\partial I}{\partial H})_T$ is the irreversible susceptibility, χ_{irr}

Then,

$$kT\ \chi_{irr} = 2I_0(\frac{\partial E'}{\partial H})_T f(E') \int_0^\infty \lambda\exp(-\lambda)dE \qquad (7.3\text{-}1)$$

where once again

$$E' = kT\ \ell n(Ct)$$

Comparison of eqs.(7.2-7) and (7.3-1) show that

$$(\frac{\partial E'}{\partial H})_T = \frac{-kT\ \chi_{irr}}{S} \qquad (7.3\text{-}2)$$

This expression uses the irreversible susceptibility χ_{irr}.

χ_{irr} and S can be determined experimentally at a particular temperature and thus the value of $(\frac{\partial E}{\partial H})_T$ can be obtained for the barriers active during the experiment.

An expression for the theoretical distribution of energy barriers has already been derived as

$$(\frac{\partial E}{\partial H})_T = \frac{-4\pi NI\gamma b^2}{F} \qquad (3.5\text{-}6)$$

The parameters for this expression have been calculated in chapter 4 by combining the micromagnetic calculation of chapter 4 with

the parabolic force model of chapter 3. A purely theoretical $(\frac{\partial E}{\partial H})_T$, which is the value at the coercive field, H_c, can thus be obtained. The results from eqs.(3.5-6) and (7.3-2) may be compared.

7.4 Demagnetization Corrections to the Viscosity Parameter, S

As the magnetization changes due to thermal activation, the demagnetizing field will change. This causes a further change in magnetization which will also be recorded as an after-effect. The total after-effect, therefore, is not caused entirely by thermal activation and the following correction must be made if the true viscosity coefficient is to be calculated.

If I is the observed change in magnetization, the rate of change of I with ℓnt is given by:

$$\frac{dI}{d(\ell nt)} = \frac{\partial I}{\partial(\ell nt)} + \frac{\partial I}{\partial H}\frac{dH}{d(\ell nt)} \qquad (7.4\text{-}1)$$

The change in the demagnetizing field for a magnetization change dI, when D is the demagnetizing coefficient is:

$$dH = -DdI \qquad (7.4\text{-}2)$$

The observed viscosity coefficient,

$$S_{obs} = \frac{dI}{d(\ell nt)} \qquad (7.4\text{-}3)$$

Let

$$S' = \frac{\partial I}{\partial(\ell nt)} \tag{7.4-4}$$

The susceptibility,

$$\chi = \left(\frac{\partial I}{\partial H}\right)_T \tag{7.4-5}$$

where we assume that χ is invariant over the measurement.

Substituting from eqs.(7.4-2) to (7.4-5) into eq.(7.4-1), we get

$$S_{obs} = S' - D\chi S_{obs} \tag{7.4-6}$$

Now,

$$\Delta I = \chi \Delta H$$

and

$$\Delta I_{irr} = \chi_{irr} \Delta H \ ,$$

where I_{irr} is the irreversible change in magnetization.

Then,

$$\Delta I_{irr} = \frac{\chi_{irr}}{\chi} \Delta I \tag{7.4-7}$$

But

$$S = \frac{\partial I_{irr}}{\partial(\ell nt)}$$

From eqs.(7.4-4) and (7.4-7) therefore,

$$S' = \frac{\chi}{\chi_{irr}} S$$

Substituting into eq.(7.4-5),

$$S = \left[\frac{(1+D\chi)\chi_{irr}}{\chi}\right] S_{obs}$$

and this is the correction to the observed viscosity.

Substituting this into eq.(7.3-2), we get:

$$\left(\frac{\partial E}{\partial H}\right)_T = - \frac{kT\chi}{(1+D\chi)S_{obs}} \qquad (7.4\text{-}8)$$

where S_{obs} is the observed viscosity coefficient and χ is the magnetic susceptibility.

7.5 Quantum Mechanical Tunneling

Magnetic after-effect is observed when domain walls receive enough energy to overcome energy barriers. In the preceding chapters thermal activation of walls has been considered and with such a model the magnitude of after effect will be temperature dependent. However, Egami (1973) has observed that below 10K, Dy has a temperature independent after-effect, implying the presence of some other mechanism. This can be understood if the system is treated quantum mechanically, rather than classically as has heretofore been done. The wall is now treated as a particle of finite mass, sitting in a potential well. All facets of a quantum mechanical problem can therefore be exhibited and the most important of these is the phenomenon of tunneling through the energy barrier.

Egami (1973) has shown theoretically that the temperature at which tunneling begins to dominate thermal activation as a mechanism for domain wall escape is consistent with his experimental observations.

In the experiments on $SmCo_5$ that were carried out in this study, no measurable after-effects were observed at 4.2K. This is consistent with model calculations in section 7.8.3 which showed that after-effect at this temperature would be smaller than experimental error. Since thermal activation effects are less evident at low temperatures, any after-effect at this temperature may be adduced to tunneling. The apparent absence of such effects would seem to imply that tunneling effects are negligibly small in $SmCo_5$, as the following calculation shows.

If a particle of mass M and zero kinetic energy attempts to tunnel through a rectangular energy barrier of height E and width t, the probability of penetrating the barrier is, from Fermi (1949),

$$P_1 = C \exp\left[-2\left(\frac{2MEt^2}{\hbar^2}\right)^{\frac{1}{2}}\right] \qquad (7.5\text{-}1)$$

where C is a constant and may be regarded as the attack frequency used in eq.(3.7-1).

The probability of escape by thermal activation is

$$P = C \exp\left(\frac{-E}{kT}\right) \qquad (3.7\text{-}1)$$

Thus, if tunneling is to dominate thermal activation as the mode of escape, it is plain from eqs.(7.5-1) and (3.7-1) that

$$2\left(\frac{2MEt^2}{\hbar^2}\right)^{\frac{1}{2}} \quad < \quad \frac{E}{kT} \qquad (7.5\text{-}2)$$

In the present problem the shape of the barrier is not rectangular. However, since an exact solution is not required, the following treatment may be used.

As seen in figure 3.4-1, the element of wall rdr has to travel a distance $z-z_0$ before it escapes. Then, if the wall has an area a,

$$at^2 = \int_0^\infty 2\pi r(z-z_0)^2 dr$$

and from section 3.4,

$$Mt^2 = \sigma\frac{\pi\gamma}{H_0 I} b^2 \left(1 - \frac{H}{H_0}\right)^{\frac{1}{2}} L \qquad (7.5\text{-}3)$$

where $$L = \int_0^\infty R\,(Z+1)^2\, dR$$

and $$\sigma = \frac{\gamma}{8\pi\nu^2 A}\,, \qquad (7.5\text{-}4)$$

the mass per unit area of the wall (Morrish 1965).

In eq.(7.5-4), ν is the Larmor precession frequency, $\frac{ge}{2m}$, where e is the electronic charge in emu,

m is the electronic mass

and g is the Landé g-factor, equal to 2.

This gives $\nu = 1.76 \times 10^7 Hz$

The height of the energy barrier is, from eq.(3.5-4),

$$E = 2\pi N\gamma b^2 (1 - \frac{H}{H_0}) \qquad (7.5\text{-}5)$$

Substituting for Mt^2 and E from eqs.(7.5-3) to (7.5-5) and remembering that from eq.(3.7-1), $E = 25kT$ for thermal activation to take place, the temperature at which tunneling begins to dominate thermal activation,

$$T_t = \left[(50\pi)^{1/4} \frac{N^{1/4}}{L^{1/2}} \frac{\hbar}{k^{3/4}} \nu \frac{A^{1/2}(H_0 I)^{1/2}}{\gamma^{3/4} b}\right]^{4/3} \qquad (7.5\text{-}6)$$

From section 3.6, $N = 4.929$

and $L = 9.865.$

Also, from chapter 4,

$\gamma \simeq 80$ erg/cm^2 ,

$b \simeq 1 \times 10^{-7}$cm ,

$H_0 \simeq 5 \times 10^4$Oe ,

$I \simeq 1 \times 10^3$emu/cm^3

and $A \simeq 7 \times 10^{-7}$erg/cm ,

at 4.2K. It will be assumed that these values are invariant at low temperatures. Earlier in this section, it was seen that $\nu = 1.76 \times 10^7 Hz$.

Substituting the above values into eq.(7.5-6) gives

$$T_t = 2.0 \times 10^{-2}K$$

Therefore tunneling begins to dominate thermal activation only below temperatures of the order of $10^{-2}K$. Since thermal activation effects at even 4.2K could not be measured, tunneling could not have played a part in the measurements of magnetic after-effect that were carried out in this study.

7.6 Experimental Technique

Magnetic after-effect was measured in the electromagnet using, by and large, the same apparatus as that used for magnetization measurements and described in chapter 6.

The flux change measured here was that due to thermal activation and the specimen therefore sat in the field and sensing coil throughout the measurement. The experimental procedure was as follows. The specimen was placed in a large forward field and then withdrawn. A reverse field was then generated and the specimen thrust into this field. The change in magnetization after the initial instantaneous domain reversal process and after drift in the electronics had been subtracted, was the magnetic after-effect. This was observed on a chart recorder connected to the output of the integrator. The chart paper moved at a speed of 8 inches per minute. Measurements were taken to

64 seconds. Total magnetization was measured by removing the specimen from the coil as described earlier.

The theory used was the one where a range of activation energies was assumed, suggesting a logarithmic variation in time as given by eq.(7.2-8). To verify that the variation of magnetization was indeed logarithmic in time and not exponential, it was necessary to measure time from as close to t = 0 as possible. To facilitate this, a pressure-activated microswitch for the integrator was attached to the sample holder. When the specimen was thrust into the magnetic field, the switch made contact with the superstructure of the magnet, turning on the integrator. This eliminated any delays that may have been caused by manual switching. The microswitch was positioned so as to turn on the integrator only when the entire sample was in the sensing region.

Using this system time effects were measured at fields of up to 17kOe at temperatures ranging from 4.2K to room temperature (295K).

7.7 Flux Creep caused by the Superconducting Magnet

Magnetic flux cannot penetrate type I superconductors. The phenomenon of instantaneous flux expulsion as such a material is cooled to its superconducting state is known as the Meissner effect. Type II superconductors exhibit the incomplete Meissner effect, where the expulsion of flux is more gradual. Here, if a magnetized specimen is placed in the vicinity of a superconductor, flux which initially

penetrates the superconductor will, with time, be expelled and there will be a gradual increase in the concentration of flux in the space between the specimen and the superconductor.

Since superconducting magnets are made of type II superconductors, they exhibit the incomplete Meissner effect. When a magnetized specimen is thrust into the magnet therefore, the flux change caused by the initial change in magnetization is followed by a slower increase caused by the expulsion of flux from the magnet windings. This time effect will be detected by the sensing coil which sits within the magnet and around the specimen.

Rebouillat (1972) has shown that when a specimen has a magnetic moment, M the change in flux, $\Delta\phi$, with time, t, is given by:

$$\Delta\phi \propto M \ln \frac{t + t_0}{t}$$

where t_0 is a constant dependent on the base of the logarithm. This expression is valid to a time t = 140 seconds.

$\Delta\phi$ is logarithmic with time and is therefore difficult to separate from the magnetic after-effect which is also logarithmic.

To measure magnetic after-effect, the field must be changed. Such a change will once again result in flux creep that will be measured in the sensing coils. Since magnetic viscosity effects are most observable at small times, it is not feasible to wait until creep dies away.

Both these effects therefore will be seen in any measurement of after-effect and when trial measurements were made, it was observed that

they totally dominated and as a result obscured the true magnetic viscosity of the specimen.

Consequently, magnetic after-effect could not be measured at high fields in the superconducting magnet, using the available systems. This restricted viscosity measurements to the electromagnet and a maximum field of 17kOe.

7.8 Experimental Observations

7.8.1 Determining the Energy Barrier Distribution, $(\frac{\partial E}{\partial H})_T$

Magnetic after-effect was measured for each sample at temperatures of 4.2, 77, 200 and 295K. The experimental technique has been described in section 7.6.

Measurements were made at various fields. For each individual field the corrected magnetization change was plotted against the logarithm of time. The graphs were observed to be linear, verifying eq.(7.2-8) which was valid when a range of activation was present. The slope, S_{obs}, was calculated. This was the observed viscosity coefficient of the specimen at that field and temperature.

Since magnetization, M, was measured for each after-effect measurement, it was possible to calculate the effective field on the specimen.

Effective field,

$$H_{eff} = H_a - DM \ ,$$

where H_a is the applied field and D is the demagnetizing coefficient, determined in section 6.6.1.

The specimen sees this effective field and not the applied field. It is therefore the more fundamental quantity and future references to 'field' in this chapter will be to the effective field.

M was plotted against H_{eff} and the susceptibility χ was thus calculated at the fields at which after-effect was measured, giving a set of simultaneous values of S_{obs} and χ. (Figure 7.8.1-1 shows the variation of S_{obs} and χ with field for specimen C at 200K). Using these values in eq.(7.4-8), $(\frac{\partial E}{\partial H})_T$ was calculated. It was convenient to plot $(\frac{\partial E}{\partial H})_T$ against H_{eff}^{-1} and such graphs were plotted at temperatures of 77,200 and 295K for all three specimens. They are shown in figures 7.8.1-2 to 7.8.1-4. It can be seen in all cases that $(\frac{\partial E}{\partial H})_T$ decreases as the field increases.

The theoretical values of $(\frac{\partial E}{\partial H})_T$ which were calculated from eq.(3.5-6) and shown in table 7.8.1-1 are also plotted on these graphs. As mentioned in section 7.7, it was only possible to measure after-effect in the electromagnet and as such, an experimental value of $(\frac{\partial E}{\partial H})_T$ at the coercive field could not be obtained for a direct comparison with the theoretical values. However, in all cases, the graphs appear to extrapolate to the theoretical $(\frac{\partial E}{\partial H})_T$.

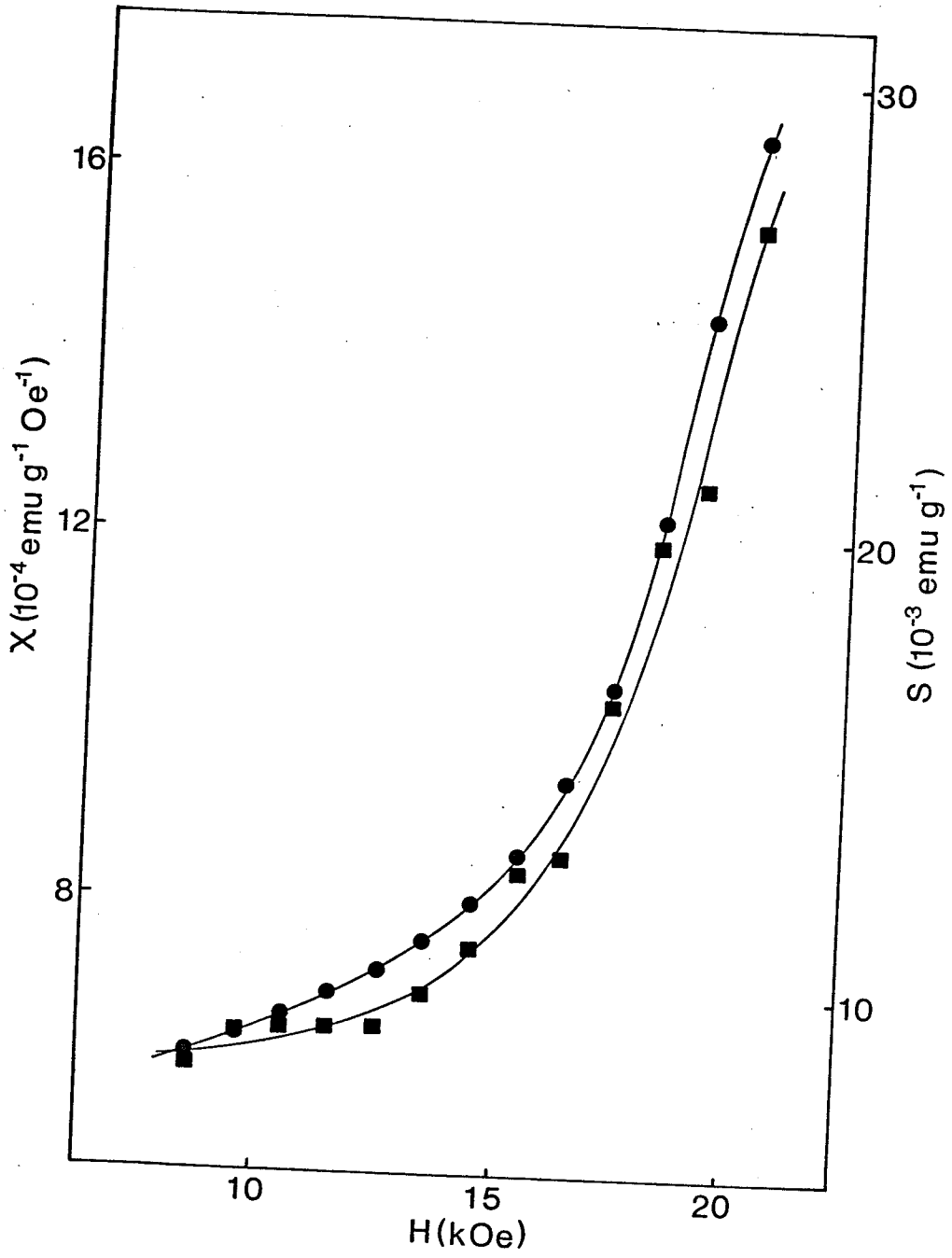

Figure 7.8.1-1 - Susceptibility (circles) and viscosity coefficient (squares) plotted against the effective field for specimen C at 200K.

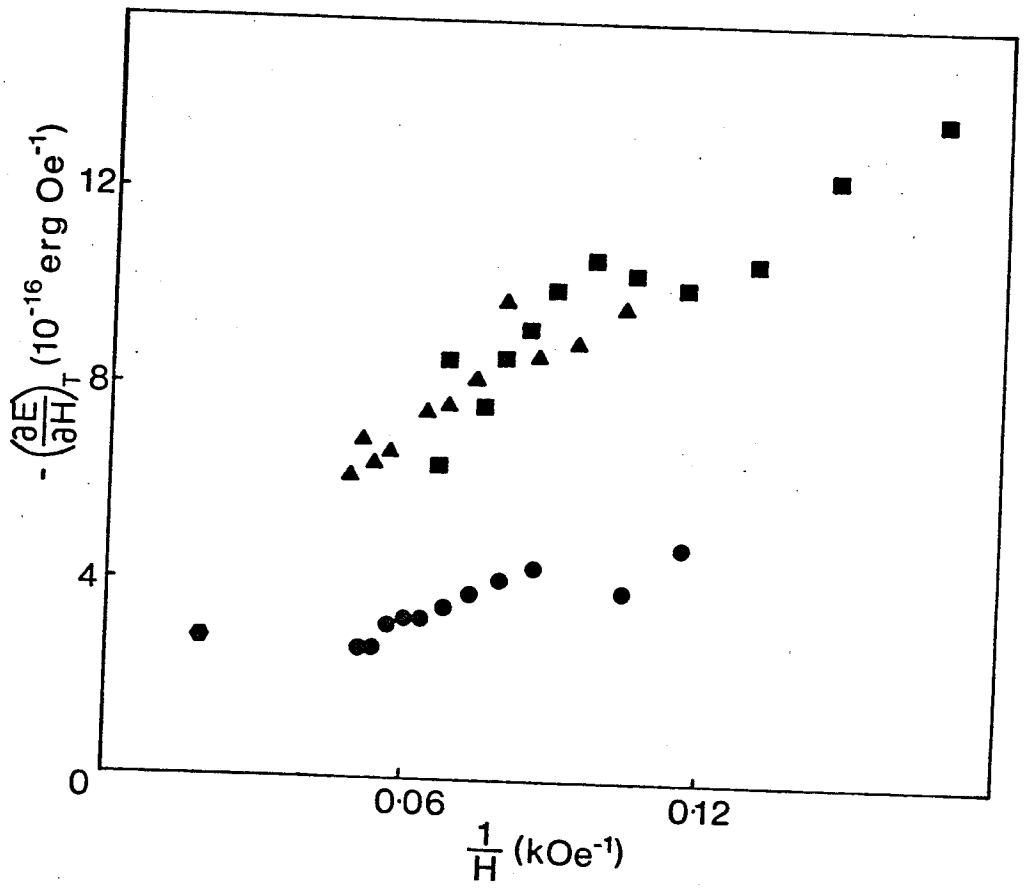

Figure 7.8.1-2 - Experimental activation energy/field parameter plotted against the inverse of the effective field at 77K for specimens B(squares), C(triangles) and M(circles). The hexagon denotes the theoretical prediction.

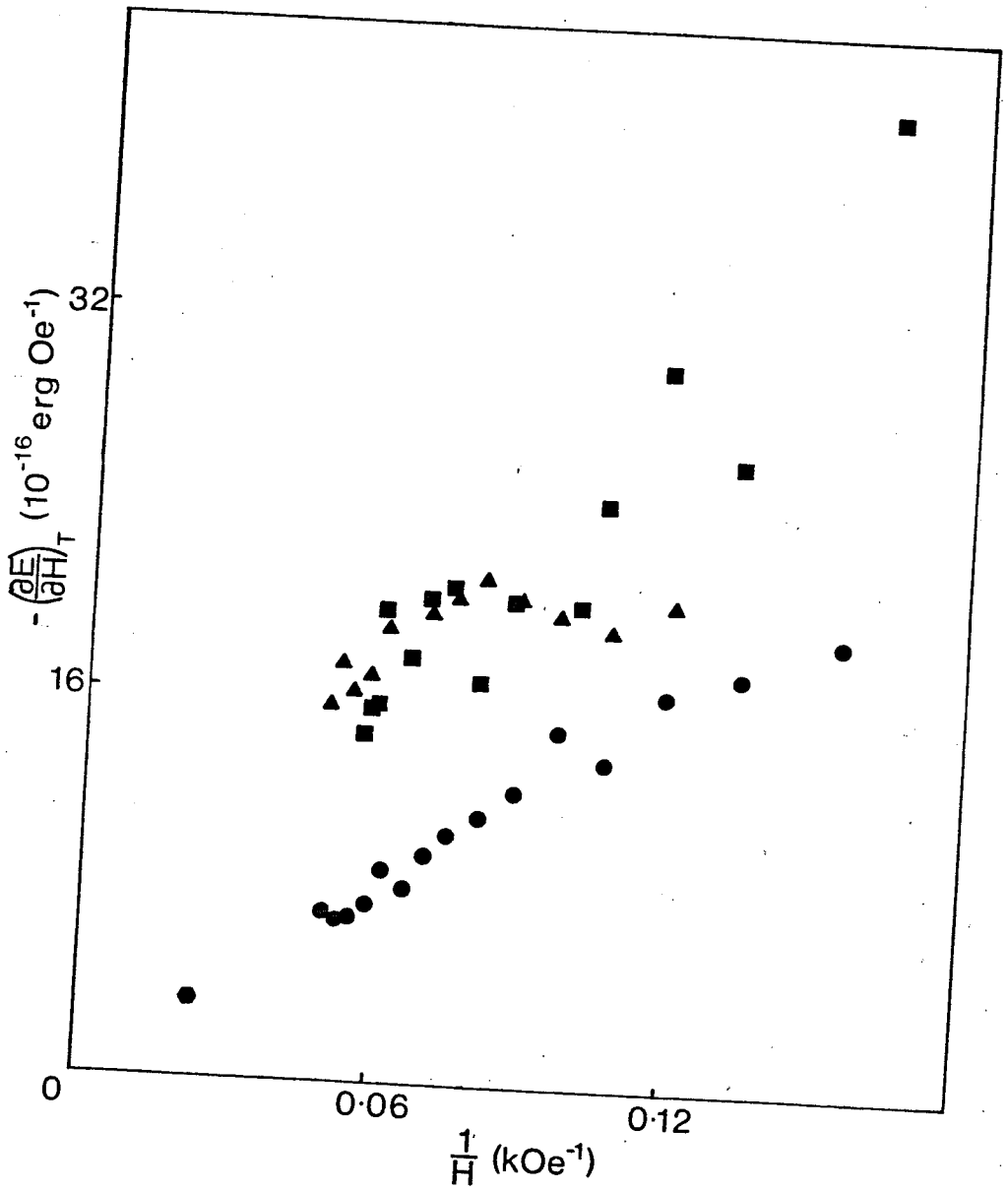

Figure 7.8.1-3 - Experimental activation energy/field parameter plotted against the inverse of the effective field at 200K for specimens B(squares), C(triangles) and M(circles). The hexagon denotes the theoretical prediction.

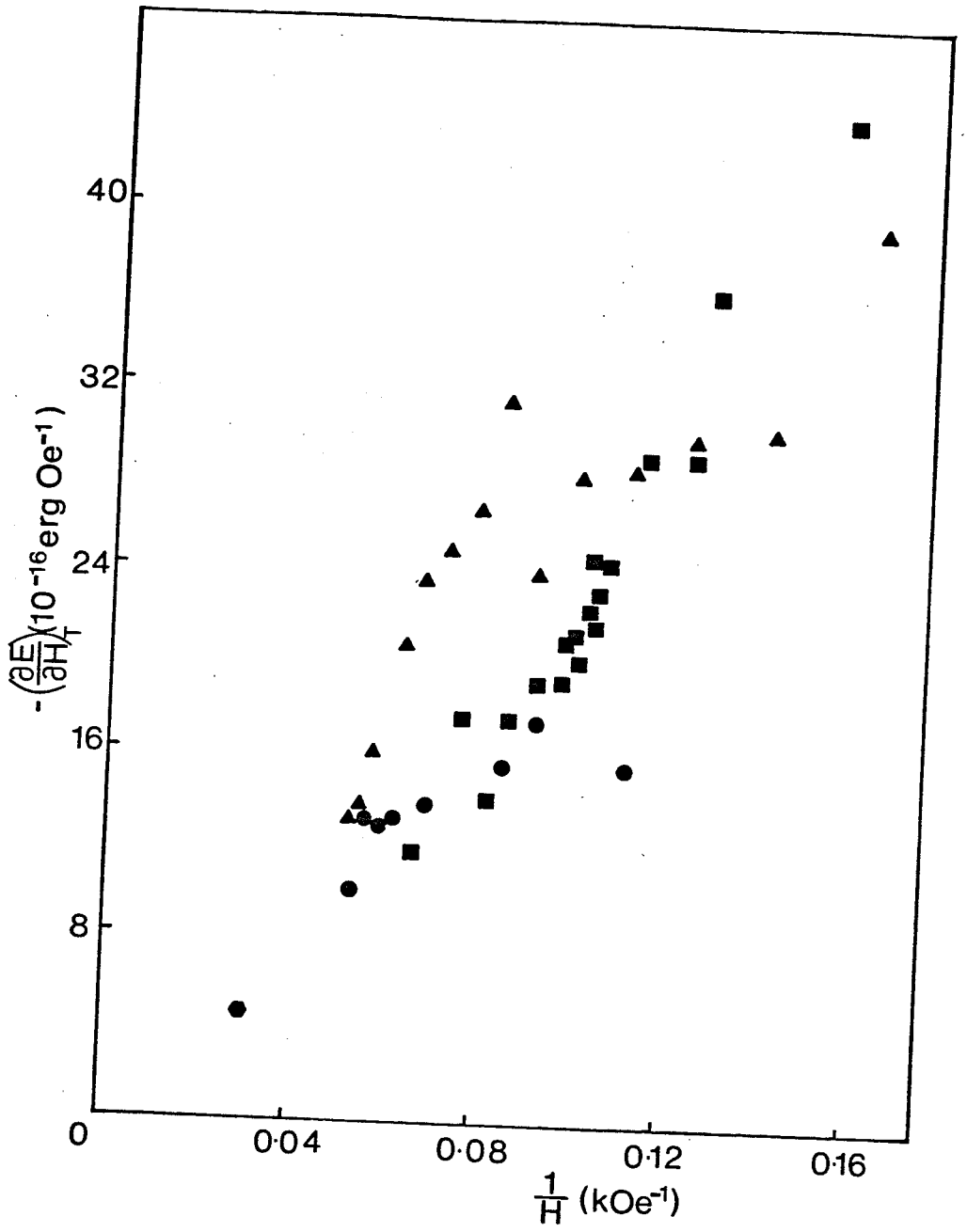

Figure 7.8.1-4 - Experimental activation energy/field parameter plotted against the inverse of the effective field at 295K for specimens B(squares), C(triangles) and M(circles). The hexagon denotes the theoretical prediction.

Table 7.8.1-1

Variation with Temperature of the

Activation Energy/Field Parameter for a 75Å Inhomogeneity

T (K)	$-(\frac{\partial E}{\partial H_T})$ (10^{-16} erg/Oe)
4.2	3.376
77	2.869
200	3.389
300	4.257

7.8.2 Specimen History and After-Effect

Figure 7.8.2-1 is a sketch of the typical hysteresis loop measured in the electromagnet for a specimen that had previously been placed in the superconducting magnet. The obvious asymmetry of the loop is purely a result of the small fields available in the electromagnet. The initial 'saturation' magnetization would therefore be different at the points A and B. After-effect measurements were carried out in the usual manner, starting at point A and then repeated with B as the new starting point. The two sets of data were processed and the calculated quantities compared.

However, while the differences between the two sets of values of S_{obs} and χ for specimen C at 295K are plainly seen in figure 7.8.2-2, as figure 7.8.2-3 shows, $(\frac{\partial E}{\partial H})_T$ itself was independent of the starting point and depended only on the effective observation field. This field is, in fact, the coercive field of that portion of the specimen that is undergoing reversal of its magnetization through thermal activation. $(\frac{\partial E}{\partial H})_T$ is therefore seen to have a constant value at the coercive field at that temperature. The implications of this result will be discussed in section 7.9.

7.8.3 Measurements at 4.2K

No measureable after-effect was seen at liquid helium temperatures.

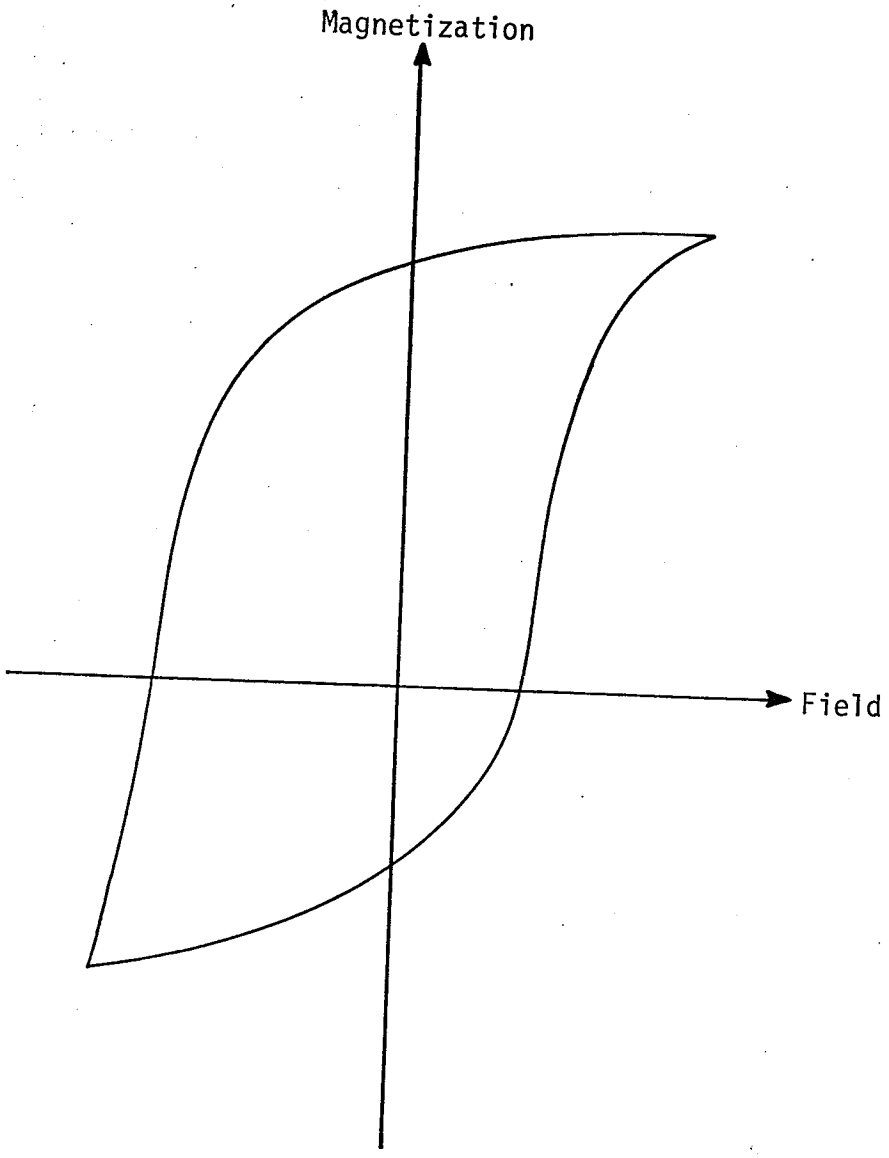

Figure 7.8.2-1 - The sketch of an 'unbalanced' hysteresis loop.

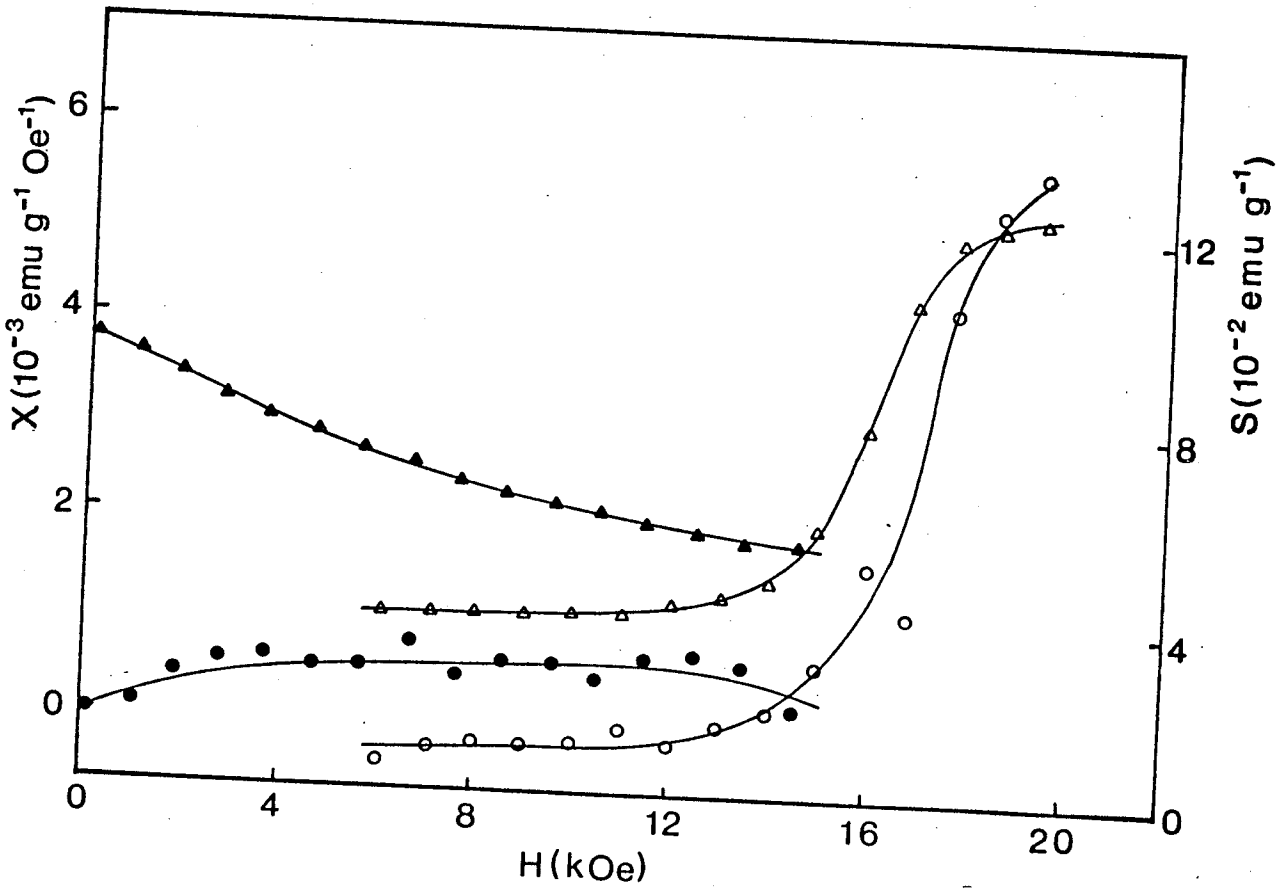

Figure 7.8.2-2 - Variation of viscosity coefficient (circles) and susceptibility (triangles) for specimen C at room temperature in forward (filled symbols) and reverse (hollow symbols) effective fields.

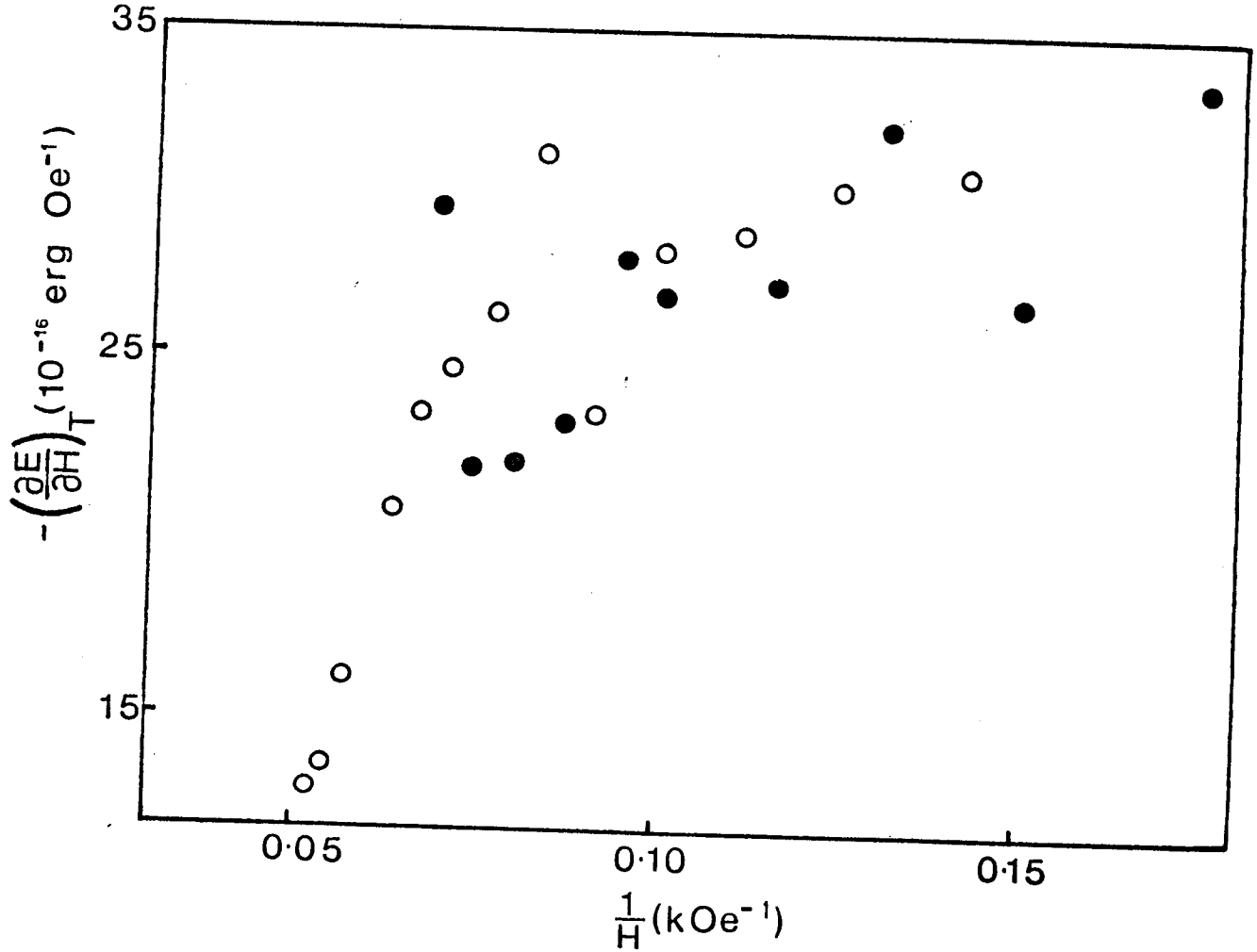

Figure 7.8.2-3 - Experimental activation energy/field parameters plotted against the inverse of the effective forward (filled circles) and reverse (hollow circles) fields for specimen C at 295K.

This is, in fact, as expected as the following calculation shows.

Because of electronic noise, the lowest usable range of the chart recorder was the 5mV full scale (100 units) range. To make a measurement, an after-effect of at least 1 unit in 16 seconds was necessary.

The smallest observable measurement is therefore 5×10^{-2}mV in 16 seconds which corresponds to a value of S of 1.25×10^{-5}V/$\log_2 t$

To convert this to units of emu/g/ℓnt, it is necessary to multiply this value by $\sim$500 for all specimens.

Thus, the smallest measureable value of the viscosity coefficient is 6.25×10^{-3}emu/g.

If the $SmCo_5$ magnet material contains planar Sm_2Co_{17} of thickness 100Å, the expected value of $(\frac{\partial E}{\partial H})_T$ at 4.2K is -3.411×10^{-16}erg/Oe (Table 7.8.1-1).

We had

$$(\frac{\partial E}{\partial H})_T = -kT\frac{\chi}{S} \qquad (7.3\text{-}2)$$

Dispensing with the corrections, because in the measuring field range $\chi \sim 5\times10^{-4}$emu/g/Oe and χD is consequently negligible, the expected value of S at 4.2K in this range of field is 8.5×10^{-4}emu/g, which is less than a seventh of the smallest measurable value. Indeed, this theoretical value is the value at the coercive field and is therefore much smaller than the viscosity coefficient that can be expected at fields in the measuring range.

7.9 Variation of $(\frac{\partial E}{\partial H})_T$ with Field

As seen in sections 7.7 and 7.8.1, it was not possible to measure magnetic after-effect at the calculated coercive fields. However, the fact that viscosity effects were observed at lower fields suggests that the material has within it regions having a range of coercivities smaller than the calculated one.

The calculations of sections 4.9 and 4.15 show that coercivity can decrease as inhomogeneity thickness decreases, or when grain size increases and multiple walls are present. However, with the exception of inhomogeneity thicknesses which approached the critical thickness, all such cases of reduced coercivity gave values of $(\frac{\partial E}{\partial H})_T$ which, as seen in figure 7.9-1, were smaller in magnitude than the value at the previously calculated coercive field. This was inconsistent with the experimental data and would seem to rule out grain and inhomogeneity dimension as the major cause of the observed reduced coercivities.

A factor that has an even greater bearing on the coercive field is the anisotropy constant. When the difference between the anisotropy constants of the $SmCo_5$ matrix, K_1 and the Sm_2Co_{17} inhomogeneity, K_2 was reduced, the decline in coercivity was accompanied by a rise in $(\frac{\partial E}{\partial H})_T$ as shown in figure 7.9-2 for a 100Å inhomogeneity at 77K. This is, in fact, the trend followed by the experimental data of section 7.7.

Using the theoretical curves in figure 7.9-2, the corresponding values of $(\frac{\partial E}{\partial H})_T$ for a given coercivity can be determined. For example,

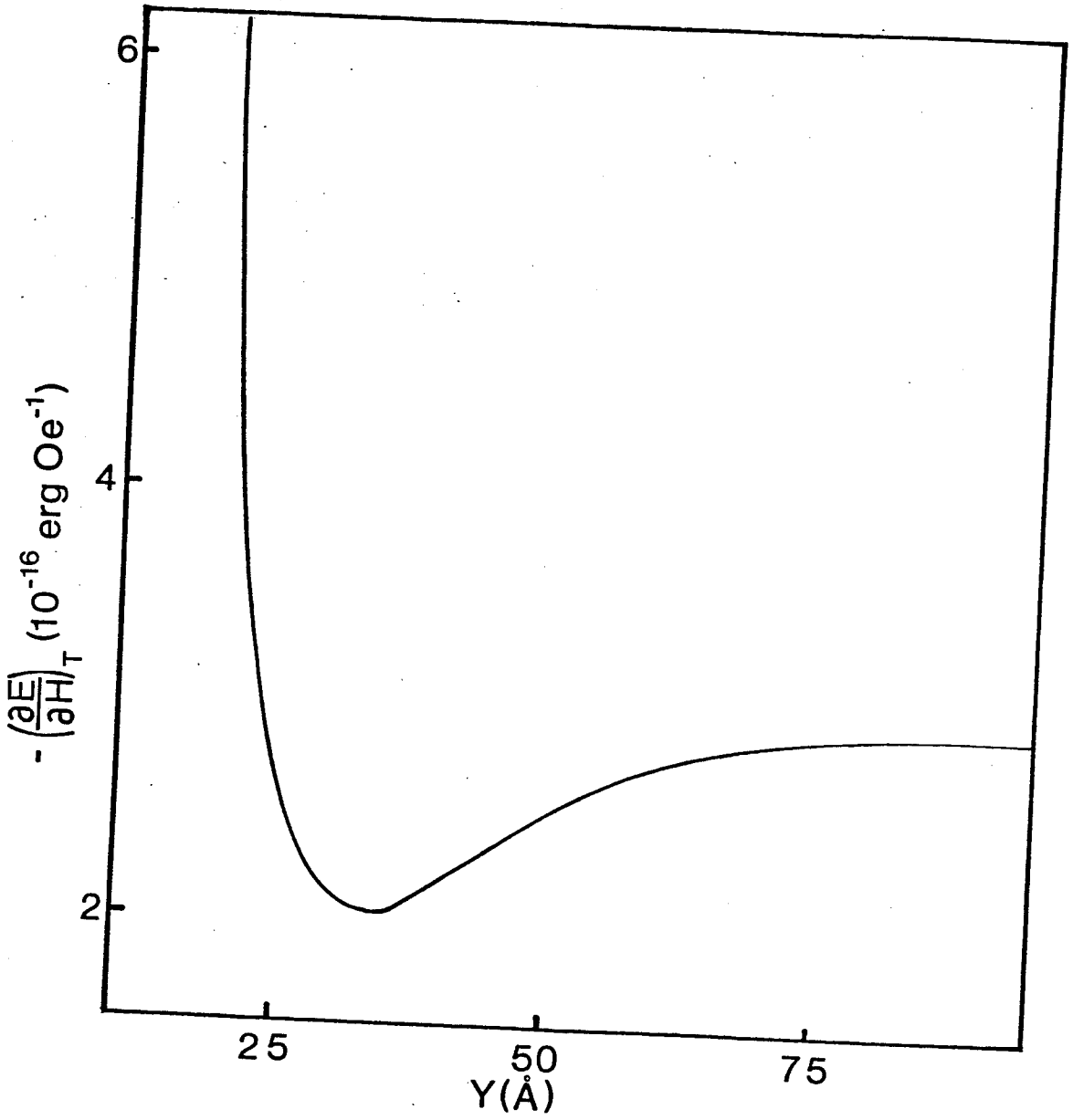

Figure 7.9-1 - Dependence of the activation energy/field parameter on inhomogeneity thickness at 77K.

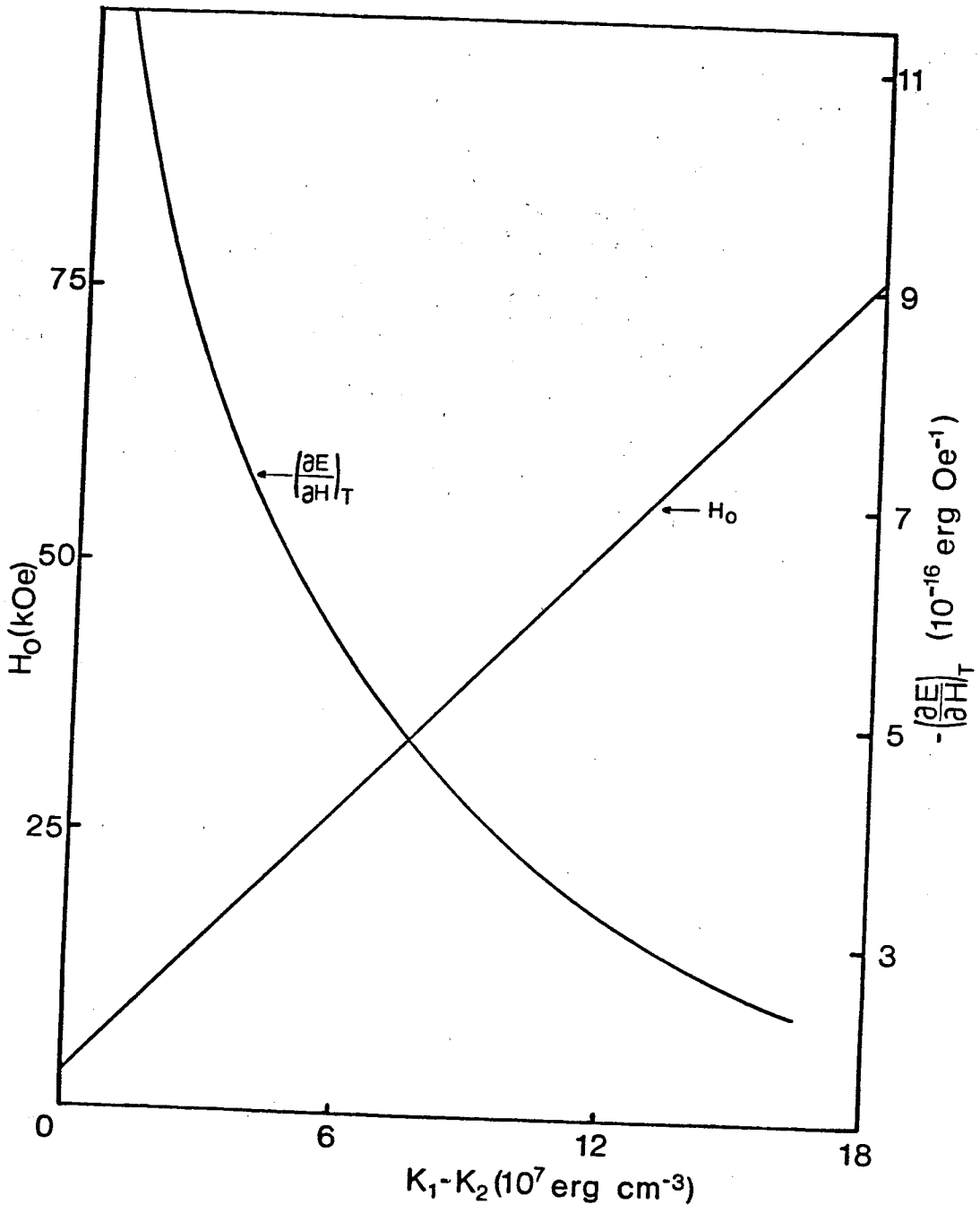

Figure 7.9-2 - Dependence of the coercivity and the activation energy/field parameter on the difference between the anisotropy constants for a 100A inhomogeneity at 77K.

a K_1-K_2 value of $2 \times 10^7 erg/cm^3$ is seen to cause a coercivity of 12kOe. This, in turn, corresponds to a $(\frac{\partial E}{\partial H})_T$ of $9.1 \times 10^{-16} erg/Oe^1$, which is consistent with the measured value at that temperature. Overall the correlation between coercivity and $(\frac{\partial E}{\partial H})_T$ when K_1-K_2 is varied is in fairly good agreement with the experimental findings.

Varying anisotropy constants is not as arbitrary a procedure as it may seem. Section 2.3 describes how, during the sintering process, factors such as the addition of samarium-rich alloys and oxidation can give rise to the presence of non-stoichiometric Sm-Co compounds which can alter the crystalline anisotropy as shown by Déportes, Girord, Schweizer and Tasset (1976) for YCo_5. The different coercivities could conceivably be the result of deviations from stoichiometry within the material.

Another reason that may be adduced for varying K is that whereas the calculations assume a model of a $SmCo_5$ matrix which contains a slab of Sm_2Co_{17}, in practice there is bound to be a region between the two distinct phases in which some mixing takes place, resulting once again in a smaller effective value of K_1-K_2.

While reducing the difference between K_1 and K_2 produces the desired trend in $(\frac{\partial E}{\partial H})_T$, it is to be expected that other factors, such as variation in inhomogeneity thickness, will also influence the observed value.

7.10 Discussion

The change in magnetization caused by thermal activation has been shown to vary linearly with the logarithm of time. This supports the concept of a range of activation energies within the material as described in section 7.2. It must be noted here that at large times it is difficult to distinguish between this logarithmic variation and the inverse exponential dependence of eq.(7.2-2) which is valid for a single activation energy. The difference between the two relationships is most evident at small times and this is where the role of the microswitch is crucial.

For satisfactory comparison of theory with experiment, experimental results must be reproducible. Yamada, Yamada and Ono (1979) have observed that in samarium-cobalt magnets the viscosity coefficient depended on specimen history. This is confirmed in the present study. However, it was also observed here that the quantity $(\frac{\partial E}{\partial H})_T$ was independent of history and depended only on the effective field at the time of measurement. It can therefore be compared with the theoretically obtained values of table 7.8.1-1.

This lack of dependence of $(\frac{\partial E}{\partial H})_T$ on the demagnetizing path chosen has further significance. Combining eqs.(3.5-6) and (3.7-2), the relationship between the thermally activated coercive field, H_c' and the absolute zero coercivity, H_0' of the region undergoing reversal is derived as:

$$H_c' = H_0' - \frac{25kT}{\left(\frac{\partial E}{\partial H}\right)_T}$$

Since a one-to-one correspondence exists between H_c' and $\left(\frac{\partial E}{\partial H}\right)_T$, the reproducibility of $\left(\frac{\partial E}{\partial H}\right)_T$ tells us that even though the distribution of the particles undergoing reversal at a particular field may be changing, the intrinsic coercivities of the individual particles themselves remain constant. This is true even in the case of multiple double walls, for as section 4.15 illustrates, b depends on H_0 and not on wall multiplicity, while γ will hardly change. $\left(\frac{\partial E}{\partial H}\right)_T$ does not therefore depend on the number of walls present.

As in figures 7.8.1-2 to 7.8.2-4 illustrate, extrapolation to higher fields of the experimental $\left(\frac{\partial E}{\partial H}\right)_T$ values provide good agreement with theoretical calculations. Even the unobservability of after-effect at the liquid helium temperature has been predicted. Since $\left(\frac{\partial E}{\partial H}\right)_T$ is a quantity that stems directly from the pinning model and is affected entirely by the concepts therein, the results in this chapter would seem to verify the model.

Note must also be taken of the range of coercivities observed at each temperature. As the preceding section illustrates, a plausible explanation for this phenomenon may be the presence of non-stoichiometric phases of the Sm-Co alloys under consideration. Grain size and inhomogenity thickness would appear to be ruled out as possible causes.

In summary then, the after-effect measurements detailed in this chapter serve first of all to confirm the validity of the interaction

model of chapter 3. Beyond that though, they complement previously calculated and measured results to yield information about the nature of the sintered $SmCo_5$ magnet alloy and the underlying causes of its coercivity.

CHAPTER 8

BARKHAUSEN EFFECT

8.1 Introduction

Barkhausen (1919) observed that magnetization changes in ferromagnets were discontinuous. These discontinuities reflected the fact that changes in magnetization were caused by irreversible domain wall movements from pinning site to pinning site, rather than by a gradual change of magnetization within domains, lending further credence to the theory that there was free movement of domain walls within the bulk of the material. If the incremental changes in magnetization are measured therefore, the volume traversed by individual domain walls between pinning sites can be estimated with some confidence.

8.2 Observation of the Effect

The electromagnet and the sensing coil system detailed in section 6.3 were used with a cathode ray oscilloscope connected across the terminals of the coil so as to give a direct measure of the rate of change of flux through the coil, instead of the integrated signal obtained earlier. A variable resistance was placed in parallel with the sensing coils and adjusted so as to damp out any oscillations. It was found that a resistance of 7000Ω was suitable for this purpose.

When the magnetic moment of the volume within the sensing coils changed, the magnetic flux through the coils was altered and an induced e.m.f. was established in the coil circuit as has been discussed more fully in section 6.2. This e.m.f. disappeared when the flux became

stable and the net result of the process was an approximately trianguler spike in the trace of the oscilloscope (figure 8.2-1). The area below the spike was proportional to the total flux change and therefore to the change in magnetization.

8.3 Calibration

The system was calibrated by inserting a specimen of known moment into the coil. The height and width of the resulting spike were read off the screen of the oscilloscope and the area was calculated in units of (e.m.f.).(time). The resulting calibration factor was 1.55×10^5 e.m.u./volt.second.

8.4 Experimental Techniques

Measurements on all three samples (B,C and M) were carried out in the following manner.

A sample was placed in a large forward field and then removed. The magnetic field was reversed and the specimen was reinserted. After a brief flurry of spikes on the screen, caused by the initial magnetization change, the frequency of their appearance diminished and it was possible to distinguish individual spikes. From the dimensions of a number of spikes it was possible to obtain the range of changes in magnetization.

Motion of a 180° domain wall results in reversal of magnetization

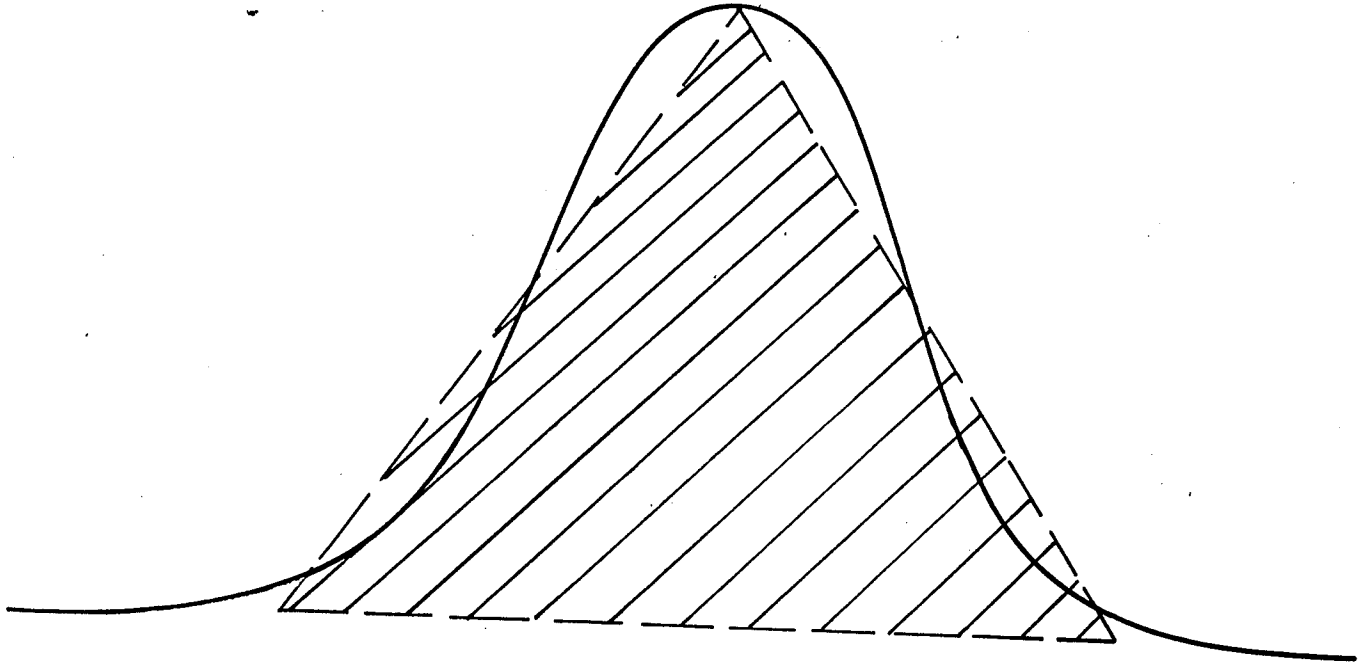

Figure 8.2-1 - Typical output trace seen on screen of the CRO during a measurement of Barkhausen effect. The shaded area is approximated to be the area under the spike.

in the area through which the wall has passed. The observed change in magnetization therefore corresponded to twice the magnetic moment of this area and this had to be taken into account when calculating the magnetic moment.

Since the magnetization of $SmCo_5$ was known, the volume of the domain corresponding to the observed spike could be evaluated.

8.5 Results

Observations were made throughout the range of fields available with the electromagnet. The necessary corrections were made for image effect.

No substructure was observed in the spikes, implying that trapping was a single event and that there was no partial trapping within domains in the reverse fields that were used.

A preponderance of larger spikes were observed at lower fields. While this was an essentially qualitative observation, it was noticeable enough to strongly suggest that larger domains had, in general, lower coercivities. This is supportive of the theoretical findings of section 4.15.

Convincing evidence that domain wall trapping takes place only at grain boundaries is presented in table 8.5-1. The measured maximum and minimum domain volumes and corresponding dimensions are compared with the observations of grain size by optical microscopy of section 5.5. The upper limits are in agreement within a few microns, while the lower limits

Table 8.5-1

Comparison of Grain and Domain Sizes

Specimen	Max. Domain Volume (10^{-7} cm^3)	Min. Domain Volume (10^{-7} cm^3)	Max. Domain Dimension (μ)	Min. Domain Dimension (μ)	Max. Grain Dimension (μ)	Min. Grain Dimension (μ)
B	4.2	0.4	75	30	72	33
C	1.7	0.4	55	30	50	28
M	1.0	0.4	47	30	48	24

also agree reasonably well if the experimental uncertainty in the Barkhausen observation, which is $\sim$ 25% for the dimension at this limit, is taken into account. This result suggests that grains and domains are synonymous in sintered $SmCo_5$ and that there is free movement of domain walls within grains, with the boundaries acting as pinning sites, as Livingston (1975) has shown, using Kerr effect observations.

The table also indicates that specimen B has a larger overall domain size than either C or M. When this is correlated with the measurements of coercivity of section 6.5.3, the implication once again is that the larger the size of the grain, the lower the coercive field.

In summary, the measurements of Barkhausen effect detailed in this chapter yield valuable information about the mechanism of domain wall motion and confirm some of the underlying assumptions of the theory developed in chapters 3 and 4.

CHAPTER 9

CONCLUSIONS

9.1 Pinning, Nucleation and the Micromagnetic Model

The causes of the large coercivities exhibited by $SmCo_5$ alloys have undergone extensive investigation. The two mechanisms that are generally proposed are the pinning of domain walls (Zijlstra 1970) and the difficulty of nucleating reverse domains (Becker 1970). In this study it is suggested that when two winding 180° walls meet in the presence of an inhomogeneity of lower wall energy, they are bound rather than annihilated, producing a 360° domain wall. Nucleation is therefore merely the unpinning of the 180° wall pair. Using such a hypothesis, the micromagnetic model of chapter 4 was developed.

The model is based upon the concept of pinning of domain walls by regions of lower wall energy within the matrix. It has been assumed that the inhomogeneity is discontinuous and manifests itself in planar form. Livingston (1973) has shown, using Kerr microscopy, that domain wall pinning in sintered $SmCo_5$ takes place at grain boundaries. This has been confirmed by observations of the Barkhausen effect described in chapter 8, which demonstrated that the size of individual domain reversals corresponded to the actual grain volume to within a few percent. Discontinuous pinning is further supported by the observations of chapter 6 which show that the domain wall is able to move freely over 82% of the material before any sizeable trapping occurs. This feature of pinning at grain boundaries may be contrasted with the intra-grain pinning

observed in Co-Cu-Fe-Sm magnets (Livingston 1975). den Broeder and Zijlstra (1976) have examined the behaviour of coercivity with heat treatment and microstructure in sintered $SmCo_5$. Using long annealing times they induced large scale precipitation of Sm_2Co_{17} and Sm_2Co_7 within grains. These phases acted as nucleation centres, producing reduced coercivities. This further corroborates the findings that the large coercivities which have been observed in this study are caused by pinning at grain boundaries.

The composition of the pinning site has been open to some speculation. Searle and Garrett (1974) have suggested that pure cobalt is a possible inhomogeneity, while Westendorp (1970) has considered the possibility of absorbed hydrogen as the pin. In the present study it has been suggested that the cobalt-rich Sm_2Co_{17} phase acts as the pinning material. Unfortunately the evidence for this is not conclusive as explained further in chapter 5. It seems clear however, that some material other than $SmCo_5$ characterizes grain boundaries. Fidler, Kirchmayr and Wernisch (1979) have shown that Sm_2Co_{17} precipitates form a coherent precipitate in the $SmCo_5$ matrix with c-axes of the two phases parallel and the basal axes rotated in 30° with respect to each other. Khan and Qureshi (1973) have claimed that Sm_2Co_{17} is always present, regardless of the type of heat treatment.

The major failing of the present study was the inability to positively identify the intra-grain inhomogeneity, as detailed in chapter 5. An alternate method of preparing specimens to be examined in the

electron microscope such as ion beam thinning, or the use of a different electropolishing solution may provide information on the nature of the grain boundary.

Another possible cause of pinning was the presence of $SmCo_5$ crystallites which had not been properly aligned during sintering. Since the misorientation is quite small, the resulting coercivity may be expected to be low, but this intra-grain pinning may explain the small coercivities of $\sim$100 Oe that are initially observed in the specimen (section 6.5.2).

Most of these assumptions have been incorporated into the calculations of chapter 4. The agreement between the calculated coercivity for a variety of inhomogeneity thicknesses and experimental determinations of coercivity is very good. Particularly striking is the degree of correlation with the curve of normalised coercivity versus temperature which Benz and Martin (1972) have propounded as a universal curve. Considering that the only parameter that was varied was the inhomogeneity thickness and that the sensitivity to even this parameter was relatively insignificant, it must be concluded that the model and the assumptions incorporated within it have been adequately validated.

Using the model, a critical inhomogeneity thickness has been determined, below which no pinning can take place. This may explain why bulk samples of $SmCo_5$ exhibit negligible coercivities, while liquid phase sintered magnets have large coercivities. The role of the sintering process may be to enlarge the intergrain inhomogeneity region.

9.2 Thermal Activation and Magnetic After-Effect

Using a simple parabolic force model, the interaction between a domain wall and a pinning site has been described in chapter 3. This model predicts that the activation energy, which is the energy that the trapped wall requires for escape, is related to the magnetic field by a two-thirds power relationship (eq.(3.3-5)).

This is, in fact the relationship obeyed by the activation energy calculated using the micromagnetic model of chapter 4. One is therefore justified in linking the two models and parameters such as the interaction distance can be calculated.

The concepts of the interaction model are quite basic, with the additional refinement of the 'blister' which enables the continuously pinned wall to break away from the pin by thermal activation at a lower field than might otherwise be expected. However, the effect of thermal activation on coercivity is, as seen in figure 4.13-1, relatively small. Some further type of measurement is therefore required to test its validity and this is where magnetic after-effect plays a crucial role.

The viscosity parameter, S has been measured in this study. As Yamada et al (1979) have noted, S depends on the sample history. However, the parameter $(\frac{\partial E}{\partial H})_T$ is, as shown in figure 7.8.2-3, independent of history and unique to the effective field on the specimen. The values of $(\frac{\partial E}{\partial H})_T$ from measurement have been compared with the calculated values in

figures 7.8.1-2 to 7.8.1-4. Despite the previously noted inability to measure after-effect at the predicted coercive field, it is clear that the experimental points extrapolate toward the theoretical value.

Perhaps even better agreement may have been obtained if an improved frequency factor was known. The value of exp(25) Hz which was used, has been calculated for a two dimensional case, whereas the present study deals with a three dimensional process.

9.3 Variation of Coercive Field and Composition of the Material

While declining coercivities may be explained by decreased inhomogeneity thickness or the presence of more than one pair of walls within the grain, the after effect measurements of chapter 7 show that at measuring fields lower than the mean coercive field, the parameter $(\frac{\partial E}{\partial H})_T$ rises. Decreased thickness however, leads to a lower predicted $(\frac{\partial E}{\partial H})_T$ and thus cannot account for this observation.

It is to be expected that rather than having a precise boundary between the respective $SmCo_5$ and Sm_2Co_{17} regions, there is a layer in which they diffuse into each other, causing the effective difference between their anisotropy constants to decrease.

Buschow and den Broeder (1973) have stated that a non-stoichiometric phase of the form $SmCo_{5+x}$ is the likely form of primary phase in the sintered alloy. A study of the process of manufacture and the phase diagram, described in chapter 2, show that the samarium-rich alloy

$SmCo_{5-x}$ could also be present. Such non-stoichiometric phases, as Déportes et al (1976) have shown, produce disordering within the lattice, which in turn, cause a decrease in the crystalline anisotropy.

Calculations discussed in section 7.9 show that as the anisotropy energies of the matrix and the inhomogeneity grow closer together, coercivity falls, while $(\frac{\partial E}{\partial H})_T$ rises. This suggests that the sintered material is indeed non-stoichiometric.

9.4 Summary

Recounting the features of this study, the following conclusions may be drawn.

(a) The large coercivities of sintered $SmCo_5$ permanent magnets are the result of pinning of domain walls at grain boundaries. The pinning material may be the cobalt-rich Sm_2Co_{17} phase. Liquid phase sintering may promote the growth of the inter-grain phase. Variations in coercivity may be a result of non-stoichiometric material within the magnet. A minimum thickness of the pinning site is required before the walls can be trapped.

(b) The so-called 'nucleation' of reverse domains is, in fact, the splitting of a 360° domain wall into two 180° walls upon application of the coercive field.

(c) A single parabolic force model can describe the interaction between the domain wall and the inhomogeneity. The wall, which has been

pinned, bows out and finally breaks away as a result of thermal activation.

There are a few areas in which further improvement can be made.

(a) The results of the electron microscope investigation into the nature of the grain boundary inhomogeneity were inconclusive.

(b) After-effect measurements could not be made at the predicted coercive field of the material, forestalling direct comparison of experiment with theory.

(c) A value of the frequency factor for a three dimensional system was not available.

Despite these drawbacks, the investigation may, on the whole, be regarded as having been successful with satisfactory correlation between theoretical prediction and experimental observation. The trends which have been predicted are not restricted to the case of the Sm_2Co_{17} inhomogeneity, which has been considered here in some detail, but remain valid for any pinning site which has a lower wall energy than the $SmCo_5$ matrix.

APPENDIX

Calculation of the Spin Angle θ_1 from Eq.(4.4-12)

Outline of the Procedure and the Transformations

The expression for inhomogeneity thickness has been derived in the form of the elliptic integral:

$$Y = 2a_2^{\frac{1}{2}} \int_{\theta_1}^{\pi} (\sin^2\theta - 2h_2\cos\theta + c)^{-\frac{1}{2}} \, d\theta \qquad (4.4\text{-}12)$$

The lower limit θ_1 is required when Y, a_2, h_2 and c are known. To do this it is first necessary to use a prescription which has been developed by Forlani and Minnaja (1969) which transforms the elliptic integral of eq.(4.4-12) into an incomplete elliptic integral of the first kind. The procedure is detailed below.

Let

$$r = (1 + c + h^2)^{\frac{1}{2}} ,$$

$$k = \frac{[(r+h+1)(r-h+1)]^{\frac{1}{2}} - [(r+h-1)(r-h-1)]^{\frac{1}{2}}}{[(r+h+1)(r-h+1)]^{\frac{1}{2}} + [(r+h-1)(r-h-1)]^{\frac{1}{2}}} ,$$

$$C = \frac{[(r+h-1)(r-h-1)]^{\frac{1}{2}}}{1+k}$$

and

$$t = \frac{[(r+h-1)(r-h+1)]^{\frac{1}{2}} - [(r+h+1)(r-h-1)]^{\frac{1}{2}}}{[(r+h-1)(r-h+1)]^{\frac{1}{2}} + [(r+h+1)(r-h-1)]^{\frac{1}{2}}}$$

(The suffix '$_2$' in h_2 has been omitted)

The complete elliptic integral of the first kind,

$$F(\frac{\pi}{2}\ ,\ k) = \int_0^{\frac{\pi}{2}} \frac{d\phi}{\sqrt{1-k^2\sin^2\phi}}$$

can thus be evaluated.

An incomplete elliptic integral of the first kind, $F(\phi,k)$ is then generated as follows:

$$F(\phi,k) = \frac{1}{2}\, a_2^{-\frac{1}{2}}\, CY - F(\frac{\pi}{2}\ ,k) \quad ,$$

where ϕ is related to θ_1 by the expression:

$$\theta_1 = \cos^{-1}(\frac{t + \sin\phi}{1 + t\sin\phi})$$

Since k is known, ϕ can be obtained and θ_1 is thus evaluated.

The value of θ_1 which is obtained for the appropriate inhomogeneity thickness and field and the chosen constant C, is then used in eq.(4.4-14) to obtain the corresponding value of $\frac{dE}{d\theta_1}$. The above procedure is repeated for a range of values of C and a series of θ_1 and corresponding $\frac{dE}{d\theta_1}$ values are thus computed.

Series Forms of the Elliptic Integral and Inverse

Since it was more convenient to perform the calculations on a computer, it was necessary to employ the following algorithms for the generation of the complete elliptic integral, $F(\frac{\pi}{2}\ ,\ k)$ and the inverse,

ϕ, of the incomplete elliptic integral $F(\phi,k)$. These were obtained from the work of Gradshteyn and Ryzhik (1965). The figures in paranthesis against the equations are the labels that they have assigned.

The complete elliptic integral of the first kind,

$$F(\tfrac{\pi}{2},k) = \tfrac{\pi}{2}\{1 + \sum_{n=1}^{N}\left[\frac{(2n-1)!!}{2^n\, n!}\right]k^{2n}\} \quad . \qquad (8.112\ \#1)$$

Choosing N = 45 gave results that compared extremely well with tabulated values.

The inverse of the incomplete elliptic integral of the first kind,

$$\phi = \sin^{-1}\{\frac{2\pi}{kF(\frac{\pi}{2},k)} \sum_{n=1}^{M}\frac{q^{n-\frac{1}{2}}}{1-q^{2n-1}}\sin\left[\pi(2n-1)\frac{F(\phi,k)}{F(\frac{\pi}{2},k)}\right]\} \quad , \quad (8.146\ \#1)$$

where

$$k' = (1-k^2)^{\frac{1}{2}}$$

and

$$q = \exp\{-\pi\left[\frac{F(\frac{\pi}{2},k')}{F(\frac{\pi}{2},k)}\right]\}$$

It was found that setting M = 21 gave satisfactory results.

REFERENCES

Barkhausen, H., 1919, Physik Z., 20, 401

Bean, C.P., and Livingston, J.D., 1959, J. Appl. Phys., 30, 120S

Becker, J.J., 1970, IEEE Trans. Magn., MAG-7, 644

Benz, M.G., and Martin, D.L., 1970, Appl. Phys. Lett., 17, 176

Benz, M.G., and Martin, D.L., 1972, J. Appl. Phys., 43, 4733

Bozorth, R.M., 1951, Ferromagnetism (Princeton : D. Van Nostrand)

Buschow, K.H.J., Luiten, W., and Westendorp, F.F., 1969, J. Appl. Phys., 40, 1309

Buschow, K.H.J., and den Broeder, F.J.A., 1973, J. Less-Common Met., 33, 191

Cech, R.E., 1970, J. Appl. Phys., 41, 5247

Cottrell, A.H., and Bilby, B.A., 1949, Proc. Phys. Soc. London A, 62, 49

Craik, D.L., and Hill, E.W., 1974, Phys. Lett., 48A, 157

Crangle, J., and Goodman, G.M., 1971, Proc. Roy. Soc. A, 321, 477

Das, D.K., 1969, IEEE Trans. Magn., MAG-5, 214

den Broeder, F.J.A., and Buschow, K.H.J., 1972, J. Less-Common Met., 29, 65

den Broeder, F.J.A., and Zijlstra, H., 1976, J. Appl. Phys., 47, 2688

Déportes, J., Girord, D., Schweizer, J., and Tasset, F., 1976, IEEE Trans. Magn., MAG-12, 1000

Deryagin, A.V., Kudrevatykh, N.V., and Bashkov, Yu.F., 1974, Proc. Intern. Conf. on Magnetism, Moscow, 1973 (in Russian), 1, 2, 222

Egami, T., 1973, Phys. Stat. Solidi, 57, 211

Fermi, E., 1950, Nuclear Physics (Chicago : Univ. of Chicago Press)

Fidler, J., Kirchmayr, H., and Wernisch, J., 1979, Private Communication

Forlani, F., and Minnaja, N., 1969, J. Appl. Phys., 40, 1092

Gaunt P., 1976, Philos. Mag., 34, 775

Glasstone, S., Laidler, K.J., and Eyring, H., 1941, The Theory of Rate Processes (New York : McGraw Hill)

Gradshteyn, I., and Ryzhik, I., 1965, Tables of Integrals, Series and Products (New York : Academic Press)

Granato, A.V., Lücke, K., Schliff, J., and Teutonico, L.J., 1964, J. Appl. Phys., 35, 2732

Hadjipanayis, G.C., 1979, Thesis, Univ. of Manitoba (Unpublished)

International Tables for X-ray Crystallography, 1969, Volume I, Henry, N.F., and Lonsdale, K., (ed.) (Birmingham : Kynoch)

Jorgenson, P.J., and Bartlett., R.W., 1973, USAF Materials Laboratory Report No. AFML-TR-73-60

Kersten, M., 1943, Grundlagen einer Theorie der Ferromagnetischen Hysterese und der Koerzitivkraft (Leipzig : Hirzel)

Khan, Y., and Qureshi, A.H., 1973, J. Less-Common Met., 32, 307

Livingston, J.D., 1973, Phys. Stat. Solidi (A), 18, 579

Livingston, J.D., 1975, J. Appl. Phys., 46, 5259

Martin, D.L., Benz, M.G., and Rockwood, A.C., 1972, AIP Conf. Proc., 10, 583

Martin, D.L., and Smeggil, J.G., 1973, IEEE Trans. Magn., MAG-10, 704

Morrish, A.H., 1965, The Physical Properties of Magnetism (New York : John Wiley)

Néel, L., 1946, Ann. Univ. Grenoble, 22, 299

Osborn, J.A., 1945, Phys. Rev., 67, 351

Ostertag, W., Strnat, K., and Hoffer, G.I., 1967, USAF Materials Laboratory Report No. AFML-TR-66-420

Rebouillat, J.-P., 1972, These, Univ. Scientifique et Medicale de Grenoble (Unpublished)

Riley, A., and Jones, G.A., 1973, IEEE Trans. Magn., MAG-9, 201

Searle, C.W., and Garrett, H.J., 1974, J.Appl. Phys., 45, 5037

Stoner, E.C., and Wohlfarth, E.P., 1948, Phil. Trans. Roy. Soc. A, 240, 599

Street, R., and Woolley, J.C., 1949, Proc. Phys. Soc. A, 62, 562

Taylor, K.N.R., 1971, Adv. Phys., 20, 551

Weiss, P., 1907, J. Phys., 6, 661

Westendorp, F.F., 1970, Sol. State Comm., 8, 139

Yamada, O., Yamada, M., and Ono, F., 1979, Proc. Fourth Intern. Workshop on Rare Earth - Cobalt Permanent Magnets, Hakone Prince Hotel, Japan, 241

Zijlstra, H., 1970, J. Appl. Phys., 41, 4881